FERMILAB-THESIS-2009-75

SEARCH FOR THE SUPERSYMMETRIC PARTNER OF THE TOP QUARK IN DILEPTON EVENTS PRODUCED IN PROTON-ANTIPROTON COLLISIONS AT $\sqrt{S}$ =1.96 TEV

A Dissertation

Submitted to the Faculty

of

Purdue University

by

Alexei A. Sedov

In Partial Fulfillment of the

Requirements for the Degree

of

Doctor of Philosophy

May 2009

Purdue University

West Lafayette, Indiana

To my mother Galina, my wife Inna and our baby due in July.

ACKNOWLEDGMENTS

First and foremost, I would like to thank my advisor, Professor Vigil E. Barnes, for guidance, wisdom and patience. I remember when I broke that plug sourcing wire, everybody was pointing fingers at me, telling that I broke a $3000 equipment, and you made me happy by letting me go to Russia to visit my family, while you were fixing that wire in Purdue!

I am deeply indebted to Dr. Oscar González for an extensive help in this analysis as well as plug sourcing. His work is present in most parts of the analysis starting with Monte Carlo simulation generation and ending with golden plots production.

I wish to thank Dr. Alvin Laasanen for useful analysis discussions. His extensive Fortran knowledge was invaluable during "corlim" 95% expected limit calculations.

I would like to thank the Multilepton group, in particular I am grateful to Drs. Elsa Lytken, a former Purdue postdoctoral research assistant now at CERN, and Beate Heinemann for their work on the fakes.

I would especially like to thank Dr. Konstantin Anikeev for getting me started in CDF and for all the useful conversations we had. Now I can tell, Konstantin, I'm not mad at you for that marathon you tricked me to run!

CDF Purdue group for fruitful discussions during Purdue meetings as well as nice trips to the APS meetings!

I thank all (former and current) SUSY and exotics conveners for helpful suggestions for the analysis.

Russians from MIT group for help in understanding SmartSockets and Hardware Event Builder, it made my plug sourcing software production much easier.

Drs. Willis Sakumoto, Steve and Dee Hahn for their support and understanding during plug sourcing times.

I dearly thank all of my friends from Russia, Purdue, and Chicago area, who made my life better and more productive!

This thesis would not have been complete without the contributions of many past and present CDF collaboration members. Thank you all!

TABLE OF CONTENTS

Page

LIST OF TABLES vii

LIST OF FIGURES viii

ABSTRACT x

1 INTRODUCTION 1

2 THE STANDARD MODEL 3
2.1 The theory 3
2.1.1 The Higgs scalar 5
2.2 Problems of the Standard Model 6

3 SUPERSYMMETRY 8

4 EXPERIMENTAL APPARATUS 10
4.1 Tevatron 10
4.1.1 Cockroft-Walton Chamber, Linac, and Booster 10
4.1.2 The Main Injector, Accumulator and Recycler 12
4.1.3 Tevatron 13
4.2 The CDF II detector 14
4.2.1 Tracking system 15
4.2.2 Calorimetry 17
4.2.3 Muon detection 19
4.2.4 Trigger system 21

5 STOP QUARK AT THE TEVATRON 23
5.1 Production 23
5.2 Decay 24

6 DESCRIPTION OF THE ANALYSIS 27
6.1 Search strategy 27
6.2 Data samples 29
6.3 SM Backgrounds from Monte Carlo 29

7 BASIC EVENT SELECTION 32
7.1 Electron 32
7.2 Muon 36
7.3 Jets 38
7.4 Missing transverse energy 39

Page

8 TRIGGERS 41

9 SYSTEMATIC UNCERTAINTIES 44

10 PRESELECTION AND CONTROL REGIONS 46
10.1 Control Region A (Z peak). 48
10.2 Control Regions with low $\not\!\!E_T$ and no jets. 49
10.3 Control Regions with high $\not\!\!E_T$ and no jets. 55
10.4 Control Regions with low $\not\!\!E_T$ and at least one jet. 55
10.5 Extra clean up cut for pre-signal region 66

11 ANALYSIS 69

12 RESULTS 77

13 SUMMARY 90

A Monte Carlo (MC) programs used 91

B Heavy Flavor estimation from data 93

C Misidentified leptons 95

D List of data events passed analysis cuts. 97

LIST OF REFERENCES 102

[redacted] 104

LIST OF TABLES

Table		Page
2.1	The Standard Model Fermions and their quantum numbers: electrical charge(Q), baryon number(B), lepton number(L) and spin(S).	3
7.1	Run II Electron identification cuts. As also used in the trilepton group analysis.	33
7.2	Electron ID scale factors for CDF Monte Carlo events.	35
7.3	Run II Muon identification cuts (trilepton group version).	36
7.4	Muon ID scale factors for CDF Monte Carlo events.	38
9.1	Systematic errors	45
10.1	Control Region A (Z peak).	49
10.2	Control Region B0. $\not\!\!E_T \geq 15$ GeV, no jets, back-to-back leptons.	50
10.3	Control Region C0. $\not\!\!E_T \geq 15$ GeV, no jets, not back-to-back leptons.	50
10.4	Control Region D. $\not\!\!E_T \geq 15$ GeV, no jets, back-to-back leptons.	56
10.5	Control Region E. $\not\!\!E_T \geq 15$ GeV, no jets, not back-to-back leptons.	56
10.6	Control Region B1. $\not\!\!E_T < 15$ GeV, ≥ 1 jet, back-to-back leptons.	61
10.7	Control Region C1. $\not\!\!E_T < 15$ GeV, ≥ 1 jet, not back-to-back leptons.	61
10.8	Pre-signal region before (dPhiMet_min) extra clean up cut.	68
10.9	Pre-signal region after (dPhiMet_min) extra clean up cut.	68
11.1	Cuts for different groups.	70
12.1	Cut group a results for (130/95).	82
12.2	Cut group b results.	83
12.3	Cut group c results.	84
12.4	Cut group d results.	85
D.1	$e\mu$ events.	97
D.2	ee events.	98
D.3	$\mu\mu$ events.	98

LIST OF FIGURES

Figure Page

4.1 The Fermilab accelerator complex. 11

4.2 The CDF II detector. 14

4.3 The $r - z$ view of the CDF tracking system. 16

4.4 Muon coverage in Run II. 20

5.1 Feynman diagrams for stop quark production at Tevatron 23

5.2 $\tilde{t}\tilde{\bar{t}}$ production cross section at the Tevatron 24

5.3 Stop and sneutrino mass plane showing the CDF 95% C.L. excluded region as hatched area compared to D0 and LEP2, for the three-body stop decay, $\tilde{t} \to l^+ + \tilde{\nu}_l + b$ 25

6.1 Schematic diagram for stop quark production and decay at Tevatron. . 27

8.1 Trigger efficency plots from [27] for CEM4 and CMX4. 43

10.1 Definitions of Control Regions (y axis - $\Delta\phi$ between leptons). 46

10.2 Z peak invariant mass plots with data fits (top) and MC fits (bottom). 48

10.3 $\not\!\!E_T$ plots for CR with low $\not\!\!E_T$ and no jets (B0 and C0). 51

10.4 H_T plots for CR with low $\not\!\!E_T$ and no jets (B0 and C0). 52

10.5 p_{T1} plots for CR with low $\not\!\!E_T$ and no jets (B0 and C0). 53

10.6 p_{T2} plots for CR with low $\not\!\!E_T$ and no jets (B0 and C0). 54

10.7 $\not\!\!E_T$ plots for CR with high $\not\!\!E_T$ and no jets (D and E). 57

10.8 H_T plots for CR with high $\not\!\!E_T$ and no jets (D and E). 58

10.9 p_{T1} plots for CR with high $\not\!\!E_T$ and no jets (D and E). 59

10.10 p_{T2} plots for CR with high $\not\!\!E_T$ and no jets (D and E). 60

10.11 $\not\!\!E_T$ plots for CR with low $\not\!\!E_T$ and at least one jet (B1 and C1). 62

10.12 H_T plots for CR with low $\not\!\!E_T$ and at least one jet (B1 and C1). 63

10.13 p_{T1} plots for CR with low $\not\!\!E_T$ and ≥ 1 jet (B1 and C1). 64

10.14 p_{T2} plots for CR with low $\not\!\!E_T$ and ≥ 1 jet (B1 and C1). 65

Figure Page

10.15Smallest dPhi between $\not\!\!E_T$ and any (of two) leptons or jet. 67

11.1 Expected exclusion contour. 71

11.2 Sliding cut for group a. 72

11.3 N-1 Cuts for group a for stop/sneutrino masses 130/95. 73

11.4 N-1 Cuts for group b for stop/sneutrino masses 170/110. 74

11.5 N-1 Cuts for group c for stop/sneutrino masses 180/100. 75

11.6 N-1 Cuts for group d for stop/sneutrino masses 170/60. 76

12.1 $\not\!\!E_T$ plots for pre-signal region. 78

12.2 H_T plots for pre-signal region. 79

12.3 Limit plot. 80

12.4 Observed/expected limits in a stop-sneutrino plane. 81

12.5 (N-1) $\not\!\!E_T$ plots for cut group a. 82

12.6 (N-1) $\not\!\!E_T$ plots for cut group b. 83

12.7 (N-1) $\not\!\!E_T$ plots for cut group c. 84

12.8 (N-1) $\not\!\!E_T$ plots for cut group d. 85

12.9 (N-1) H_T plots for cut group a. 86

12.10(N-1) H_T plots for cut group b. 87

12.11(N-1) H_T plots for cut group c. 88

12.12(N-1) H_T plots for cut group d. 89

B.1 Invariant mass distributions used to calculate scale factors for HF estimation from data, using inverse d0 data, lepton + fake and DY MC samples for different data periods (d,h,i) and lepton flavors (opposite sign only). 94

C.1 Plots of misidentified electrons rates for various jet trigger samples (left) and average one (right) with fake rate parametrization. 96

D.1 Event Dispay plots for signal $\mu\mu$ event (run number 165198). 99

D.2 Event Dispay plots for signal $e\mu$ event (run number 177418). 100

D.3 Event Dispay plots for signal ee (eee) event (run number 197716). . . 101

ABSTRACT

Sedov, Alexei A. Ph.D., Purdue University, May 2009. Search for the Supersymmetric Partner of the Top Quark in Dilepton Events Produced in Proton-Antiproton Collisions at $\sqrt{s}$ =1.96 TeV . Major Professor: Virgil E. Barnes.

We present a search for the lightest supersymmetric partner of the top quark $\tilde{t}$ at the Fermi National Accelerator Laboratory in proton-antiproton collisions at a center-of-mass energy $\sqrt{s} = 1.96$ TeV. This search was conducted within the framework of the R_p conserved Minimal Supersymmetric extension of the Standard Model, assuming the decay $\tilde{t} \to l^+ + \tilde{\nu}_l + b$ is dominant. We searched a total Luminosity of $\mathcal{L} = 1$ fb^{-1} of data collected by the CDF experiment looking for two leptons of opposite electric charge, jets and missing transverse energy. No statistically significant evidence of the stop signal has been found in a model with degenerate sneutrino ($\tilde{\nu}$) masses. New limits at 95% confidence level in the stop versus sneutrino mass plane have been set.

1. INTRODUCTION

For many centuries people have been trying to find fundamental units of matter and explain the nature of their interactions. As a result, four types of interactions were found: gravitational, electromagnetic, weak and strong. Many models were developed to understand the fine structure of matter based on only few basic principles. These models tried to describe the variety of experimental phenomena by means of elementary particles and their interactions which are mediated by special particles called gauge bosons.

Thus far the most successful theory is the Standard Model (SM) of Elementary Particles and Their Interactions [1]. Most of this model has been tested in detail by experiment and so far no significant deviations were found. Only one experimental exception exists, recent astrophysical measurements [2], that can't be explained within SM. It should be also mentioned that some aspects of the SM remain untested (up to date the Higgs boson is still not found).

But the more answers we get the more questions arise. New theories have been developed to answer these questions. One of the most promising is the so-called Supersymmetry (SUSY). This theory says that every particle has a supersymmetric partner which should have the same quantum numbers except for spin, which should differ by one half unit. So far no such pairs have been observed so these superpartners should be new particles. If SUSY is true then the number of all known particles is at least doubled.

It is assumed that SUSY particles are not yet found because they are heavier than their SM partners. However, in many theories the supersymmetric partner of the top quark, the stop quark, could be light enough to be produced and detected at the Tevatron. Mass mixing between the SUSY partners fo the Left- and Right-handed helicity states of the top quark is the mechanism which could drive one of the stop

states to masses even lighter than the mass of the top quark. A Search for the stop quark at CDF with Run II data is the purpose of this study.

A brief introduction to the Standard Model and its weak points are given in section 2. We introduce Supersymmetry as a solution to the problems in section 3. The experimental apparatus is described in section 4. Stop quark production and its decays are the main topics of section 5. In section 6 we introduce the experimental strategy of the search for the stop quark, a description of the data samples used, and a description of the relevant SM backgrounds and how they are modeled.

In Section 7 we describe the basic event selection. In Section 8, we describe the triggers used to collect our main data samples, and the associated trigger efficiencies. Section 9 deals with estimates of the systematic uncertainties of the data, of the various modeled backgrounds, and of the MC-modeled stop signal.

Section 10 describes the kinematic cuts used to define various Control Regions (CR) and the "preselection" region on which final optimized kinematic selections were tuned. Comparisons between data and all modeld backgrounds are shown, to validate our modeling of the SM and of detector effects. In Section 11, we describe the final optimization of (MC) signal vs. SM background, using the results of a Bayesian-statistical algorithm as a figure of merit. [This was a blind analysis, in the sense that we did not use the actual dilepton data while performing the optimizations.] Section 12 presents the results of these optimizations, including presentation of expected and observed 95% exclusion contours in the stop-sneutrino mass plane. And Section 13 is the summary.

2. THE STANDARD MODEL

2.1 The theory

The Standard Model successfully describes the variety of experimental phenomena by means of elementary particles and their interactions mediated by special particles called gauge bosons.

The SM is based on the $SU_C(3) \times SU_L(2) \times U_Y(1)$ gauge group where C stands for Color, L stands for Left and Y stands for weak hypercharge. Strong interactions are

	Generations			Q	B	L	S
	1	2	3				
Quarks	u	c	t	$+\frac{2}{3}$	$\frac{1}{3}$	0	$\frac{1}{2}$
	d	s	b	$-\frac{1}{3}$	$\frac{1}{3}$	0	$\frac{1}{2}$
Leptons	e^-	μ^-	τ^-	-1	0	1	$\frac{1}{2}$
	ν_e	ν_μ	ν_τ	0	0	1	$\frac{1}{2}$

Table 2.1
The Standard Model Fermions and their quantum numbers: electrical charge(Q), baryon number(B), lepton number(L) and spin(S).

described via $SU_C(3)$ subgroup, the ElectroWeaK (EWK) interactions are described via $SU_L(2) \times U_Y(1)$.

The Standard Model unifies several fundamental sectors. The first one describes the EWK interaction. It was developed by Glashow, Salam and Weinberg [3] and it unifies electromagnetic and weak forces. The weak interaction is transmitted by three massive gauge bosons: the charged W^+ and W^- bosons and the neutral Z^0 boson whereas the massless photon γ is the electromagnetic mediator. All these particles are mass eigenstates of the unified boson fields.

The second sector is Quantum Chromodynamics (QCD), in which the gluon, g, is responsible for the strong interactions.

According to the Standard Model, matter consists of quarks and leptons that interact with each other via exchange of gauge bosons. Quarks and leptons have spin $\frac{1}{2}$ (fermions) whereas gauge bosons have spin 1 (bosons).

Both quarks and leptons can be divided into 3 groups (generations), as shown in Table 2.1. It is convenient to make use of this classification because fermions in each generation show similar properties.

In SM all fermions participate in weak interactions, particles with electrical charge participate in electromagnetic interactions and only quarks participate in strong interactions. Special color charges were developed in order to explain the behavior of strong interactions.

Also a special quantum number, the Baryon number B, was introduced in such a way that the Baryon number of quarks is $+\frac{1}{3}$ and the Baryon number of antiquarks is $-\frac{1}{3}$. The simplest colorless objects can be constructed from quark anti-quark pair (mesons, $B = 0$), from three quarks (baryons, $B = 1$) or from three antiquarks (antibaryons, $B = -1$).

Leptons also have a special quantum number, the Lepton number L. In fact there are three lepton numbers, one for each generation of the leptons. These numbers are defined to be equal to 1 for all (two) leptons of the specific generation, -1 for antileptons of the specific generation and 0 for the other particles.

The perturbative approach is a mathematical tool that is used for calculating some parameters (e.g. cross sections) of some SM processes. That means that these parameters can be presented as power series of a small parameter (which usually includes a coupling constant). The availability of the perturbative approach is one of the advantages of the SM because it allows one to calculate some experimentally measurable quantities to a given accuracy (e.g. Leading Order (LO), Next to Leading Order (NLO) of the small parameter).

2.1.1 The Higgs scalar

If EWK symmetry were exact, SM particles would be expected to be massless in contradiction to experimental results. Therefore, EWK symmetry must be a broken symmetry at or above some scale. The most popular explanation of EWK symmetry breaking is the Higgs mechanism [1]. It introduces a spin 0 field, the Higgs field, to the SM. Its interaction with matter and gauge fields results in the particles acquiring mass.

The spontaneous breaking of the EWK symmetry by the Higgs mechanism is one of the remaining untested parts of the SM. The Higgs is responsible for most of the 19 arbitrary parameters in the theory. There is no direct experimental evidence of the Higgs scalar to this date. Furthermore, there are difficulties with the elementary scalar Higgs, the so-called *fine tuning* problem. In any quantum field theory involving interacting fundamental scalars, one finds that radiative corrections to the scalar mass produce a quadratic divergence in that mass. This divergence is unphysical because the theory is not applicable for infinite momentum; it breaks down for momenta p that approach the mass scale Λ at which new interactions or new particles become important. This scale Λ serves as a cutoff, since physics beyond SM becomes important. The Plank scale, $\Lambda = O(10^{19})$ GeV, at which gravitation becomes relevant, must be present in the theory.

Radiative corrections try to push the Higgs mass to the Plank scale

$$m_H^2 = -m_0^2 + g^2\Lambda^2,$$

where m_0 is the bare Higgs mass parameter and g is a dimensionless coupling parameter. The value of m_H is known to be of the order of the EWK scale, $O(10^{12})$ GeV. If g is of order unity and Λ is as large as the Plank scale, then m_0 must be *tuned* to incredible precision in order to keep m_H of the correct order of magnitude. While it is not impossible, it is an unpleasant feature of the Standard Model.

2.2 Problems of the Standard Model

Even though the SM describes Nature with high precision, it can not be the ultimate theory of the universe. It's an effective theory at the electroweak scale.

Some of its weaknesses are listed below :

- gravity is not included in the SM. The gravity mediator is the graviton, G, a particle with spin 2. Although the gravitational force has been known for a very long time there is still no satisfactory theory that can be used for elementary particles.

- SM has too many input parameters (such as the masses of particles). Particles get mass via interaction with the Higgs boson but there is no explanation why there are so many different coupling constants between the Higgs field and SM particles;

- recent astrophysical measurements can not be explained (dark energy, dark matter) within the SM;

- after the successful unification of EM and weak interactions a possible further unification with the strong interaction is theoretically motivated. However, SM by itself does not lead to unification of "all coupling constants";

- SM leads to quadratic divergence in radiative corrections to the Higgs boson mass.

In order to overcome the above weaknesses many theories were developed. One of the most promising is called Supersymmetry. This theory is described in detail in the next section.

3. SUPERSYMMETRY

Supersymmetry is a generalization of the space-time symmetries of quantum field theory that connects fermions and bosons. It introduces a fermionic counterpart for every boson (and vice versa) identical in all quantum numbers.

This theory proposes a new fundamental symmetry of Nature. In this way, the theory is adding something new to the existing world while including the existing SM theory as a branch.

Taking into account that boson-fermion pairs of particles with the same quantum numbers are unknown we come to conclusion that for SUSY to be true the number of particles should be at least doubled. SUSY theory with minimal number of additional particles is called the Minimal Supersymmetric extension of the Standard Model (MSSM). In MSSM each SM fermion has a supersymmetric partner - boson with exactly the same quantum numbers but the spin as the given fermion, and each SM boson also has supersymmetric fermion partner with the same quantum numbers but the spin. The names of the superpartners are usually made by adding a "s" in front of the fermion name or adding "ino" to the end of the boson name that the superpartner came from. For example, the scalar superpartner of the *top* quark is called the *stop* quark and the fermionic partner of the *photon* is called the *photino*.

Supersymmetry can not be an exact symmetry of Nature because in this case particles and their superpartners, which differ in spin by one half, would have the same masses.

The gauge interactions of the MSSM Lagrangian allow for the definition of a new multiplicative quantum number called R-parity. It is defined as: $R = (-1)^{3(B-L)+2S}$, where B is the baryon number, L is the lepton number and S is the spin of the particle as they were defined in the previous chapter. From this definition it follows that all SM particles have a $R = +1$ and all superparticles have $R = -1$.

If R-parity is conserved then all superparticles should be produced in pairs and there should be a lightest supersymmetric particle (LSP). This particle would be stable because no decay is possible. Furthermore, the decay chain of each supersymmetric particle must end with the LSP. Since we have not yet discovered a suitable candidate for the LSP, and also because of cosmological constraints, the LSP has to be electrically and color neutral, i.e. it may interact only weakly or gravitationally and therefore escape any detection. Thus the basic signature for production of the supersymmetric particles at high energy colliders is missing energy carried by LSP's.

SUSY can solve for us several problems. Some solutions are listed below :

- since fermions and bosons give opposite sign contributions to the loop diagrams for the Higgs mass, all divergences are canceled;
- LSP could be the solution of recent astrophysical observation (dark matter);
- SUSY provides a mechanism of unifying of all coupling constants;
- number of independent parameters of the model can be significantly reduced (to $4\frac{1}{2}$ in MSSM). It is possible because we have new constraints on the theory (the above unification of coupling constants).

SUSY is very promising theory beyond Standard Model. If it is true we get easy solutions of the several SM problems,

4. EXPERIMENTAL APPARATUS

In this analysis we use the Collider Detector at Fermilab (CDF). The detector is located on the main ring of the hadron collider at Fermilab at the B0 collision point of protons p and antiprotons $\bar{p}$ with a center of mass energy $\sqrt{s} \approx 2.0$ TeV [11]. Two major components necessary for the study are described in this chapter. Those two components are the Fermilab Tevatron, which provides $p\bar{p}$ collisions, and the CDF II detector, which was built to analyze the final state particles.

4.1 Tevatron

A very sophisticated accelerator complex was built at Fermilab and it is shown in Figure 4.1. One of the purposes of this complex is to provide $p\bar{p}$ collisions at very high energy. This complex consists of several parts such as Cockroft-Walton chamber, Linac, Booster, Main Injector and Tevatron. The first two are used to accelerate negative hydrogen ions. In the Booster those ions are transformed into protons. Then after acceleration in the Main Injector some of the protons are used to produce antiprotons. And finally, after acceleration in Main Injector protons and antiprotons are accelerated up to 980 GeV to be used for $p\bar{p}$ collisions in the Tevatron.

4.1.1 Cockroft-Walton Chamber, Linac, and Booster

All parts described in this section are designed to produce and accelerate the beam of protons. Part of this proton beam is used for creation of the antiproton beam.

Electrical discharges in hydrogen gas produce negative ions, which are accelerated to 750 KeV inside the Cockroft-Walton chamber. The ions are then fed through a magnetic system that gives only H^- ions as an output.

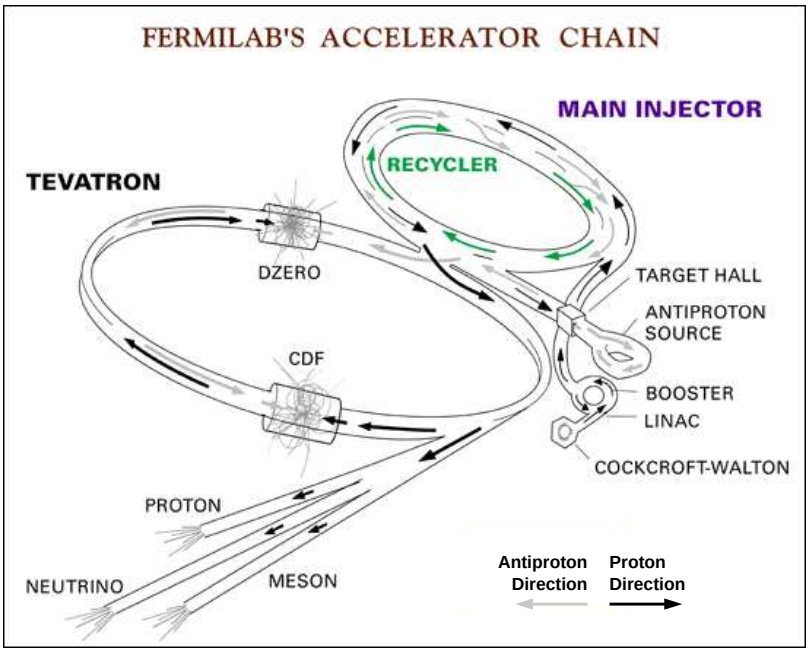

Figure 4.1. The Fermilab accelerator complex.

The Linac [12] is used to pick up those 750 KeV ions, accelerate them, and inject the ions into the Booster. The length of the Linac is about 150 meters. It can be divided into two parts. The First half-length is the Drift Tube Linac, which accelerates the ions to 116 MeV. Not so long ago the second half of the Drift Tube Linac was replaced with a Side-coupled Cavity Linac, increasing the energy of the accelerated ions to 400 MeV. At this point the whole system can deliver about 45 mA of current for about 35 msec at a 15 Hz repetition rate.

The Booster [11,13] is a synchrotron about 150 meters in diameter. The revolution period in the Booster at injection is 2.22 ms while the pulse length in the Linac is approximately 16 times longer. A portion of the Linac beam is selected by a 400 MeV *chopper* magnet while the remainder is sent to one of the two dumps. Those dumps are used for gathering information about the beam.

By extending the chop width, multiple Booster turns are generated. Although the Linac beam pulse is long enough for 16, operationally 10 or 11 turns is usually the practical limit for maximum intensity.

To increase beam intensity from the Booster the H^- beam is overlaid with the H^+ beam already circulating in the machine. The mixed beams go through a carbon foil which strips off the electrons turning the H^- into protons. To minimize beam losses the beams are made to pass through the foil only during the loading.

The resulting protons are accelerated to an energy of 8 GeV using RF cavities. The Booster can hold up to about 5×10^{12} protons simultaneously. These protons are collected into 84 bunches with up to 6×10^{10} protons per bunch. The bunches are spaced by 18.9 ns. Then accelerated 8 GeV protons are injected in the Main Injector.

4.1.2 The Main Injector, Accumulator and Recycler

The Main Injector (MI) [11] is one of the main advantages of the Run II accelerator system. The Main Injector construction was finished in 1999. Before that the protons and antiprotons in the Tevatron had been injected by the Main Ring, which was used to accelerate protons up to 400 GeV for a fixed-target experiments before the Tevatron era. Since it was originally designed for different purposes the Main Ring performance as an injector for the Tevatron was not very good. To improve this situation the Main Injector was built.

One of the main purposes of the Main Injector is to accelerate 8 GeV protons or antiprotons to 150 GeV and inject them into the Tevatron. The MI accelerates protons from the Booster to 120 GeV and delivers them to the antiproton production target, to fixed target and neutrino experiments.

The largest problem in setting effective $p\bar{p}$ collisions is to have a significant number of antiprotons confined in a small phase space volume. To reach this goal the Accumulator and the Recycler were built. The Accumulator keeps the produced antiprotons at 8 GeV energy. Then those antiprotons are injected into the MI to be accelerated to the needed energy. The Accumulator ring is about the size of the Booster which has a circumference 7 times smaller than the circumference of the MI.

The Recycler [11, 14] is built inside the MI tunnel. Its purpose is to store the antiprotons that were left at the end of the store, the period of time when collisions occur. At the end of the store antiprotons are returned to the MI to be decelerated from 150 GeV to 8 GeV. Then those antiprotons are collected in the Recycler which keeps them at 8 GeV energy. Use of different kinds of cooling techniques in the Recycler allows a reduction in space volume and keeps antiprotons within this volume which are the ultimate tasks of the upgrade [15].

4.1.3 Tevatron

The Tevatron is at present the largest energy collider in the world. It is 2 km in diameter and is used to accelerate 150 GeV protons and antiprotons from MI to an energy of 980 GeV, providing a center of mass energy of almost 2 TeV. To reach such high center of mass energy superconducting magnets are used.

The Run II goal is to collide 36 bunches of protons with 36 bunches of antiprotons, so-called 36×36 scheme. This scheme allows collection of data with instantaneous luminosity presently around 3×10^{32} cm^{-2}s^{-1}. Instantaneous luminosity is a quantity that is proportional to the number of collisions per unit of time and is given by :

$$\mathcal{L} = \frac{N_{\bar{p}} N_p N_B f}{4\pi\sigma_A^2}, \tag{4.1}$$

where $N_{(\bar{p}),p}$ is the number of the (anti)protons in a bunch, N_B is the number of bunches, f is the bunch revolution frequency and σ_A is the cross-sectional area of the beam. The particle losses (reduction of N_p and $N_{\bar{p}}$) and heating of the beams (increase of σ_A) result in reduction of the instantaneous luminosity with time.

A More useful quantity is the integrated luminosity which is an integral of the instantaneous luminosity over time. The integrated luminosity is used to get the total number of events observed which is given by :

$$N = \sigma \int \mathcal{L} dt,$$

where σ is the cross section for a given process.

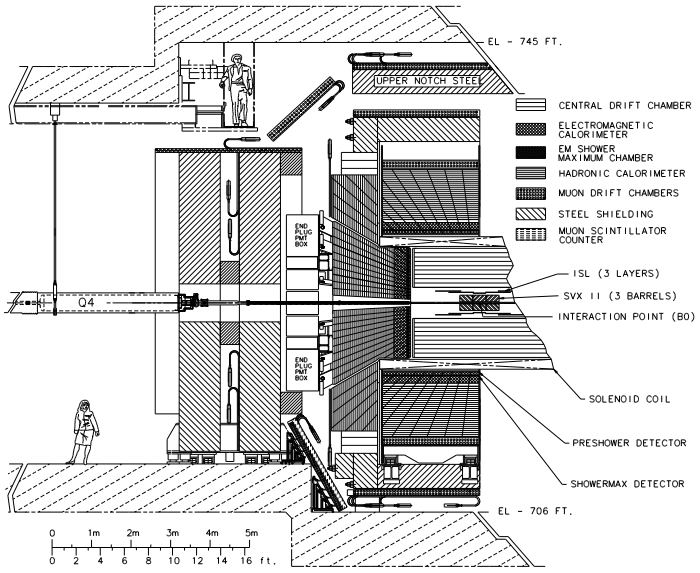

Figure 4.2. The CDF II detector.

4.2 The CDF II detector

In this section we describe the CDF II detector [16]. It can be divided into several major parts. Those parts are tracking system, magnet, calorimetry and muon detectors.

Let us define coordinate systems that will be used for the description of CDF II detector. Three systems are commonly used: Cartesian, polar and cylindrical. It is convenient to use the geometric center of the detector as a common origin of these coordinate systems. The axes of the Cartesian coordinate system are defined as follows. The x axis is in the plane of the accelerator ring, pointing radially outward, and the y axis points vertically up. The z axis is chosen so as to complete the right-handed coordinate system. In such coordinate system beams travel through the center of the detector in such a way that protons move in the positive z direction and antiprotons move in the negative one.

Since the detector is cylindrically and forward-backward symmetric it is also convenient to use cylindrical (r, ϕ, z) and polar (r, ϕ, θ) coordinate systems. The z axis is the same for the cylindrical as for the Cartesian coordinate system. The azimuthal angle ϕ lies in the $(x-y)$ plane and is counted from the positive x axis while the polar angle θ is counted from the positive direction of the z axis. Very often pseudorapidity, η, is used instead of θ. Pseudorapidity is defined as

$$\eta = -\ln \tan \theta/2 \tag{4.2}$$

4.2.1 Tracking system

The tracking system plays a very important role in the understanding of particles, produced in $p\bar{p}$ collisions. The CDF Run II tracking system uses a well known property of charged particles to cause ionization as they pass through matter.

There are two major parts of the CDF Run II tracking system. Those parts are: the Central Outer Tracker (COT) and the Inner Tracker, which in turn consists of the Silicon VerteX Detector II (SVXII) and the Intermediate Silicon Layers (ISL).

The Central Outer Tracker (COT) is a cylindrical multi-wire open-cell drift chamber that covers the region $\mid \eta \mid < 1$ in pseudorapidity and radii between 44 and 132 cm. The COT has 8 radially spaced superlayers. The number of cells in the superlayer varies from 168 for layer 1 to 480 for layer 8. Each cell includes 12 sense wires. Four COT superlayers have cells with zero stereo angle, they are called axial superlayers. The other four superlayers are called stereo superlayers, because two of them have stereo angle $+3^\circ$ and the other two have stereo angle -3°. Thus, in the COT four axial and four stereo super-layers with 12 wires each will provide 96 measurements between 48 and 131 cm, using a total of 30,240 readout channels for the entire detector. Small drift cells and fast gas lead to less than 100 ns in COT drift time. The correlation of COT tracks with Electro-Magnetic calorimetry and muon chamber information is the basis of lepton identification.

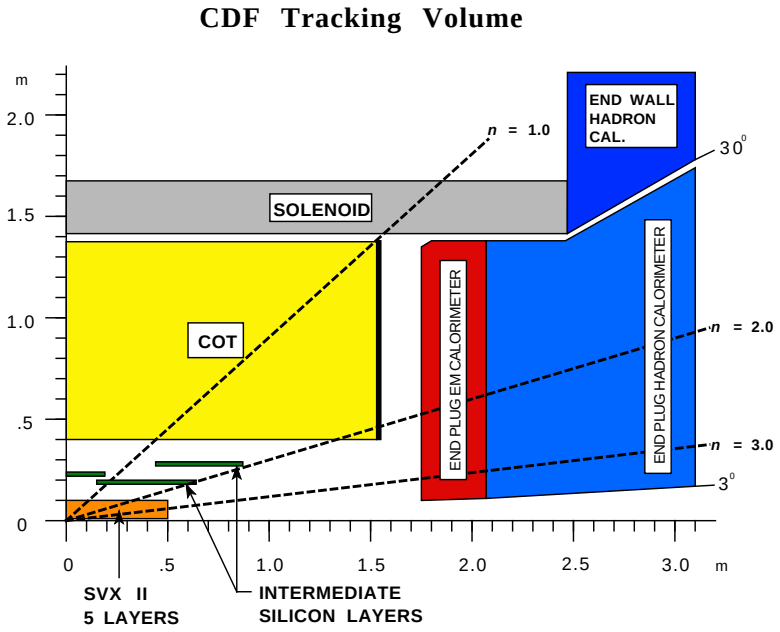

Figure 4.3. The $r - z$ view of the CDF tracking system.

The Silicon Vertex Detector II has three cylindrical barrels with a total length of 96 cm. Each barrel supports five layers of double sided silicon microstrip detectors between radii of 2.4 and 10.7 cm. Three of the layers combine an $r - \phi$ measurement on one side with 90° stereo measurement on the other. The remaining two layers combine $r - \phi$ with small angle stereo at 1.2°. The silicon crystals are supported by low mass substrates, "ladders". Twelve ladders of the appropriate width make a layer.

ISL is located between SVX II and COT. It has five cylindrical silicon detectors. A single ISL layer is placed in the central region at a radius of 22 cm. In the region $1.0 < |\eta| < 2.0$ two layers of silicon are placed at radii of 20 cm and 28 cm. Double sided silicon is used with 55 μm strip pitch on the axial side and 73 μm pitch on the stereo side with a 1.2° stereo angle.

The combination of SVX II and ISL is a single functional system which provides stand-alone silicon tracking and b-tagging over the full region $|\eta| \leq 2.0$

4.2.2 Calorimetry

Calorimetry of the CDF detector has η coverage from -3.6 to 3.6 . It consists of Central Electro-Magnetic (CEM) and Central HAdron (CHA), Wall HAdron (WHA), Plug Electro-Magnetic (PEM) and Plug HAdron (PHA) calorimeters.

The Wall and Central calorimeters cover 2π in azimuth and were intact since Run I while the Plug calorimeter was one of the major upgrades for Run II. CEM covers the region from -1.1 to 1.1 in η while WHA and CHA cover from -1.3 to 1.3 in η. In turn Plug calorimeters extend η coverage to 3.6 .

Calorimeters measure the energy of a particle by "absorbing" it in a medium and measure the deposited energy. In the CDF calorimeters it is done by having two kinds of layers, the absorber material (with a high nuclear number Z), and the active read out material. The energy deposited by a charged particle is dissipated mostly in the absorber and a small fraction in the read out material. The total deposited energy is proportional to the amount absorbed in the read out material, therefore, by measuring the signal from the active read-out (which are scintillators) we can deduce the actual deposited energy. The energy of neutral particles can be measured in general only by determining the energy imbalance in the detector, however the photons are measurable in the electromagnetic calorimeters and neutral hadrons leave energy in the hadron calorimeters.

The calorimeters are segmented in azimuth and pseudorapidity to form a projective "tower" geometry which points back to the nominal interaction point. The collision product meets the EM part first, which is used to measure the energy of electrons and photons, then the HAD part, which deals with the hadronic particles.

The central calorimeter is made up of 24 wedges and is placed around the beam pipe, so one wedge covers 15°. In the polar direction, one wedge is made out of 10 towers, all of them pointing to the center of the detector and each tower covers $\eta < 0.1$. Towers 0-5 of CEM continue to CHA , towers 6-9 continue to CHA but share their ends with WHA.

The CEM uses polystyrene scintillator as the active read out material (31 layers each 5 mm thick) and lead as the absorber material (30 layers each 1/8 inch thick). The scintillator's light is collected through wavelength shifter bars on both sides of the wedge. The wavelength shifters transmit the light through acrylic light guides which are attached to photomultipliers located at the rear end of each wedge . The fractional energy resolution for CEM is

$$\frac{\sigma(E)}{E} = \frac{13.5\%}{\sqrt{E_T/1GeV}} \oplus 2\%$$

There are proportional chambers embedded within the CEM, called the Shower Max Detector (CES) and the Pre-Shower Detector (CPR).

The CPR is located between the front face of the CEM and the surface of the solenoid. It gives information about early showers. The CES , a gas wire chamber, is located at 6 radiation lengths within the CEM and reads out the transverse profile of the EM showers.

The CHA is located behind the CEM. It uses the same read out material as the CEM, but the absorber is steel. It contains 32 layers of 1.0 cm thick scintillators and 2.5 cm thick steel. The WHA has more steel, since for the same E_T the E of the particles which get to the WHA is greater. WHA is made out of 15 layers of 1.0 cm scintillators and 5.0 cm steel. The proportional resolution is given by

$$\frac{\sigma(E)}{E} = \frac{75\%}{\sqrt{E_T/1GeV}} \oplus 3\%$$

The above resolutions are measured using the test beam and the radioactive source.

The plug region $1.1 < |\eta| < 3.6$ is covered by the plug electromagnetic calorimeter (PEM) and the plug hadron calorimeter (PHA). The plug calorimeter, both PEM and PHA, is divided into twenty four 15° segments in ϕ. Each segment has 20 (PEM) and 18 (PHA) physical towers. Those towers are combined into six trigger towers. Extending the CEM/WHA tower numbering scheme, we get 12 (PEM) and 11(PHA) towers for a given ϕ pointing to the center of the detector.

The PEM is a lead/scintillator sampling calorimeter, with unit layers composed of 4.5 mm lead and 4 mm scintillator. There are 23 layers in depth for a total thickness of about 21 radiation lengths at normal incidence. The resolution of the PEM is

$$\frac{\sigma(E)}{E} = \frac{16\%}{\sqrt{E/1GeV}} \oplus 1\%$$

The PHA is an iron/scintillator sampling device. It is made out of 23 layers and each layer in turn is composed of 2 inch iron and 6 mm scintillator. The resolution is given by

$$\frac{\sigma(E)}{E} = \frac{80\%}{\sqrt{E/1GeV}} \oplus 5\%$$

Similar to the CEM, the Plug calorimeter has Shower Max (PES) and Pre-Shower detectors (PPR). They help to determine the position of the shower. PES is a scintillator strip detector placed at a depth of approximately 6 radiation lengths inside the PEM calorimeter, while modified layer 0 of PEM represents PPR.

4.2.3 Muon detection

The CDF muon system consists of four main subsystems. Central MUon (CMU) and Central Muon uPgrade (CMP) detectors have η coverage from -0.6 to 0.6, Central Muon eXtension (CMX) covers $0.6 <| \eta |< 1$ and the last subsystem, Intermediate MUon detector (IMU), covers $1 <| \eta |< 1.5$.

As a result of the Run II upgrade central region ($| \eta |< 1$) coverage was improved (see Fig. 4.4) as well as a new muon detector, IMU, was installed.

Muons which get to the muon chambers usually have high p_T tracks in the COT and very little energy deposited in the calorimeters. The central region is covered by 3 parts, the CMU, CMP and CMX.

The CMU is is a drift chamber built on the top of the CHA wedges. It is divided into 24 wedges, each 15° in the azimuthal direction. In the polar direction it covers $|\eta| < 0.63$ but the active region is in fact smaller, namely only 84% of the solid angle due to the 2.4° gaps between the wedges. In addition to these gaps, there is a 1.5° (about 18cm) gap at $\eta = 0$ between the East and West arches.

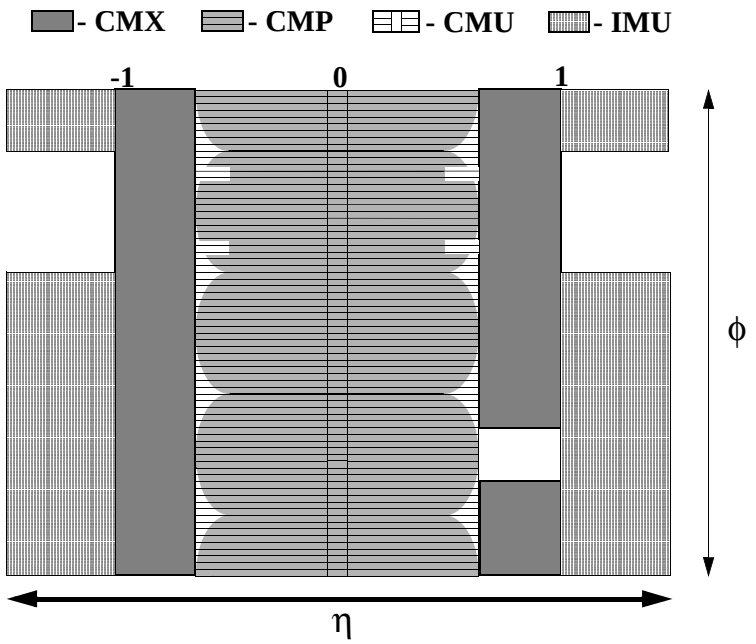

Figure 4.4. Muon coverage in Run II.

Each wedge consists of three 4.2° chambers. Inside a chamber the detector is divided into 16 drift cells made out of 4 layers and 4 towers. It provides 3-dimensional reconstruction of the tracks for muons which were able to get to the muon system, i.e. muons with p_T at least 1.5 GeV since approximately 5 hadronic absorption lengths of the central calorimeters separate the muon system from the interaction point. A mixture of argon and ethane fills the chambers. Anode wire pulses in each of the four layers are made as the muons traverse through them and leave an ionization trail behind. The path of the muon in $r - \phi$ is deduced by measuring the time of arrival of each pulse. By off-setting the top two planes of the wires from the bottom two, one can resolve the left right ambiguity. By measuring the pulse hight at both ends of the anode wire the z-coordinate can be measured. The resolution in $r - \phi$ is 250 μm and 1.2 mm in z.

The CMP sits on the steel absorber behind the CMU. The purpose of the steel absorber is to absorb the "punch through's", hadrons leaving the CHA, which would

fire the CMU. Muons which get to the CMP must have at least $p_T = 2.2$ GeV to penetrate all the intervening material. The steel reduces the punch-through rate by a factor of ~ 10. The CMP consists four layers of rectangular single-wire drift tubes, running in proportional mode. The CMP detector has the shape of a rectangular box with walls having equal length in z. This analogy is only approximate and some of the CMP walls are made of several sections, not lying in the same plane, that leads to smaller coverage. There are several reasons for this such as location of the cables, serviceability, etc. For Run II CMP coverage has been expanded to close azimuthal gaps wherever possible.

The next part, the CMX, extends the CMU to the region $0.6 < |\eta| < 1.1$. Each 15° wedge is made up of 8 layers of drift tubes with 6 tubes in each layer. These tubes differ from those used in the CMP only in length. Although the increase of the coverage was one of the accomplished goals of the Run II upgrade, the CMX does not cover all the possible solid angle due to cracks.

The data from the forward region is not used in the preliminary analysis and the details of the forward muon systems as well as the previous parts can be found in [16].

4.2.4 Trigger system

The inelastic $\bar{p}p$ cross section at $\sqrt{s} = 1.98$ TeV is around 60 mb. Since we are limited by the existing electronics, we cannot record all these events and analyze them. We need to make preselections and write only the events that contain the basic signatures of the physics one is interested in. In order to do this, CDF has three levels (L1, L2 and L3) of triggers. The L1 and L2 triggers are combinations of hardware and software, L3 is purely software.

In general, the triggers use the tower nature of the calorimeters and some tracking information coming either from the CMX chambers (see the previous section) or from an eXTRaPolator unit (XTRP) which is responsible for quick extrapolation of tracks from the eXtremely Fast Tracker (XFT) to other detector subsystems. The trigger

towers are 15° in ϕ direction and 0.2 in the polar direction η. At level 1 triggers, the decision to select or reject the event is made within 3.5 μs , and the incoming rate of events (7.6 MHz) is reduced to about 50 kHz (Note that a bunch crossing is the definition of an event, therefore we can have more then one $p\bar{p}$ interaction in an event.). Then the level two trigger further reduces this number to 300 Hz and the level 3 trigger reduces this number to about 5 to 8 Hz.

5. STOP QUARK AT THE TEVATRON

Since the top quark is the presently heaviest observed fermion, in many theories the stop may be the lightest scalar quark.

5.1 Production

In R-parity conserved MSSM stop quarks are produced in pairs. Feynman diagrams for dominant stop production processes at the Tevatron are shown in Figure 5.1

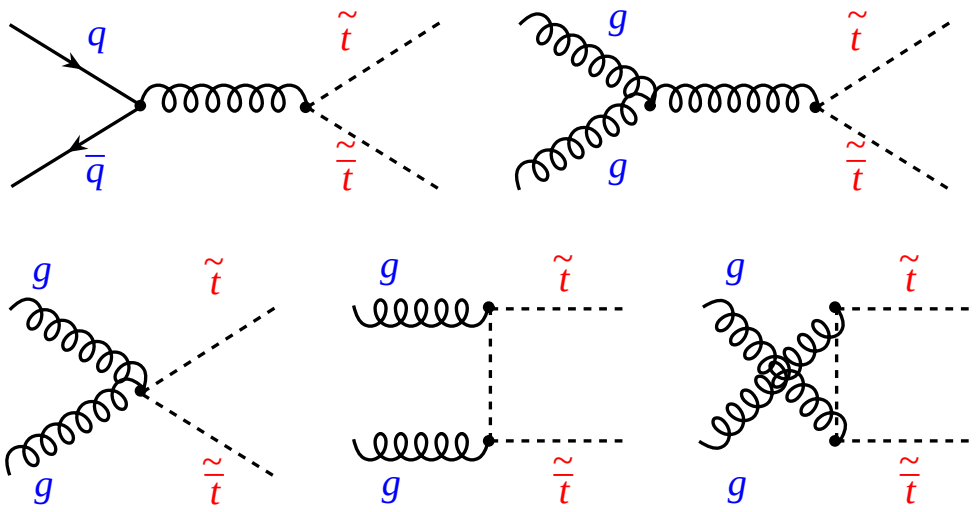

Figure 5.1. Feynman diagrams for stop quark production at Tevatron

The $\tilde{t}\bar{\tilde{t}}$ production cross section at the Tevatron calculated in next-to-leading order QCD using the PROSPINO program [7] for the stop masses varying from 50 to 200 GeV is shown in Figure 5.2, using the CTEQ6 Parton Distribution Function (PDF) and setting the renormalization and factorization scale, Q, to the stop mass, $m_{\tilde{t}}$. The yellow band is the theoretical uncertainty (≈20%) on stop cross section.

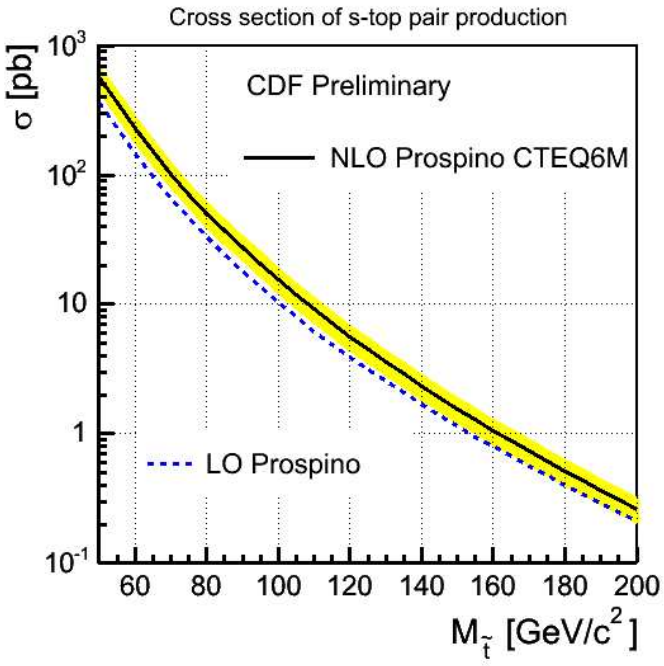

Figure 5.2. $\tilde{t}\bar{\tilde{t}}$ production cross section at the Tevatron

5.2 Decay

In order to decay via strong decays the stop quark would have to have a mass higher than that of the top quark. In R_p-conserving models the dominant decay would be $\tilde{t} \rightarrow t\tilde{g}$ if kinematically allowed. Another interesting decay would be $\tilde{t} \rightarrow t\tilde{\chi}_1^0$ which would be the dominant decay if $\tilde{g}$ has a large mass and the strong two-body decay is then not allowed. With the available luminosity we estimate our "reach" for stops to be at or not far above the top mass. Given the LEP limit on $\tilde{g}$ and $\tilde{\chi}_1^0$ masses [5], [6], the above decay modes would not be relevant to the present analysis.

In Tevatron Run I stop masses below the top quark mass were not excluded. For this area of stop masses the 2-body decay $\tilde{t} \rightarrow \tilde{\chi}_1^+ b$ should be a dominant one, if kinematically allowed. The LEP2 limit for $\tilde{\chi}_1^+$ is about 103 GeV/c^2 and the limit for the stop quark from CDF in Run I is 130 GeV/c^2 (See Figure 5.3) [9, 17].

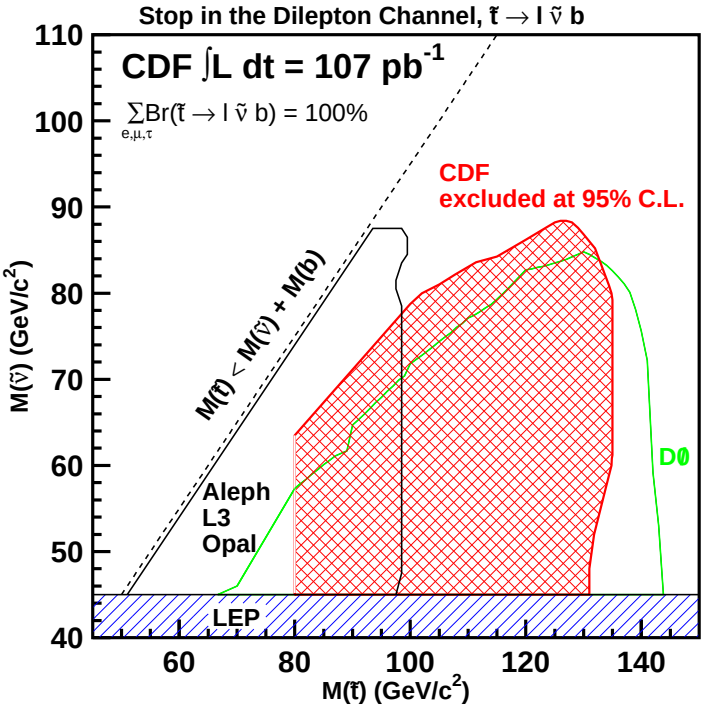

Figure 5.3. Stop and sneutrino mass plane showing the CDF 95% C.L. excluded region as hatched area compared to D0 and LEP2, for the three-body stop decay, $\tilde{t} \rightarrow l^+ + \tilde{\nu}_l + b$

If the chargino is considered on-shell then the stop should have mass $m_{\tilde{t}} \geq 130$ GeV/c^2 and chargino mass should be 103 GeV/$c^2 \leq m_{\tilde{\chi}_1^+} < m_{\tilde{t}} - m_b$. Two b-quark jets and objects from the chargino decays are the signature of such stop events in the detector.

Let's consider decay modes for an on-shell chargino in this interval of masses.

$\tilde{\chi}_1^+ \rightarrow W^+\tilde{\chi}_1^0$ decay mode is kinematically forbidden due to currently existing neutralino limits.

Since squarks are too heavy then the $\tilde{\chi}_1^+ \rightarrow \tilde{q}\bar{q}'$ decay mode is also not allowed.

So the most promising decay modes are leptonic decays. These modes are $\tilde{\chi}_1^+ \rightarrow \tilde{l}\nu_l$ or $\tilde{\chi}_1^+ \rightarrow l\tilde{\nu}_l$. Since the slepton decays into lepton and neutralino then the signature for either decay mode will be two opposite sign leptons and missing energy. In this analysis we do not consider slepton decays.

If the chargino mass is larger than the stop mass then we will have an off-shell chargino and direct three body decay modes for the stop. Using similar arguments we conclude that leptonic decays dominate. Thus a very promising signature for stop decays in the detector is two b-jets, two opposite sign leptons and missing energy.

6. DESCRIPTION OF THE ANALYSIS

6.1 Search strategy

The decays of interest are the following :

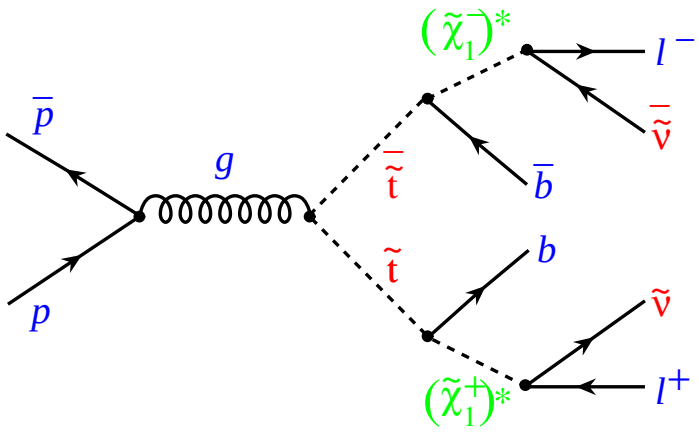

Figure 6.1. Schematic diagram for stop quark production and decay at Tevatron.

$$\tilde{t} \rightarrow (\tilde{\chi}_1^+)^* + b$$

$$(\tilde{\chi}_1^+)^* \rightarrow l^+ + \tilde{\nu}_l$$

$$\bar{\tilde{t}} \rightarrow (\tilde{\chi}_1^-)^* + \bar{b}$$

$$(\tilde{\chi}_1^-)^* \rightarrow l^- + \bar{\tilde{\nu}}_l$$

Let's consider the resulting particles in the detector. Neutrinos and LSPs are weakly interacting neutral particles. They can't be observed directly in the CDF Run II detector [16]. Indirect detection is possible via energy imbalance as they are carrying part of the total energy. Since some of the particles in the event can leave

the detector through the beam pipe, it is standard to look for the energy imbalance only in a plane perpendicular to the beam direction, the $x-y$ plane. Such imbalance is called missing transverse energy ($\not\!\!E_T$). The b quark produces a jet of particles: a b-jet. So each event of interest manifests itself in the detector via :

- two opposite sign leptons

- two b-jets

- significant missing transverse energy

Each of these objects can be detected with some efficiency. So the final result depends on the combined efficiency of each component. Since the efficiency of tagging b-jet is rather small and requires special subdetectors, in this study we are looking for events with two leptons, missing transverse energy and at least one jet. This is only one way for searching stop in the above channel and one could look for two b-jets, missing energy and at least one lepton assuming that the second one can be very soft and it can be missed. We do not search for this latter signature.

If the chargino mass is significantly higher than the sum of the masses of its lepton-sneutrino decay products, then each charged lepton contributes equally to the decay of the chargino, by "lepton universality". If the three generations of sneutrinos are mass-degenerate, this means that $\frac{1}{3}$ of all leptonic decays of chargino should have electrons in the final state, $\frac{1}{3}$ should have muons and $\frac{1}{3}$ should have taus.

Electrons and muons are long lived particles and it is possible to detect them with the CDF detector. It is reasonable for this study to look for decays that have muons and/or electrons in the final state.

Muon and electron decays constitute $\frac{2}{3}$ of all leptonic chargino decays. Taking into account that two stops produce two charginos, we expect to have muons and/or electrons in at least $\frac{4}{9}$ of all leptonic chargino decays. This number characterizes the sensitivity of this study.

The situation with tau is more complicated because the tau lifetime is short and it decays well inside the CDF detector. Lepton (muon and electron) decays constitute

only about 36% of all tau decays. Still addition of such decays helps to increase the fraction of events with muons and/or electrons from chargino in the final state up to $\approx \frac{5}{8}$.

6.2 Data samples

In the analysis we used exotic dilepton trigger samples (edil in CDF patois) up to the CDF run period 7 with total integrated luminosity (in other CDF patois, run groups d, h and part of i)

$$\mathcal{L} = 310\text{pb}^{-1} + 388\text{pb}^{-1} + 269.2\text{pb}^{-1} = 0.9672\text{fb}^{-1}$$

This luminosity was calculated for GoodRun list (1,0,1,1) version 13. This GoodRun list includes runs for our data periods with good showermax detectors (for electrons), good muons chambers (for muons), no requirements on working silicon detector as well as exclusion of runs in the beginning of the Run II (with run number <141544).

6.3 SM Backgrounds from Monte Carlo

Higher orders diagrams in QCD could give jets which pass the stop cuts. And mismeasured leptons and/or jets could give $\not\!\!E_T$.

There are several SM background that give us two leptons, $\not\!\!E_T$ and at least one jet. Those backgrounds are :

- $t\bar{t}$
- Heavy flavor production ($b\bar{b}$, $c\bar{c}$)
- Drell-Yan production of lepton pairs plus jets.
- WW, WZ, ZZ production ("Di Boson")
- misidentified leptons

Let's consider each of the backgrounds in detail. Information on the particular CDF MC samples that we used for $t\bar{t}$, DY and Di Boson backgrounds is given in Appendix A.

Top quark

We put the decay of top quark in first place since the decay signature should be similar to that of the stop quark. The only difference is that $\tilde{\nu}$ should take a larger fraction of the stop energy leading to a softer spectrum of visible particles than in top decay.

Heavy flavor

$b\bar{b}$ and $c\bar{c}$ events have higher cross sections than $t\bar{t}$ events. Semileptonic decays of these quarks (via off-shell W) produce leptons and neutrinos and jets. But since the available kinetic energy in these decays is not large compared to the parent quark masses, their momenta are very much correlated with the momentum of the original quark. Thus jets and leptons from b or c quarks should be together in a small cone, whereas in stop decays they are well isolated from each other because they come from the decay of a much heavier particle.

Since the Heavy Flavor (HF) production cross sections are very high and we are interested only in tiny part of them (with two isolated leptons and large $\not\!\!E_T$), it's very hard to get a HF MC sample that would be adequate to our purpose.

Taking into account the above considerations we decided to estimate HF contribution to our analysis from data, making use of secondary-vertex impact parameters measured either in the Silicon Tracker (SVX) (when available) or the Central Outer

Tracker (COT) drift chamber. The detailed technique of HF estimation from data is given in Appendix B.

Drell-Yan + jets

Direct lepton-antilepton pair production via real or virtual photon (γ) or Z boson, the Drell-Yan process [19] with higher order QCD processes (jets), is another source of the SM background.

Mismeasured energies of jets or leptons could lead to $\not\!\!E_T$. In the case of $\tau^+\tau^-$ production leptonic decays could also mimic stop decays.

Diboson background

Another source of SM background is production of pair of weak vector bosons. Decay of each boson could give at least one lepton. Jets could come either from hadronic Z or W decay in ZZ, WZ or from higher order QCD processes. $\not\!\!E_T$ can come from mismeasurements of jets and/or leptons as well as from the escaping neutrinos.

Misidentified leptons

The last source of SM background is events with "misidentified leptons", either hadrons misidentified as leptons or uninteresting leptons from decays in flight of pions and kaons. These events could play a very important role in understanding the analysis. In the Run I analysis [17, 32], such misidentified leptons were comparable in number to the Standard Model backgrounds and required careful tuning of cuts based on special event samples.

Pure Monte Carlo and Detector Simulation events are not adequate for this job. It is necessary to use real events from CDF data samples which are not a part of the stop search sample. Detailed information on the estimation of such events is given in Appendix C.

7. BASIC EVENT SELECTION

For all our studies we apply a preliminary and common event selection. This includes the application of the good run list as described in section 6.2 and the following requirements

- One good primary vertex : We require the presence of a vertex reconstructed with the ZVertex algorithm having Quality 12 or higher. This vertex should be found within 60 cm from the nominal interaction point.

  In case more than one vertex in the ZVertexCollection satisfies this criterion, the one with the highest $\sum p_T$ (scalar sum over all the tracks used in the vertex fit) is used as the vertex of the event.

- The standard Cosmic Ray Tagger is applied to the events in data (not in simulation) in order to reduce the presence of cosmic muons in the events.

- We require the presence of two leptons, being either muons or electrons, as well as at least one jet and $\not\!\!E_T$, all passing corresponding ID cuts and minimum energy requirements as described in the following subsections.

7.1 Electron

Electrons are detected by the electromagnetic calorimeter and tracking systems. In the calorimeter, incoming electrons interact with the EM field of atomic nuclei or interact with atomic electrons to give e^+e^- pairs or photons or knock-on electrons, all of which in turn create more electrons and/or photons. So instead of a single electron we detect a shower of electrons and photons. This shower is largely complete before the hadron calorimeter. Taking into account that neutral photons leave no track

Central Electron Variable	Cut
E_T	$\geq$ **4.0** GeV
p_T	$\geq$ 4.0 GeV
E_{had}/E_{em}	$\leq$ 0.055+0.00045*E
E/P	$\leq$ 2.0 .OR. $p_T > 50$ GeV
L_{shr}	$\leq$ 0.2
$\|\Delta z\|$	$\leq$ 3.0 cm
Q * Δx	$\geq$ -3.0 cm, $\leq$ 1.5 cm
χ^2_{strip}	$\leq$ 10.0
COT exit Radius	$\geq$ 140 cm
Hits for a COT good segment	$\geq$ 5
Good COT Axial Segments	$\geq$ 3
Good COT Stereo Segments	$\geq$ 2
Fiducial	Yes
$\|z_0\|$	$\leq$ 60.0 cm
Conversion	Veto
Absolute Isolation	$\leq$ 2.0 GeV if $E_T > 20$GeV
Fractional Isolation	$\leq$ 0.1 if $E_T \leq 20$GeV
$\|d_0\|$	$\leq$ 0.2 cm if no Si hits
$\|d_0\|$	$\leq$ 0.02 cm if Si hits

Table 7.1
Run II Electron identification cuts. As also used in the trilepton group analysis.

in the tracking detectors, track information helps separate electrons from photons hitting the calorimeter.

To identify electrons we used the standard CDF clustering algorithm which finds towers where shower energy is deposited - so-called seed and shoulder towers : 3 towers in the polar direction (adjacent in η) with the same ϕ direction. Several variables are used to identify electrons in the CDF detector. These variables are :

- the transverse energy E_T of the electron calorimeter cluster, a correction for the beam position is applied to E_T ;

- the transverse momentum p_T of the track associated with the electron;

- the ratio E/P of the cluster energy to the track momentum. We expect this ratio to be around 1 although some moderate deviations are allowed;

- the calorimetric ratio E_{HAD}/E_{EM} of the hadronic energy to the electromagnetic energy of the cluster. This ratio should be small because only a small part of the electron energy is deposited in the hadron calorimeter. Since the EM shower penetrates deeper for higher incident energy this ratio depends on the electron energy;

- the lateral shower profile L_{shr} is defined as :

$$L_{shr} \equiv 0.14 \times \sum_i \frac{E_i^{adj} - E_i^{expect}}{\sqrt{0.14^2 \times E^{clust} + (\Delta E_i^{expect})^2}},$$

  where the sum runs over two towers adjacent to the seed tower such that all three towers are from the same azimuthal wedge, and E^{clust} - energy of the cluster, E_i^{adj} - energy of the adjacent tower, E_i^{expect} is the expected energy calculated from the projected electron track and ΔE_i^{expect} is the associated uncertainty;

- Δz is the difference in z, at the radial position of the EM calorimeter, between shower center in the Central Electromagnetic Shower Maximum Detector(CES) and the projected position of the corresponding track.

- the number of hits in the COT that are used to characterize the "goodness" of the track. The more hits you have the better the quality of the reconstructed track;

E_T (GeV)	Data/MC
5-8	0.74±0.1
8-12	1.0±0.02
12-16	1.0±0.023
16-20	1.04±0.03
>20	0.986±0.004

Table 7.2
Electron ID scale factors for CDF Monte Carlo events.

- the z_0 (at the beam line) of the beam-constrained COT-only track.

- the isolation is defined as total transverse energy in a cone of 0.4 about the electron, divided by E_T of the calorimeter cluster for fractional isolation;

- the impact parameter (distance of closest approach) of the track with respect to the primary vertex.

We use the CDF trilepton group electron ID cuts that were used by CDF for conferences in 2004-2009 [20]. The cuts are shown in Table 7.1. We apply those cuts to all electron-like objects in the events of the analysis. Electrons were required to pass all of the cuts. Electron candidates which failed only the d0 (transverse impact parameter) cuts were used in the data-based HF estimation.

The efficiency of finding an electron after using the above ID cuts was studied in di-electron trigger under the trilepton search [21]. ID scale factors used in that analysis are shown in Table 7.2.

Central Muon Variable	Cut
p_T	$\geq$ **4.0** GeV
E_{had}	$\leq$ max(6,6+0.0280(p - 100)) GeV
E_{em}	$\leq$ max(2,2+0.0115(p - 100)) GeV
COT exit Radius	$\geq$ 140 cm
Hits for a COT good segment	$\geq$ 5
Good COT Axial Segments	$\geq$ 3
Good COT Stereo Segments	$\geq$ 2
$\|z_0\|$	$\leq$ 60.0 cm
Cosmic	Veto
CMU $\|\Delta x\|$	$\leq$ 7.0 cm if $p_T >$ 20GeV
CMU $\|\Delta x\|$	$\leq$ 7.0 cm.OR.$\chi^2 < 9$ if $p_T \leq$ 20GeV
CMP $\|\Delta x\|$	$\leq$ 5.0 cm if $p_T >$ 20GeV
CMP $\|\Delta x\|$	$\leq$ 5.0 cm.OR.$\chi^2 < 9$ if $p_T \leq$ 20GeV
CMX $\|\Delta x\|$	$\leq$ 6.0 cm if $p_T >$ 20GeV
CMX $\|\Delta x\|$	$\leq$ 6.0 cm.OR.$\chi^2 < 9$ if $p_T \leq$ 20GeV
Fractional Isolation	$\leq$ 0.1 if $p_T >$ 20GeV
Absolute Isolation	$\leq$ 2.0 GeV if $p_T \leq$ 20GeV
$\|d_0\|$	$\leq$ 0.2 cm if no Si hits
$\|d_0\|$	$\leq$ 0.02 cm if Si hits

Table 7.3
Run II Muon identification cuts (trilepton group version).

7.2 Muon

To detect muons, information from muon detectors, calorimeters and central trackers is needed. Hits in the muon detectors are matched to a track from the tracking system. Then corresponding projected calorimeter information is used.

Several variables are used to identify muons at the CDF detector. These variables are :

- the transverse momentum of the track associated with the muon;
- the energies E_{EM}, E_{HAD} deposited in the electromagnetic and hadron calorimeters. Those values are expected to be small, since the muon generally does not interact in the calorimeter, except for minimum-ionization energy loss.
- the number of hits in COT that are used to characterize the "goodness" of the track;
- the z_0 of the beam-constrained COT-only track.
- the isolation is defined as total transverse energy in a cone of 0.4 about the muon, divided by p_T for fractional isolation;
- the distance between the stub in the muon chamber and the expected hit from the corresponding track from the tracker, as well as χ^2 of the fit.
- the impact parameter of the track with respect to the primary vertex.

We apply a correction which takes into account the initial beam position in the $x - y$ plane [24] to p_T of the muon in data, while the p_T of MC muons is left intact (v6.1.4 MC, CDF jargon).

We use the trilepton group muon ID cuts that were used by CDF for conferences 2004-2009 [20]. The cuts are shown in Table 7.3. We apply these ID cuts to all muon-like objects in the events of the analysis. Muons were required to pass all of the cuts. Muon candidates which failed only the d0 transverse impact parameter cuts were used in the data-based HF estimation.

The efficiency of these muon above ID cuts was studied in [22] and [23]. ID-efficiency scale factors used in this analysis are shown in Table 7.4.

p_T ≥20 GeV	run period d	run period h	run period i
CMUP	0.9360±0.0055	0.9286±0.0050	0.9174±0.0064
CMX	1.0098±0.0057	0.9931±0.0056	0.9931±0.0067

p_T <20 GeV	All run periods
CMUP	0.937±0.032
CMX	0.914±0.034

Table 7.4
Muon ID scale factors for CDF Monte Carlo events.

7.3 Jets

Quarks and gluons (partons) have a QCD color charge and can participate in strong interactions, which can produce more colored objects with conservation of the total color charge. Thus energetic final state partons can create quark-antiquark pairs from vacuum. This process slows down partons and above some kinematic threshold they can form colorless hadrons with quarks from those $q\bar{q}$ pairs, so called fragmentation or hadronization. In practice hadronization gives us a large number of particles moving in the same general direction, which we call a *jet*.

To find jets we use a standard CDF jet finding algorithm. The cone size R can be equal to 0.4, 0.7 or 1.0, where cone size, effectively the half-angle in azimuthal-pseudorapidity space, is defined as :

$$R = \sqrt{(\Delta\eta)^2 + (\Delta\phi)^2}$$

Several variables are used to identify ans select jets at the CDF detector. These variables are :

- cone size

- the transverse energy

- the pseudorapidity η of the calorimeter cluster of the jet

- the ϕ angle of the calorimeter cluster of the jet

- the fraction of the EM part to the total energy of the jet

In our analysis we use jets with 0.7 cone size. Other standard jet ID cuts are : EM fraction should be between 0.1 and 0.9; and jet should be in the central region ($|\eta| < 2.0$). We use so-called CDF Level 5 Jet Energy Scale (JES) Corrections to calculate E_T of the jet, which should be greater than 15 GeV.

CDF procedure for jet energy correction is described in details in [26]. Level 5 correction includes online/offline calibrations, η dependance, multiple interactions and "Absolute", which corrects the jet energy measured in the calorimeter for any non-linearity and energy loss in the un-instrumented regions of each calorimeter.

If dR between one of the two leptons and the jet is less than 0.4 and this lepton is an electron, the event is removed from the analysis. If this dR is between 0.4 and 0.7 we subtract the energy of the lepton from the energy of the jet and then re-check the jet E_T requirement, ≥ 15 GeV.

7.4 Missing transverse energy

The $\not\!\!E_T$ is defined as the vector sum of the transverse energies deposited in the calorimeter taken with minus sign (opposite direction). Ideally it should be equal to the vector sum of the transverse momenta of the undetected particles. To get closer to the ideal case special corrections must be applied to the various detected particles.

The general prescription for $\not\!\!E_T$ correction is to add to each (x and y) component of the $\not\!\!E_T$ the original E_T minus its corrected E_T . The choice of the objects to correct depends on the analysis objective. In this analysis we are looking for two leptons and one or more jets, so we correct only for the two highest energy leptons and for any jets (with $|\eta| < 2.4$ and $E_{Tj} > 10$ GeV).

First of all, the muon is known to be a Minimum Ionizing Particle (MIP). That means that only a small part (with mean value around 2 GeV) of its energy is deposited in the calorimeters (EM and HAD). On the other hand the muon leaves a good track and its energy can be calculated from momentum. Taking into account this information, the muon corrections to $\not\!\!E_T$ are : add 2 GeV (mean muon calorimeter energy deposition) in the direction of the muon and subtract p_T of the muon calculated from the track information.

The electron's $\not\!\!E_T$ correction comes from the fact that we use beam corrected electron energy in the analysis.

The $\not\!\!E_T$ correction for jets comes from standard CDF jet energy corrections. For this $\not\!\!E_T$ corrections we use all jets with $|\eta| < 2.4$ and $E_{Tj} > 10$ GeV after JES corrections.

8. TRIGGERS

Dilepton triggers were studied by trilepton group in the concept of searches for "exotics" - particles beyond the Standard Model. As a part of the trilepton group Oscar González Lopez (at that time a Purdue Postdoctoral Research Associate) gave several presentations on those studies (see [27]). In parallel, similar studies were done by other members of the trilepton group. All studies have consistent results.

In our analysis we use only central leptons. In this case our choice is limited to CEM electrons, CMUP muons and CMX muons. Since there is no CMX-CMX dilepton SUSY trigger we have 5 possible triggers:

CEM-CEM, CEM-CMUP, CEM-CMX, CMUP-CMUP, CMUP-CMX.

Our chances to get two leptons in the event are not too high, so the p_T threshold of those leptons can be rather low (4 GeV). The corresponding Level 3 (L3) trigger names for those triggers are : DIELECTRON_CENTRAL_4, CEM4_CMUP4, CEM4_CMX4, DIMUON_CMUPCMUP4, DIMUON_CMUP4_CMX4. In some time periods CMUP triggers were replaced by CMU triggers. In this case instead above CMUP triggers we used : CEM4_CMU4, DIMUON_CMUCMU4 and DIMUON_CMU4_CMX4. For all muon triggers, in this analysis we required either CMUP or CMX reconstructed muons (even if the CMU triggers were used).

Instead of treating all triggers differently it is useful to disassemble trigger into parts corresponding to just one lepton("legs"), and treat each of the two legs individually before recombining the efficiencies. For each data event we check that the trigger, corresponding to the two highest p_T leptons used in the analysis, is fired and that each trigger track is within a 0.4 cone of the corresponding lepton object.

Total trigger efficiency is calculated as the product of trigger efficiencies of two leptons. This approach is valid since we first check for the two highest p_T leptons and then check the trigger, so that for each event only one trigger is used.

Electron leg

As discussed earlier, all dilepton triggers were divided into constituent parts ("legs"). A given type of legs behaves similarly in all triggers that include them. There is a clear dependence of the trigger efficiency on lepton energy. Plateau efficiency of the CEM electron leg is eTrEff=0.963 ±0.003 (see [21] as well as [27]). The turn-on curve is rather broad and is defined by the following formula eTrEff/(1+exp((3.964-E_T)/1.622) for low energy electrons (E_T <10 GeV).

Muon leg

From Oscar González's studies [27] we have values of the muon trigger efficiencies. CMX muon trigger leg efficiency is found to be equal to $0.910 \pm .007$ for all triggers with CMX muon. The CMUP trigger leg efficiency shows little dependance with respect to the nature of the other leg of the trigger. It's equal to $0.911 \pm .007$ if the other leg is a CEM electron and it's equal to $0.925 \pm .009$ if the other leg is (any) muon type. For muons we use plateau values of the efficiency only, since these plateaus extend down to $p_T \approx 6$ GeV/c.

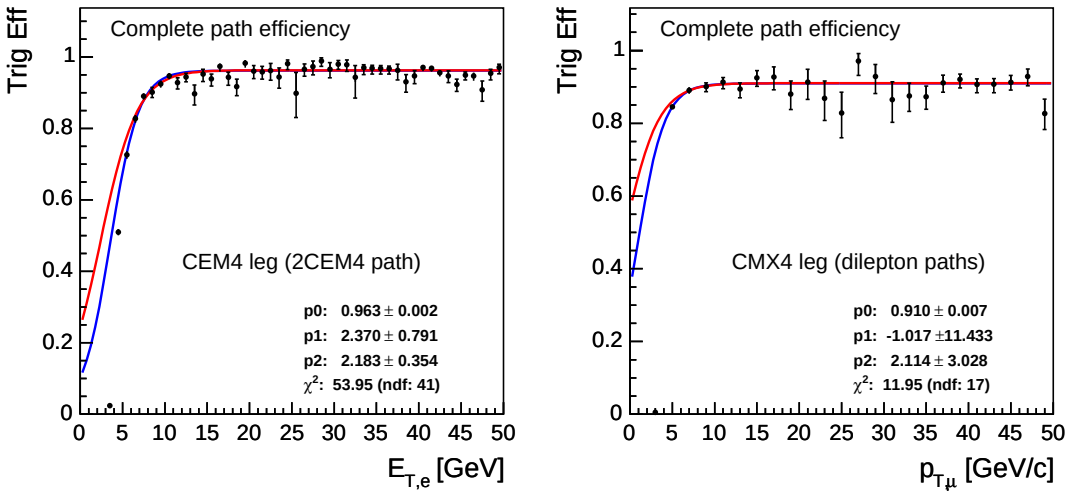

Figure 8.1. Trigger efficency plots from [27] for CEM4 and CMX4.

Two fit intervals were used for comparison (red and blue fits).

9. SYSTEMATIC UNCERTAINTIES

Systematic errors are calculated as the mean of $+1\sigma$ (up) fluctuation and -1σ (down) fluctuation from the central value.

The total systematic error is calculated by adding uncorrelated uncertainties in quadrature and correlated uncertainties linearly. Those sources are different for signal and for backgrounds. Prescriptions for the calculations of different systematic errors can be found on the CDF Joint Physics web page (and/or trilepton group web page).

Systematic errors on Background

The systematic uncertainty on lepton+fakes is taken to be 50% . For the other backgrounds it comes from different sources.

Sources of the systematic uncertainties on Background estimations are :

- the luminosity uncertainty is equal to 6% and it's applied to all MC estimations, (not applied to HF estimation from data).
- the Dilepton triggers uncertainty is equal to 2%;
- the lepton ID uncertainty is equal to 2%;
- the jet energy scale uncertainty (which is rather big for DY, since our CR are defined by presence of jet - see Table 9.1),
- PDFs (Parton Distribution Function) is $\approx 2\%$,
- ISR/FSR (Initial/Final State Radiation) (estimated from $t\bar{t}$ MC sample, $ee = 3.6\%$, $e\mu = 2.2\%$, $\mu\mu = 4.4\%$)
- uncertainties on theoretical calculations of the cross sections are the following : $t\bar{t}$= 8% , DY = 2% , WW = 6% , WZ = 8% , ZZ = 10% , Wγ = 7% [28].

	DY	$t\bar{t}$	WW	WZ	ZZ	Wγ	$\tilde{t}\bar{\tilde{t}}$
X-section	2%	8%	6%	8%	10%	7%	-
Lumi	6%	6%	6%	6%	6%	6%	6%
JES	35%	0.3%	11%	11%	11%	11%	1-11
Trigger Eff.	2%	2%	2%	2%	2%	2%	2%
lepton ID	2%	2%	2%	2%	2%	2%	2%
PDF	2%	2%	2%	2%	2%	2%	2%
isr/fsr	3%	3%	3%	3%	3%	3%	3%

Table 9.1
Systematic errors

For most of the systematic uncertainties we fluctuate the source value of the uncertainty (like using different MC sample for ISR, or apply different value for jet energy scale) and then look at the change in the number of events in the region of interest.

Systematic errors on signal (stop)

Sources of the systematic uncertainties on the MC stop signal estimations and Background estimations are almost the same.

Values of the jet energy scale uncertainty vary from 1% to 11% depending on stop sneutrino mass difference. ISR/FSR uncertinty was estimated from the 150/75 (stop/sneutrino masses) MC sample and is equal to ee = 2.8% , $e\mu$ = 2.3% , $\mu\mu$ = 3.9%. Table 9.1 represents quick summary of the mean values of all systematic uncertainties.

No systematic errors on MC generated stop sample Xsection (≈20%) were used in the tables, since our experimental upper limits are to be compared to the central values of the theoretical stop pair production cross section.

10. PRESELECTION AND CONTROL REGIONS

As preselection cuts we require two highest p_T leptons in the event to satisfy the following criteria :

- p_T of the first lepton $p_{T1} \geq 10$ GeV;
- p_T of the second lepton $p_{T2} \geq 5$ GeV;
- dR between those leptons ≥ 0.4 ;
- both leptons pass ID cuts (e or μ);
- only one of the leptons may be CMX muon;
- invariant mass of the two leptons ≥ 15 GeV;
- at most one of the leptons may be CMX muon.

The invariant mass cut helps to remove contributions from low invariant mass resonances.

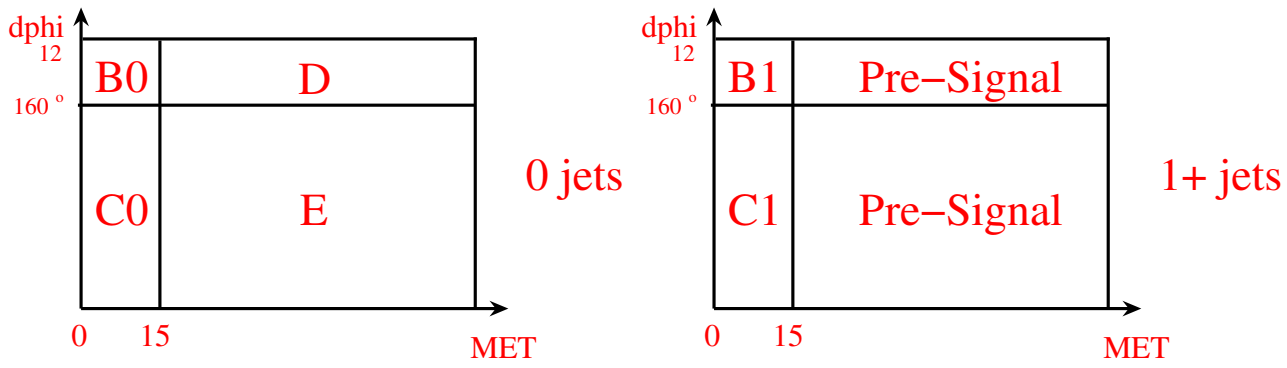

Figure 10.1. Definitions of Control Regions (y axis - $\Delta\phi$ between leptons).

One of the useful checks of our understanding of the Standard Model backgrounds is comparing the expected and observed numbers of events for cases where the stop contribution is expected to be small. For this purpose we define several Control Regions (CR).

The first Control Region (Control Region A) is for ee and $\mu\mu$ events with dilepton mass in Z mass window (76,106) GeV (no further cuts required). Those events are removed from all other regions.

The stop signature requires $\not\!\!E_T$ and one or more jets, so we can use events with low $\not\!\!E_T$ or/and without jets as additional Control Regions. For better understanding we divided the events using the difference in ϕ between the two leptons. We choose back-to-back Control Regions for $\Delta\phi$ between 160° and 180°, and not-back-to-back for $\Delta\phi$ between 0° and 160°.

Since the $\not\!\!E_T$ calculation is vital for our Control Regions (except CR A) and our pre-signal region, we introduce further preselection clean up cuts at this stage. We require the electron direction to be not too close to the azimuthal boundary of the calorimeter wedges (half a degree from each boundary; the wedges are 15° wide in ϕ).

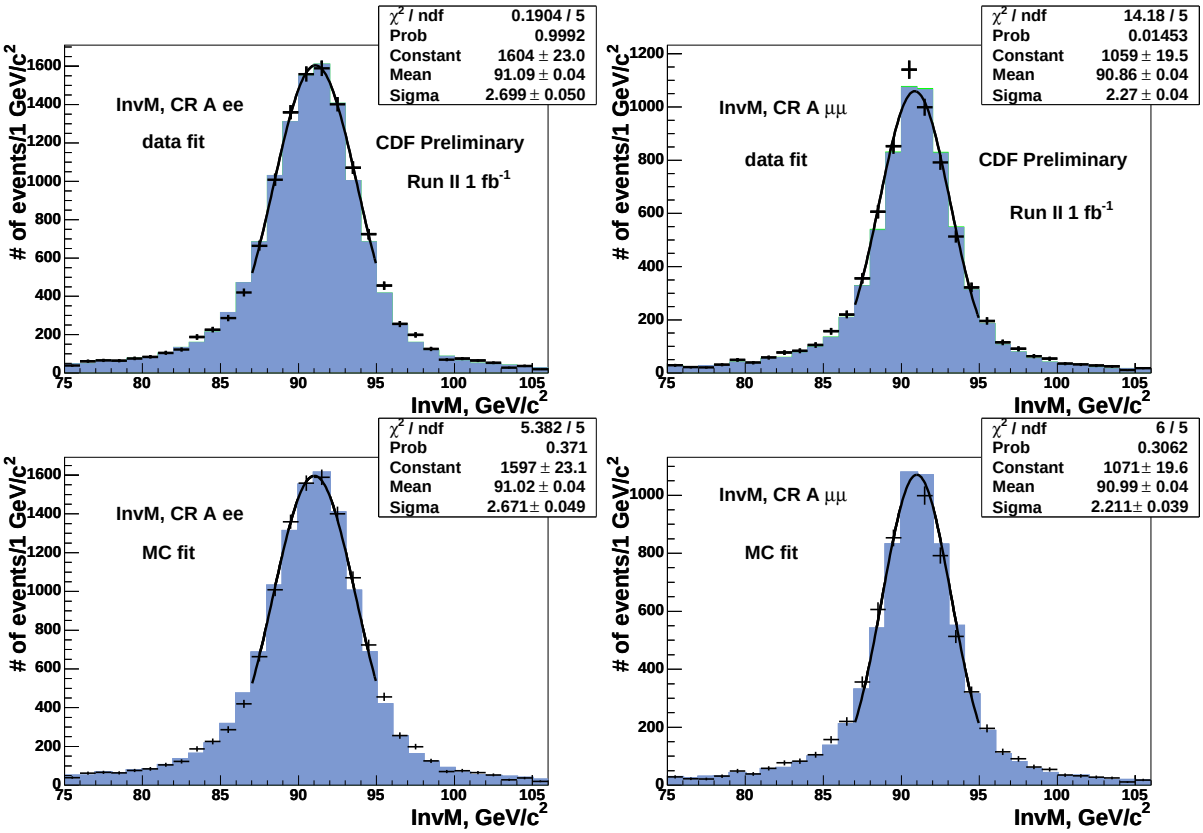

Figure 10.2. Z peak invariant mass plots with data fits (top) and MC fits (bottom).

10.1 Control Region A (Z peak).

Most of the ee and $\mu\mu$ events with dilepton invariant mass between 76 GeV and 106 GeV come from direct production via real or virtual photon (γ) or Z boson, the Drell-Yan (DY) process.

The DY totals are in excellent agreement with data. Other expected SM backgrounds ($t\bar{t}$, lepton + fakes and dibosons) are negligible in this region, see Table 10.1.

Experimental mass resolution is significant relative to the Breit Wigner (BW) $\Gamma_Z = 2.5$ GeV/c^2. We restrict the Gaussian fit to the mass range 87-95 GeV/c^2 to avoid the significant tails of the BW. Data and MC masses agree much better than the eye perceives, given how well the MC fitted curve follows the data points. Very

	ee	$\mu\mu$
DY	12313.56±63.19±956.20	6904.46±43.06±568.46
$t\bar{t}$	1.92±0.06±0.21	1.18±0.04±0.13
diboson	16.25±0.04±1.16	10.43±0.03±0.77
e+fake	2.90±0.03±1.45	0.00±0.00±0.00
μ+fake	0.00±0.00±0.00	30.01±0.63±15.01
Exp.	12334.64±63.19±956.20	6946.08±43.06±568.65
Obs.	12461	7111

Table 10.1
Control Region A (Z peak).

slight systematic shifts in the Z mass are expected to have completely negligible effect on the present stop search.

10.2 Control Regions with low $\not\!\!E_T$ and no jets.

Two control regions are characterized by low $\not\!\!E_T$ and no jets : B0 and C0. CR B0 is for back to back leptons and CR C0 is for the rest.

The major contribution in the ee and $\mu\mu$ channels comes from DY, whereas in the $e\mu$ channel Heavy Flavor production is the major contribution, see Table 10.2 and Table 10.3. The $\not\!\!E_T$, H_T , p_{T1} and p_{T2} distributions for CRs B0 and C0 are shown in Figures 10.3, 10.4, 10.5, 10.6.

	ee	$e\mu$	$\mu\mu$
DY	4207.21±35.98±396.82	187.53±7.28±18.18	2797.16±27.07±293.23
$t\bar{t}$	0.00±0.00±0.00	0.01±0.00±0.00	0.00±0.00±0.00
diboson	0.84±0.01±0.08	1.28±0.02±0.13	0.49±0.01±0.05
e+fake	107.72±0.27±53.86	49.66±0.58±24.83	0.00±0.00±0.00
μ+fake	0.00±0.00±0.00	43.91±0.16±21.96	21.44±0.34±10.72
HF	505.08±55.89±82.23	611.87±46.50±52.67	293.33±41.66±31.51
Exp.	4820.84±66.47±408.81	894.26±47.07±64.84	3112.42±49.68±295.12
Obs.	4922	1024	3311

Table 10.2
Control Region B0. $\not\!\!E_T \geq 15$ GeV, no jets, back-to-back leptons.

	ee	$e\mu$	$\mu\mu$
DY	2046.97±24.07±253.38	10.38±1.67±2.66	1883.89±22.17±235.93
$t\bar{t}$	0.00±0.00±0.00	0.00±0.00±0.00	0.00±0.00±0.00
diboson	0.56±0.01±0.04	0.64±0.01±0.06	0.32±0.01±0.03
e+fake	155.69±0.34±77.85	42.77±0.54±21.39	0.02±0.01±0.01
μ+fake	0.01±0.00±0.01	60.93±0.19±30.47	18.35±0.31±9.18
HF	320.87±38.03±57.82	489.83±39.88±57.69	260.74±37.87±34.53
Exp.	2524.11±45.01±271.30	604.55±39.92±68.71	2163.33±43.88±238.62
Obs.	2526	663	2033

Table 10.3
Control Region C0. $\not\!\!E_T \geq 15$ GeV, no jets, not back-to-back leptons.

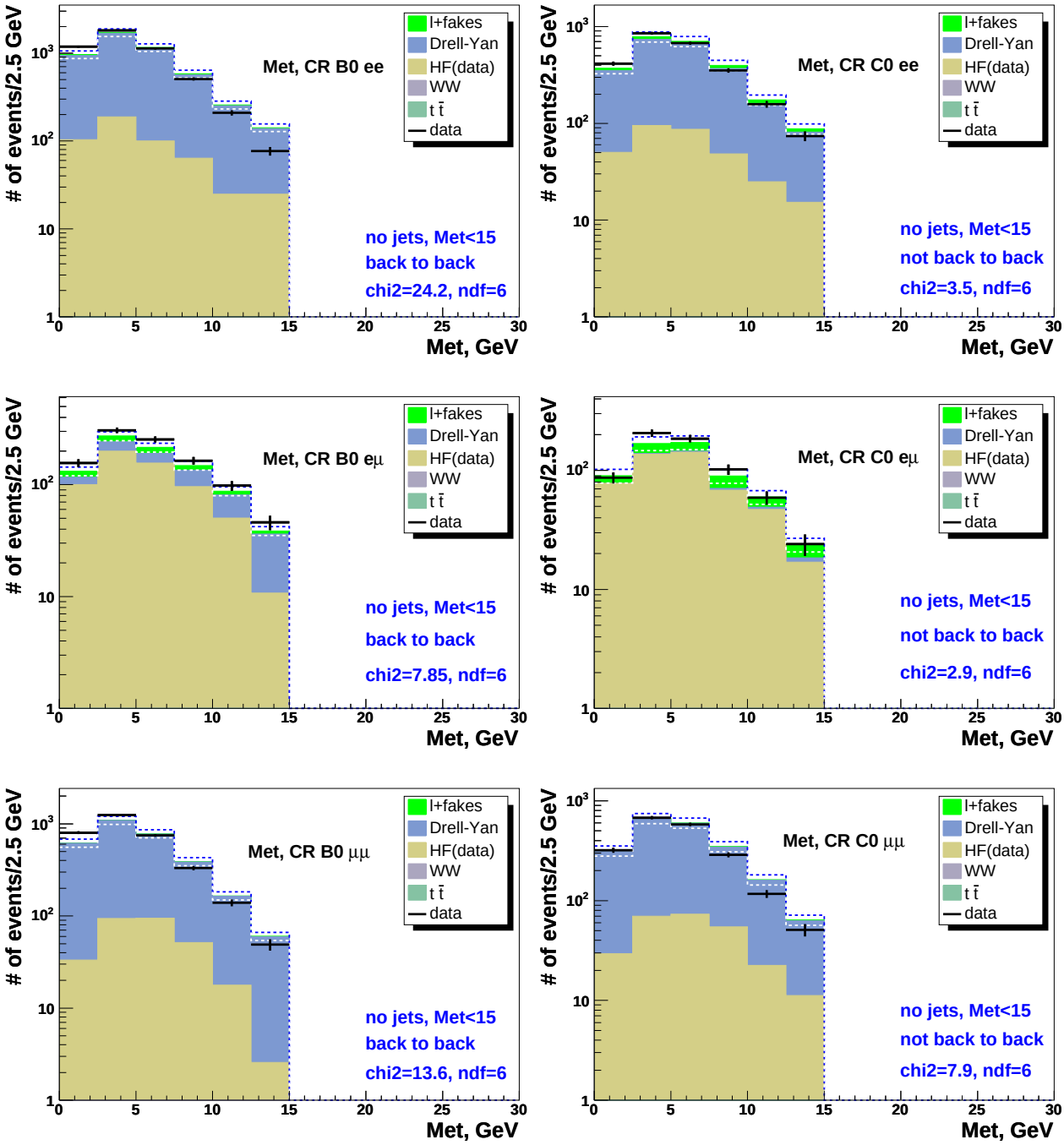

Figure 10.3. $\not\!\!E_T$ plots for CR with low $\not\!\!E_T$ and no jets (B0 and C0).

The dotted lines represent $\pm\sigma$ uncertainties on the summed backgrounds.

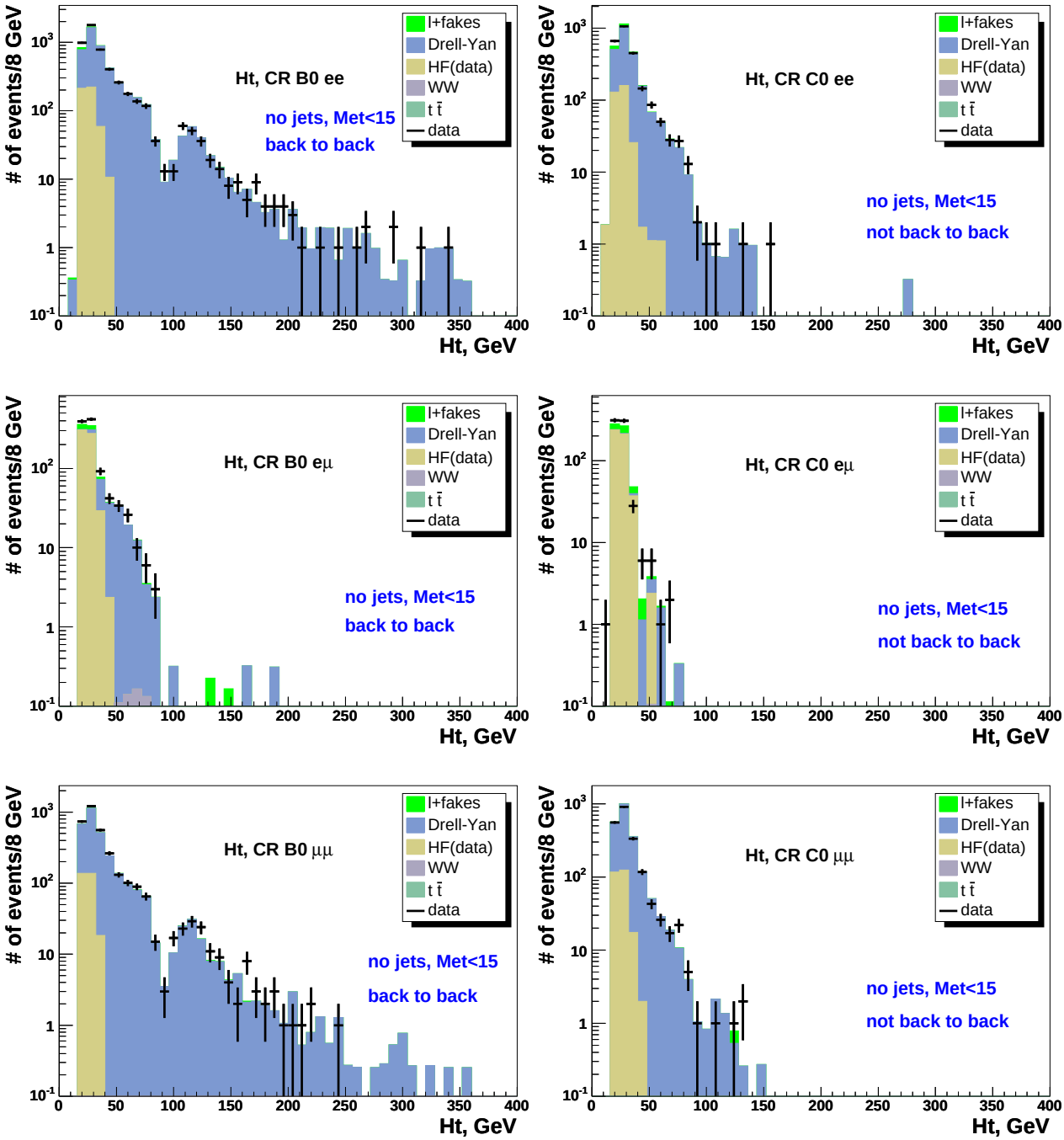

Figure 10.4. H_T plots for CR with low $\not\!\!E_T$ and no jets (B0 and C0).

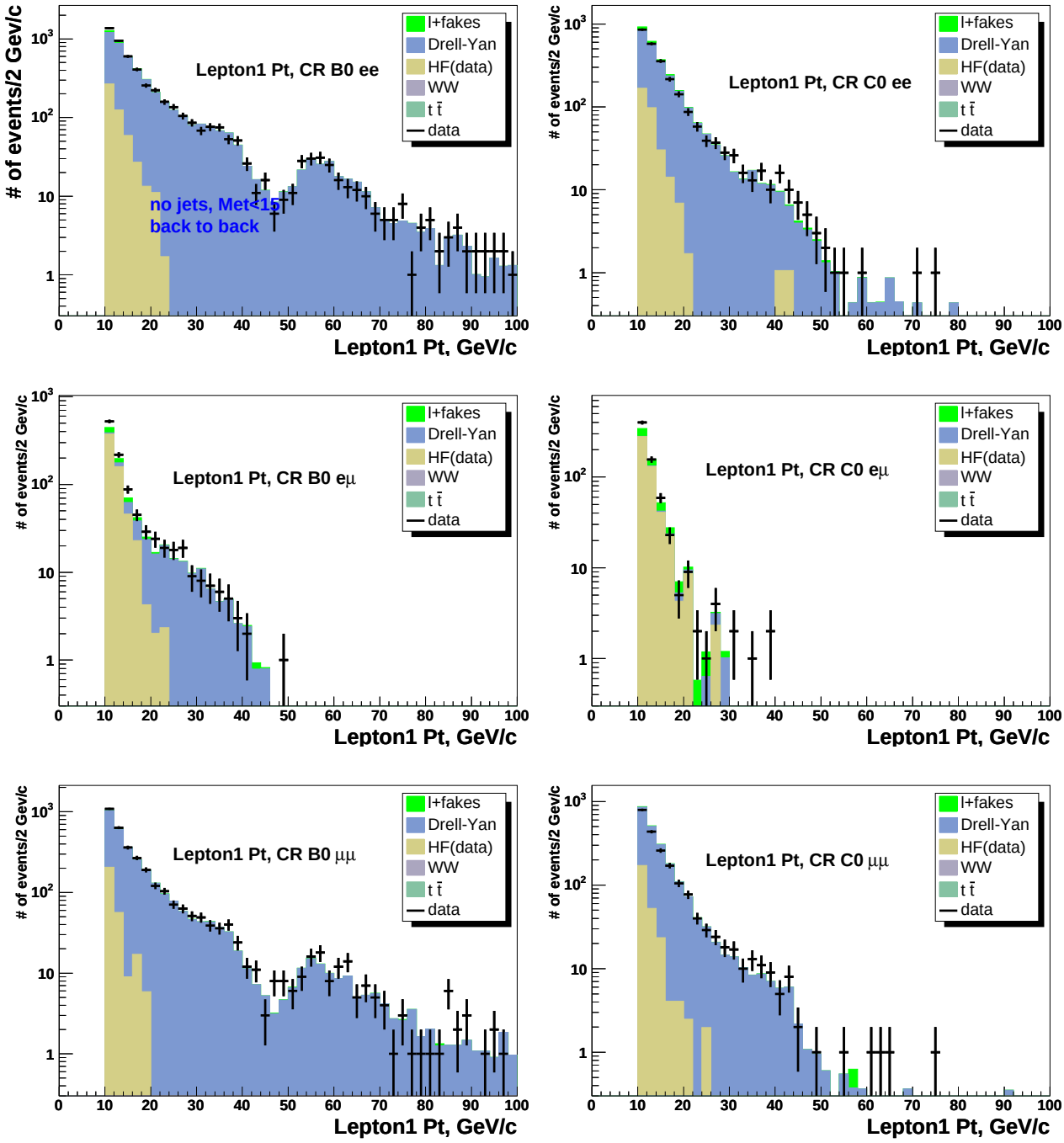

Figure 10.5. p_{T1} plots for CR with low $\not\!\!E_T$ and no jets (B0 and C0).

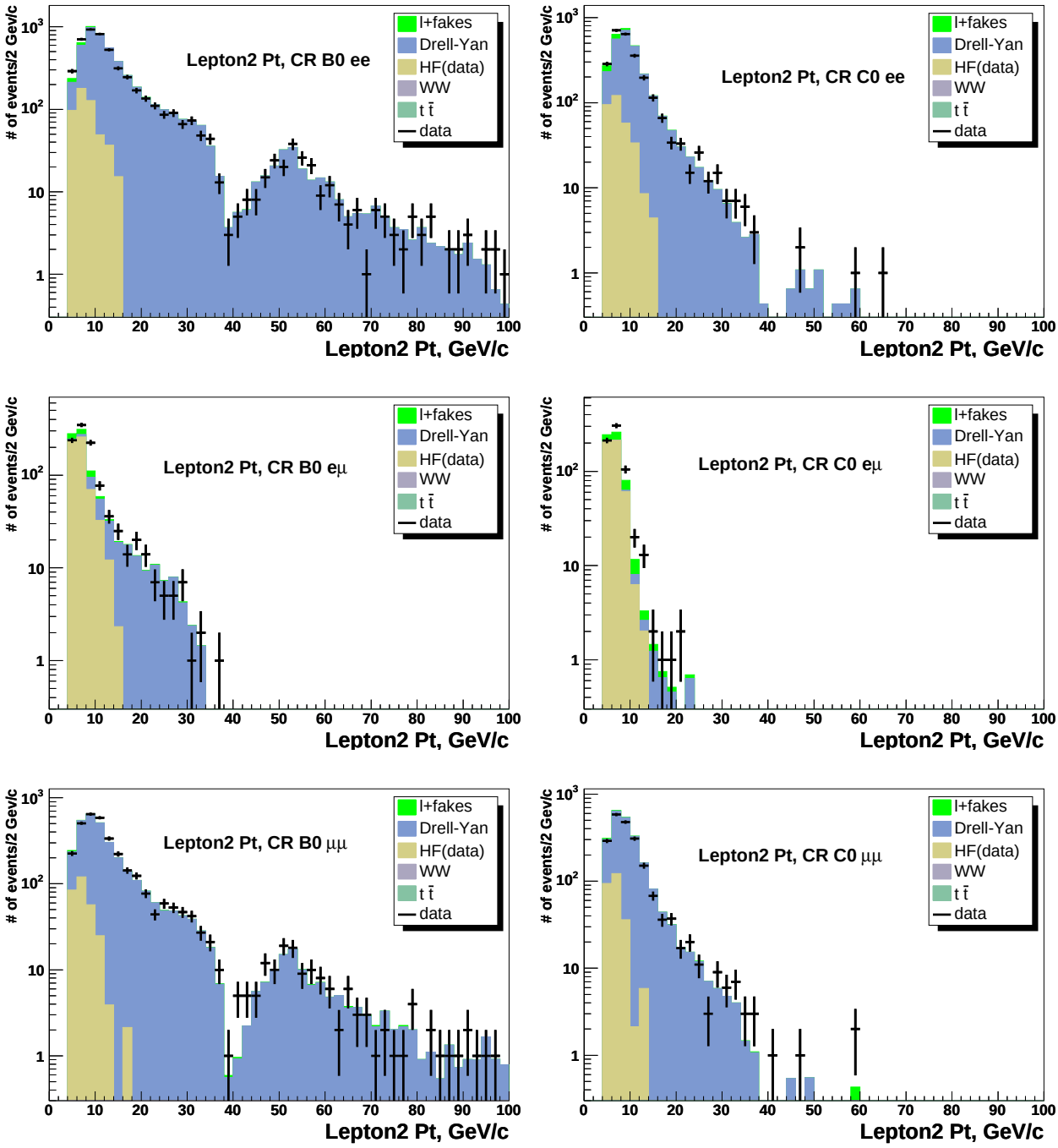

Figure 10.6. p_{T2} plots for CR with low $\not\!\!E_T$ and no jets (B0 and C0).

10.3 Control Regions with high $\not\!\!E_T$ and no jets.

Two control regions are characterized by high $\not\!\!E_T$ and no jets : D and E. CR D is for back to back leptons and CR E is for the rest.

The major contribution in the ee and $\mu\mu$ chanels comes from DY, whereas in the $e\mu$ channel Heavy Flavor production is the major contribution, see Table 10.4 and Table 10.5. The $\not\!\!E_T$, H_T , p_{T1} and p_{T2} distributions for CRs D and E are shown in Figures 10.7, 10.8, 10.9, 10.10

10.4 Control Regions with low $\not\!\!E_T$ and at least one jet.

Two control regions are characterized by low $\not\!\!E_T$ and at least one jet : B1 and C1. CR B1 is for back to back leptons and CR C1 is for the rest.

The major contribution in the ee and $\mu\mu$ chanels comes from DY, whereas in the $e\mu$ channel Heavy Flavor production is the major contribution, see Table 10.6 and Table 10.7. The $\not\!\!E_T$, H_T , p_{T1} and p_{T2} distributions for CRs B1 and C1 are shown in Figures 10.11, 10.12, 10.13, 10.14.

	ee	$e\mu$	$\mu\mu$
DY	124.17±6.16±19.34	85.08±4.83±6.44	67.47±4.24±13.19
$t\bar{t}$	0.04±0.01±0.01	0.03±0.01±0.00	0.00±0.00±0.00
dibson	1.42±0.02±0.13	2.22±0.02±0.20	0.80±0.01±0.08
e+fake	2.79±0.05±1.39	2.04±0.11±1.02	0.00±0.00±0.00
μ+fake	0.00±0.00±0.00	1.92±0.03±0.96	1.08±0.08±0.54
HF	11.61±4.58±6.01	31.40±8.30±2.62	6.69±3.98±2.30
Exp.	140.03±7.68±20.30	122.69±9.61±7.09	76.05±5.82±13.40
Obs.	114	107	57

Table 10.4
Control Region D. $\not\!\!E_T \geq 15$ GeV, no jets, back-to-back leptons.

	ee	$e\mu$	$\mu\mu$
DY	42.96±3.57±6.54	8.51±1.46±1.02	41.02±3.29±6.35
$t\bar{t}$	0.09±0.01±0.01	0.12±0.01±0.02	0.04±0.01±0.01
diboson	7.92±0.04±0.75	12.66±0.05±1.19	5.09±0.03±0.51
e+fake	20.27±0.13±10.14	5.11±0.19±2.56	0.00±0.00±0.00
μ+fake	0.00±0.00±0.00	12.89±0.09±6.44	3.64±0.15±1.82
HF	3.97±2.46±3.66	31.17±8.21±3.35	19.46±6.93±4.36
Exp.	75.21±4.33±12.63	70.46±8.34±7.86	69.24±7.67±7.93
Obs.	72	53	57

Table 10.5
Control Region E. $\not\!\!E_T \geq 15$ GeV, no jets, not back-to-back leptons.

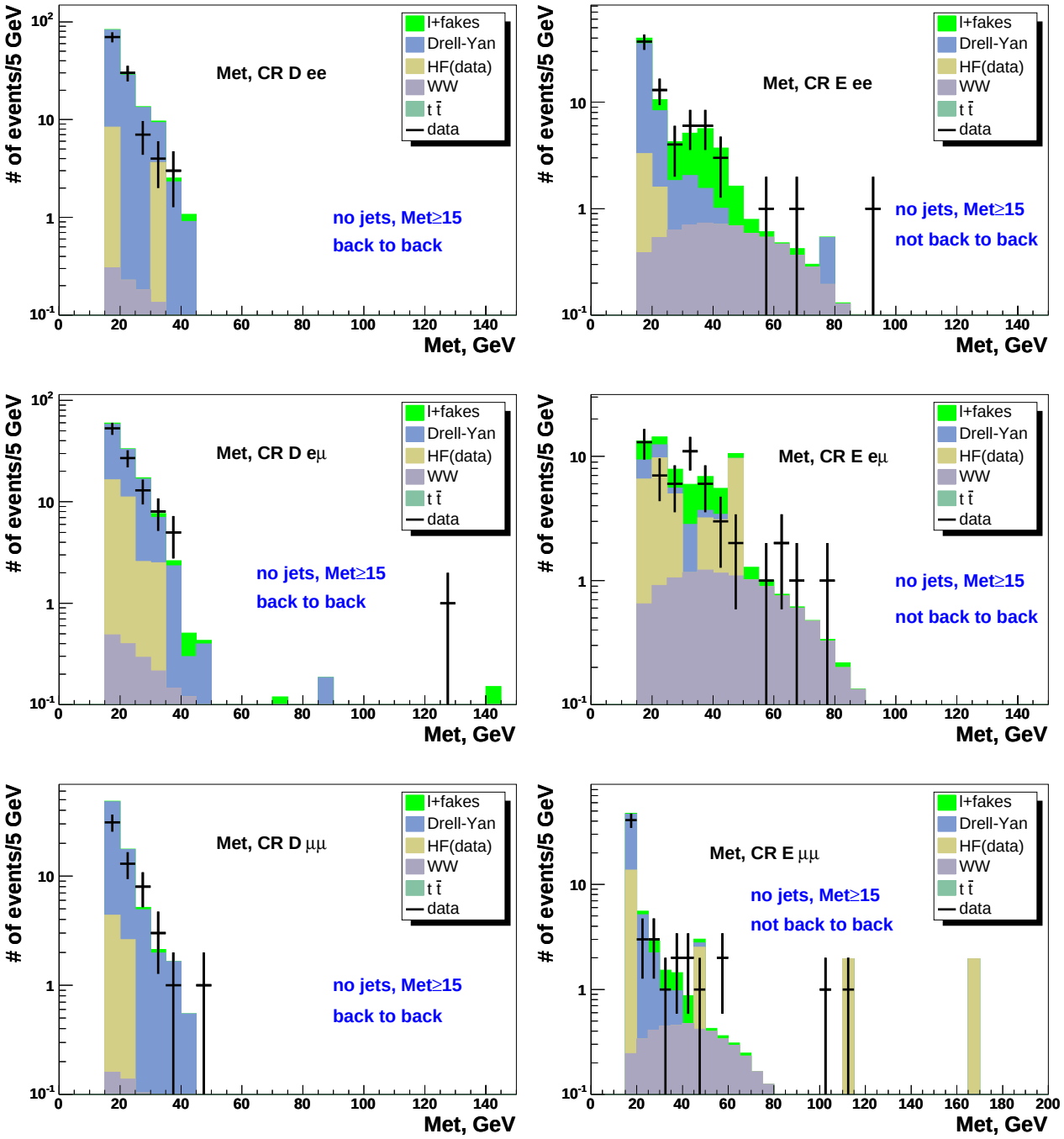

Figure 10.7. $\not\!\!E_T$ plots for CR with high $\not\!\!E_T$ and no jets (D and E).

The dotted lines represent $\pm\sigma$ uncertainties on the summed backgrounds.

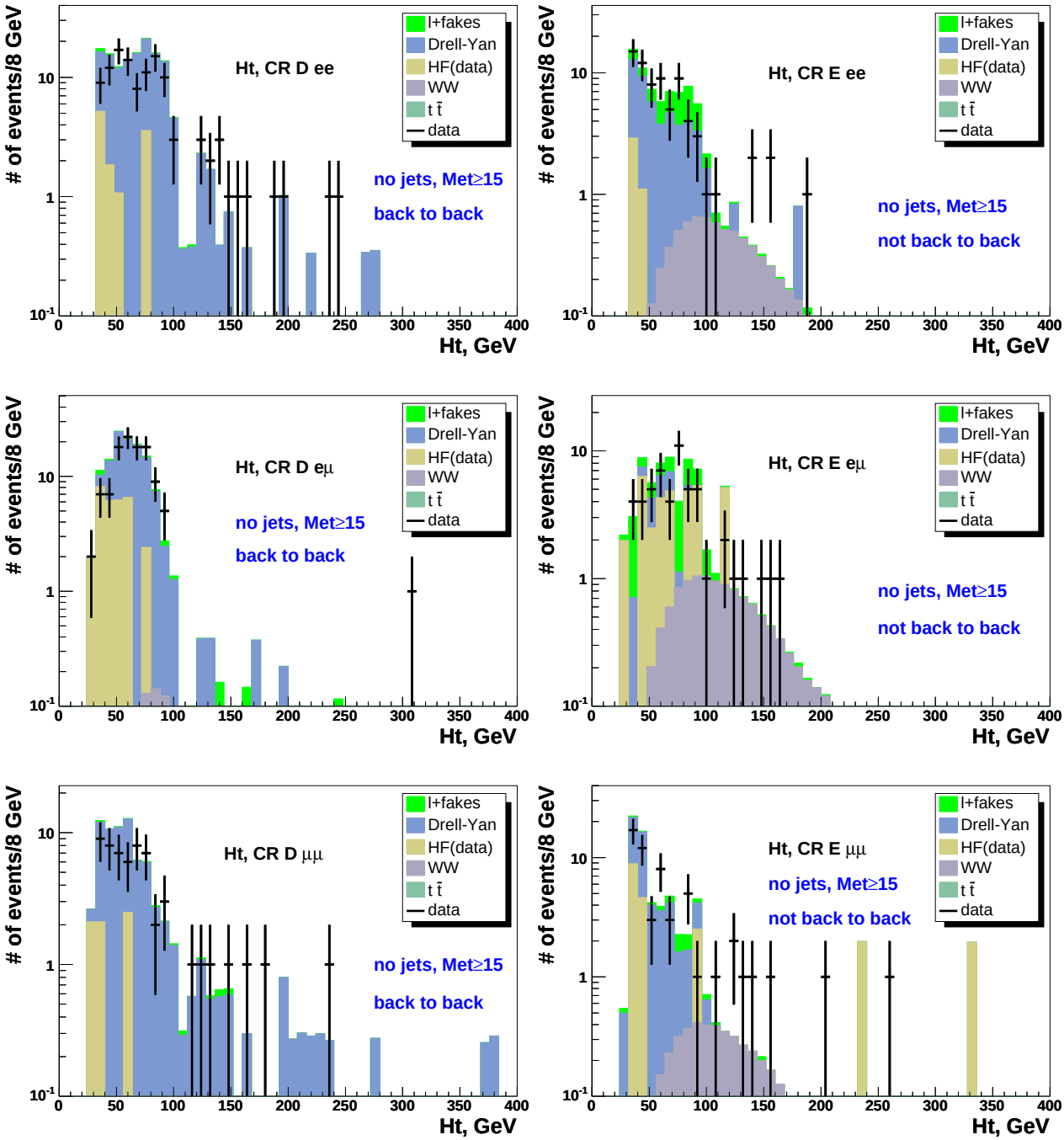

Figure 10.8. H_T plots for CR with high $\not{E}_T$ and no jets (D and E).

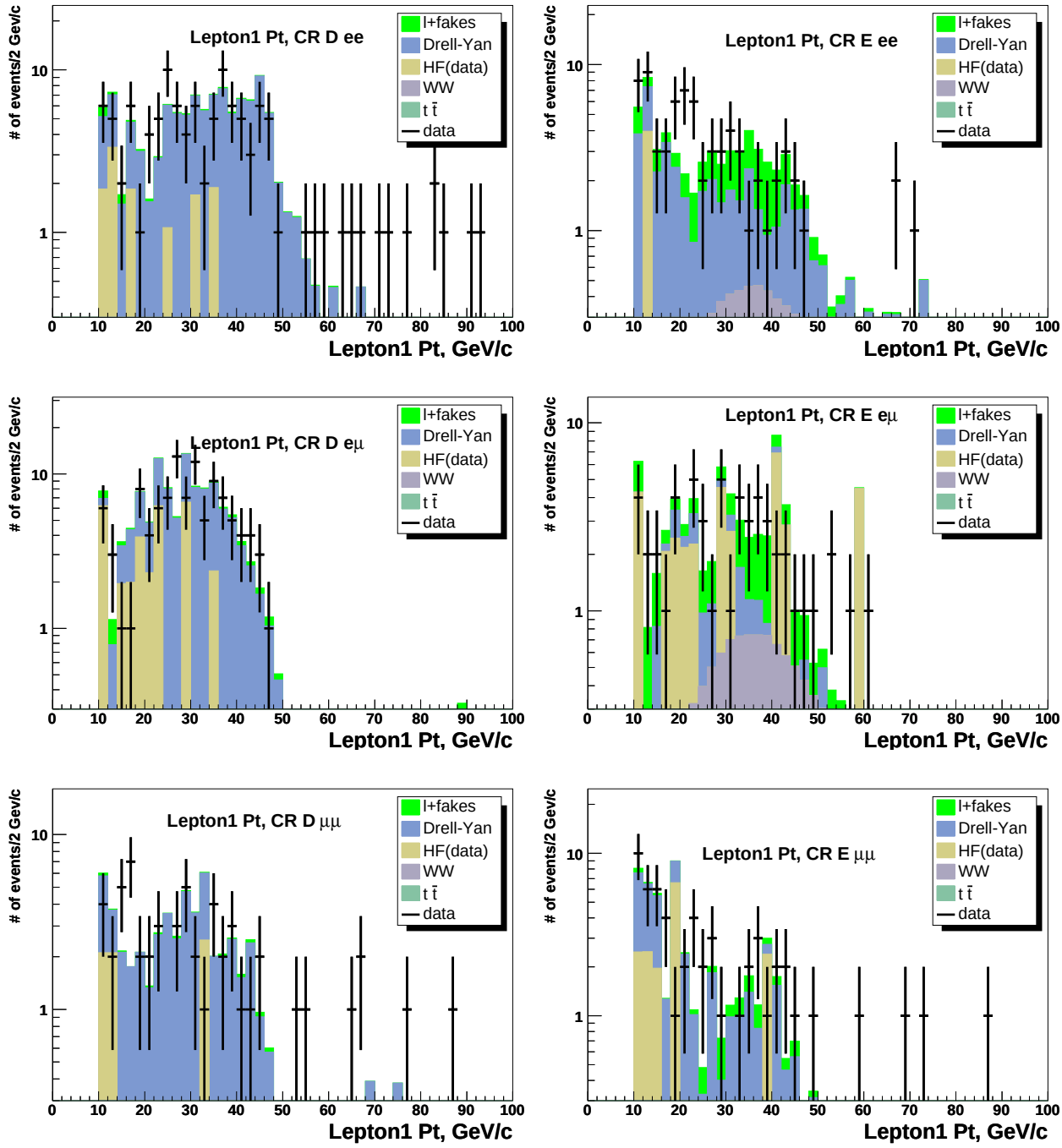

Figure 10.9. p_{T1} plots for CR with high $\not{E}_T$ and no jets (D and E).

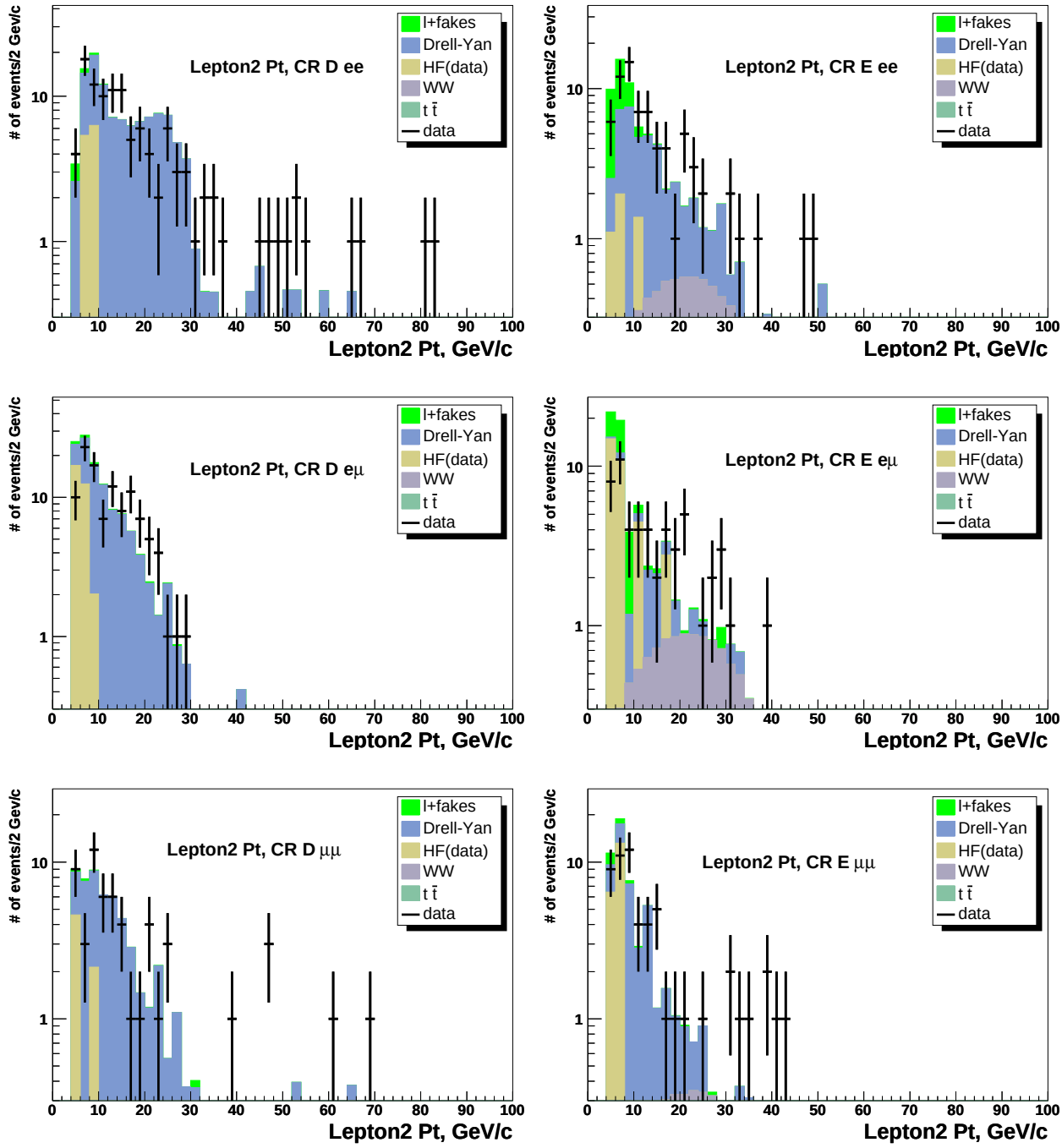

Figure 10.10. p_{T2} plots for CR with high $\not\!\!E_T$ and no jets (D and E).

	ee	$e\mu$	$\mu\mu$
DY	321.05±9.93±93.63	25.58±2.68±5.79	305.70±8.97±79.97
$t\bar{t}$	0.07±0.01±0.01	0.13±0.01±0.02	0.04±0.01±0.00
diboson	0.29±0.01±0.02	0.21±0.01±0.03	0.21±0.00±0.02
e+fake	81.64±0.18±40.82	27.66±0.43±13.83	0.00±0.00±0.00
μ+fake	0.00±0.00±0.00	36.95±0.11±18.48	12.02±0.25±6.01
HF	38.19±8.72±9.09	88.12±14.34±30.59	54.21±12.50±23.82
Exp.	441.24±13.22±102.55	178.66±14.59±38.75	372.18±15.39±83.66
Obs.	322	127	321

Table 10.6
Control Region B1. $\not\!\!E_T$<15 GeV, $\geq$ 1 jet, back-to-back leptons.

	ee	$e\mu$	$\mu\mu$
DY	839.58±15.79±132.58	16.30±2.14±1.37	698.73±13.55±124.88
$t\bar{t}$	0.23±0.02±0.03	0.44±0.03±0.05	0.17±0.01±0.02
diboson	1.08±0.01±0.09	0.37±0.01±0.04	0.77±0.01±0.07
e+fake	133.15±0.25±66.58	33.80±0.47±16.90	0.00±0.00±0.00
μ+fake	0.00±0.00±0.00	56.75±0.15±28.38	15.59±0.30±7.79
HF	105.36±16.57±23.09	158.59±19.83±39.43	116.20±20.71±21.74
Exp.	1079.40±22.89±150.14	266.25±19.95±51.45	831.45±24.75±127.00
Obs.	1121	224	925

Table 10.7
Control Region C1. $\not\!\!E_T$<15 GeV, $\geq$ 1 jet, not back-to-back leptons.

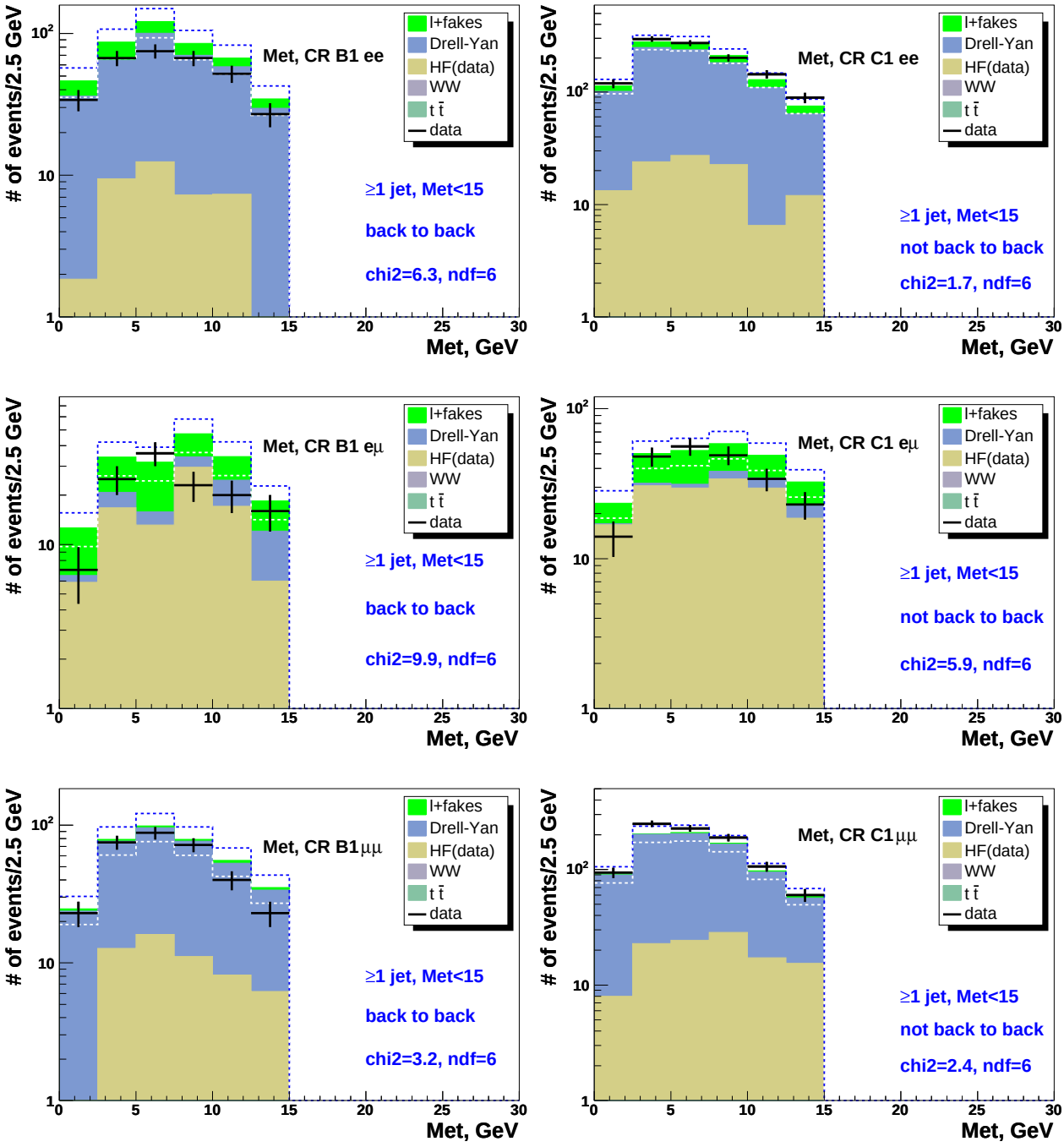

Figure 10.11. $\not\!\!E_T$ plots for CR with low $\not\!\!E_T$ and at least one jet (B1 and C1).

The dotted lines represent $\pm\sigma$ uncertainties on the summed backgrounds.

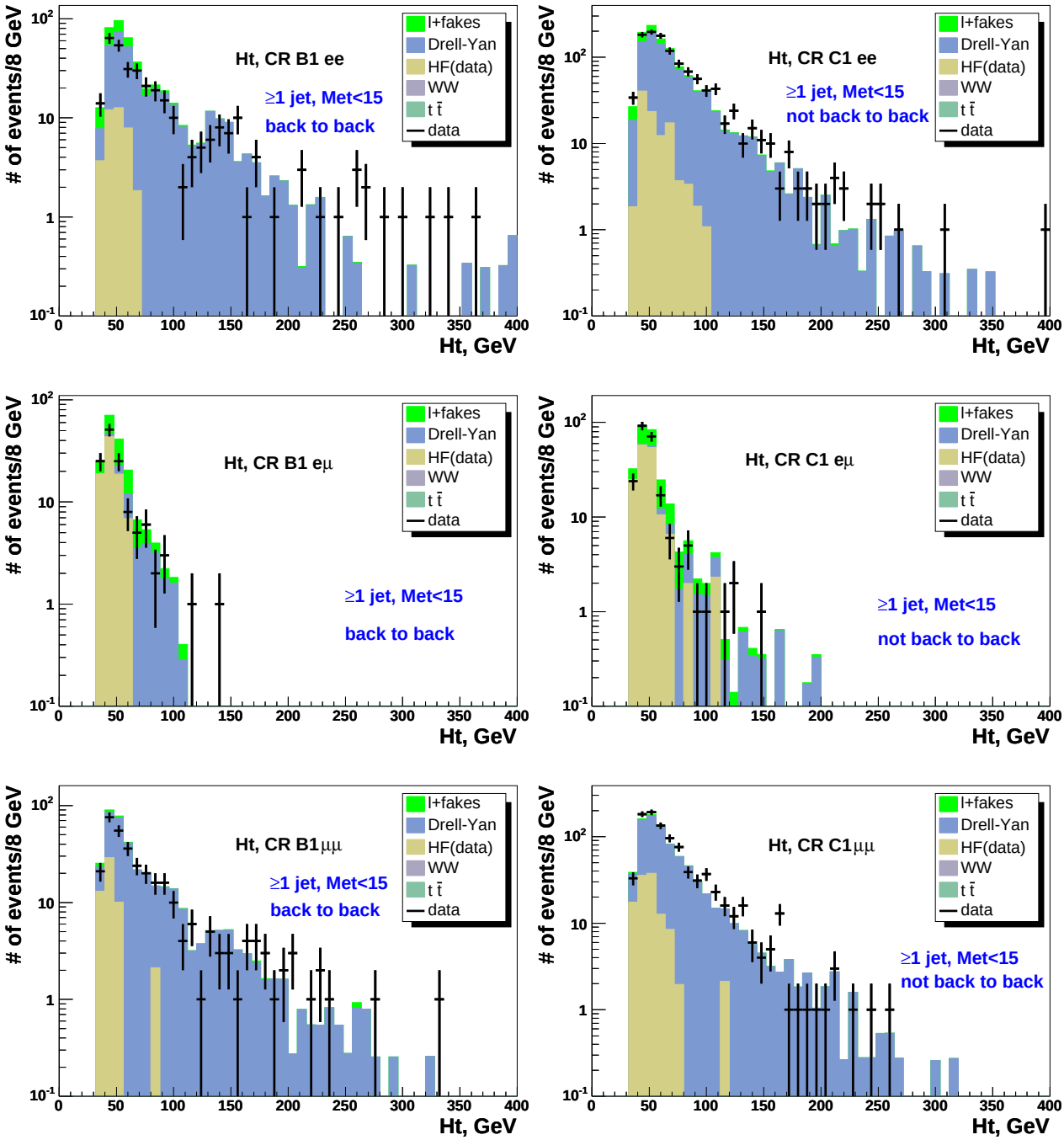

Figure 10.12. H_T plots for CR with low $\not\!\!E_T$ and at least one jet (B1 and C1).

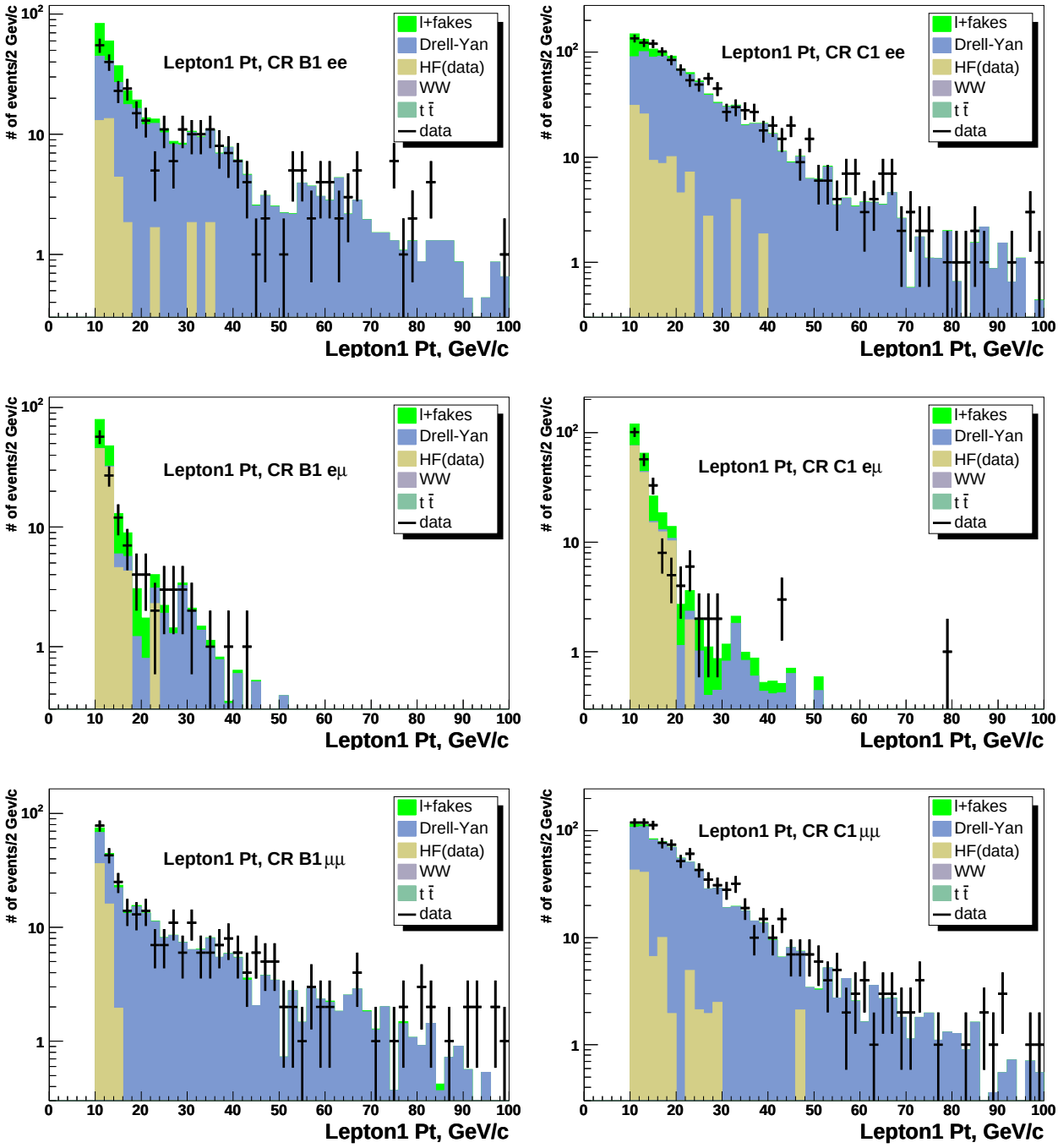

Figure 10.13. p_{T1} plots for CR with low $\not\!\!E_T$ and ≥ 1 jet (B1 and C1).

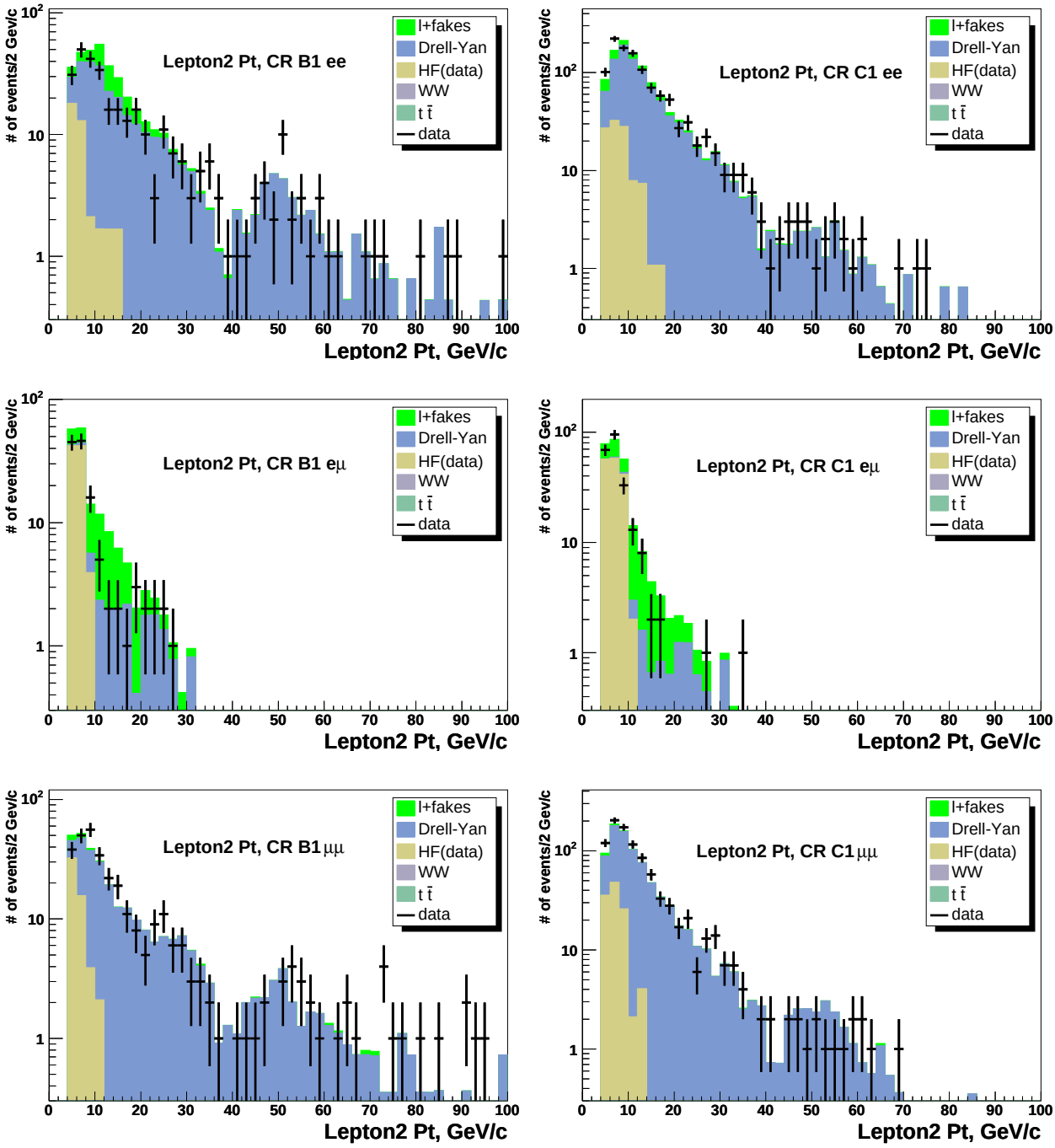

Figure 10.14. p_{T2} plots for CR with low $\not\!\!E_T$ and ≥ 1 jet (B1 and C1).

10.5 Extra clean up cut for pre-signal region

Our pre-signal region is characterized by high $\not\!\!E_T$ ($\geq$ 15 GeV) and at least one jet (with $E_{Tj} \geq 15$ GeV). Contributions to this region from different Standard Model processes are shown in Table 10.8.

To remove events which are particularly likely to have mismeasured $\not\!\!E_T$, a number of CDF analyses remove events with the $\not\!\!E_T$ close to objects such as leptons or jets. We define a variable dPhiMet_min to be the smallest of the azimuthal angle differences between $\not\!\!E_T$ and either lepton1, lepton2 or the leading jet (with E_{Tj} >15 GeV), if any. Fig. 10.15 shows a clear excess of dimuon events over the modeled background, for dPhiMet_min $< 20^\circ$ in the Z region (CR A). Fig. 10.15 also shows un-modeled excesses at low dPhiMet_min in ee and $\mu\mu$ events in CR C1 ($\not\!\!E_T$ <15 GeV, 1 or more jets, leptons not back-to-back).

Table 10.9 summarizes the pre-signal sample after the extra ("final") cleanup cut. A substantial number of Drell Yan background events (ee and $\mu\mu$), in which very little genuine $\not\!\!E_T$ is expected, are removed from the pre-signal sample by this cut. We take this to be yet another validation of the cut.

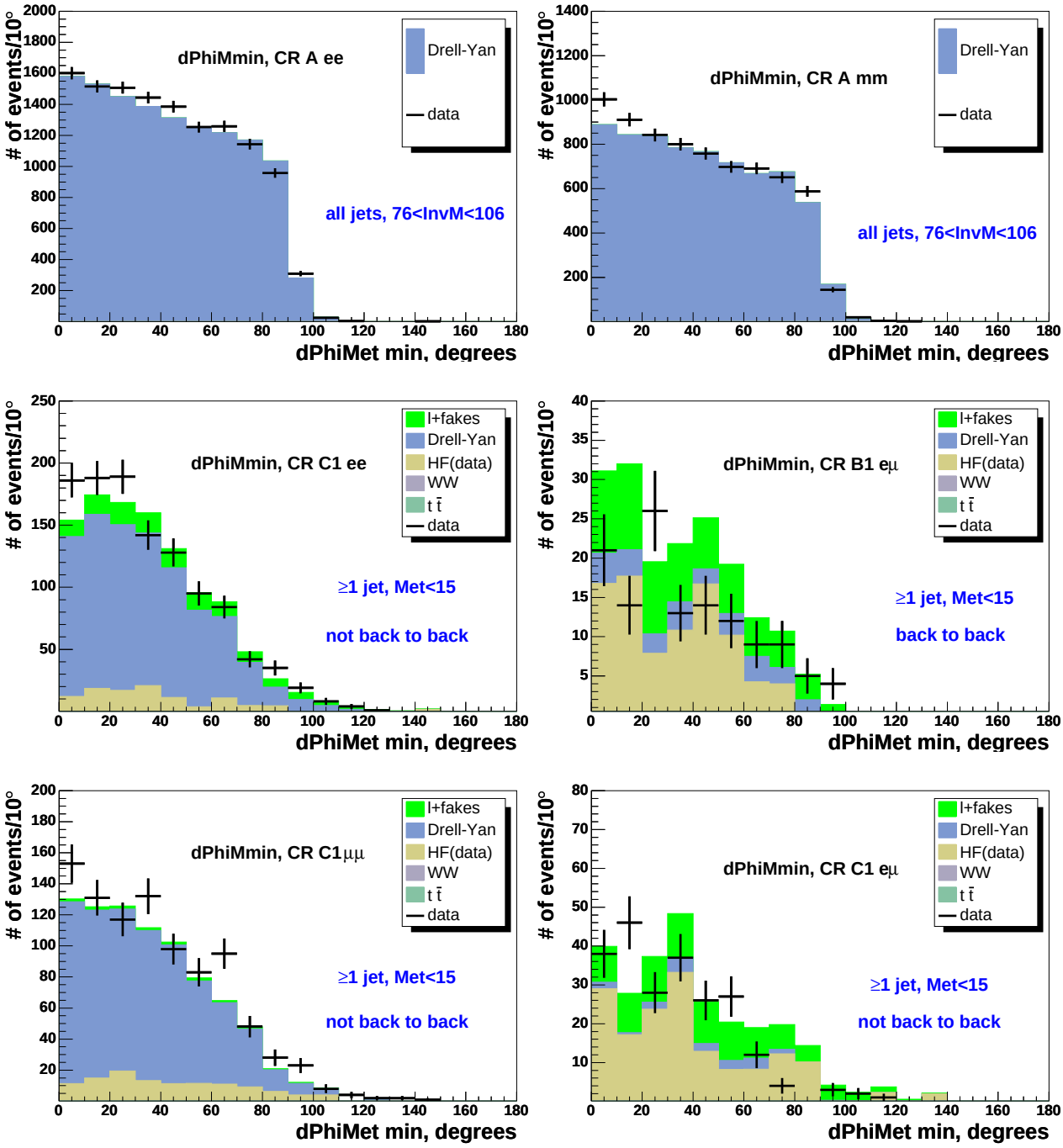

Figure 10.15. Smallest dPhi between $\not\!\!E_T$ and any (of two) leptons or jet.

	ee	$e\mu$	$\mu\mu$
DY	127.9±6.3±42.0	56.8±4.0±11.3	104.7±5.3±43.2
$t\bar{t}$	7.42±0.11±0.88	15.87±0.15±1.80	5.01±0.08±0.61
di-boson	3.48±0.03±0.38	6.74±0.04±0.82	2.58±0.02±0.30
e+fake	28.23±0.12±14.11	15.10±0.31±7.55	0
μ+fake	0	17.69±0.08±8.84	8.32±0.21±4.16
HF	14.3±5.2±11.6	56.5±11.2±19.4	15.6±6.2±12.3
Exp.Bkg.	181.2±8.2±45.8	169.±12.±25.	136.1±8.1±45.1
Obs.	165	130	135

Table 10.8
Pre-signal region before (dPhiMet_min) extra clean up cut.

	ee	$e\mu$	$\mu\mu$
DY	72.8±4.8±26.3	26.6±2.7±5.4	62.4±4.1±28.4
$t\bar{t}$	6.1±0.1±0.7	13.1±0.1±1.4	4.2±0.1±0.5
di-boson	3.5±0.1±0.6	6.2±0.1±1.1	2.1±0.0±0.4
l+fake	21.6±0.2±10.8	24.9±0.4±12.4	5.4±0.2±2.7
HF	9.1±4.1±7.4	30.6±7.9±10.5	8.5±4.3±6.7
Exp.Bkg.	113.1±6.3±29.8	101.4±8.4±17.6	82.6±5.9±29.6
Obs.	110	76	89

Table 10.9
Pre-signal region after (dPhiMet_min) extra clean up cut.

11. ANALYSIS

Now that we have all Control regions under control, we can look at our pre-signal region and do signal over background discrimination.

We use the program Corlim (with Bayesian statistics) to find expected 95% CL upper limits on the Stop cross section, at some 70 Stop-Snu points generated using the Pythia MC program. For speed, starting values of cut parameters near the optimum were found by pre-tuning using Signal/$\sqrt{Bkg.}$. All tuning is done one variable at a time, starting with $\not\!\!E_T$, and iterating as needed.

With the exception of the uncertainty on the theoretical Stop cross section, all uncertainties, both uncorrelated and correlated, including on the backgrounds, the Stop efficiency at each point, and the Luminosity, are incorporated into the UL estimates which are then compared to the central value of the theoretical Stop cross section.

A few variables discriminate MC signal from background: $\not\!\!E_T$, $d\phi$ (dilepton,$\not\!\!E_T$), $H_T = \not\!\!E_T + p_{T1} + p_{T2} + E_{Tj}$, p_{T2} , M_T (for each lepton), and p_T (dilepton).

Optimum cuts depend dominantly on the $\Delta M = M_{\tilde{t}} - M_{\tilde{\nu}}$ mass difference, and can be grouped into four sets, in bands parallel to the $M_{\tilde{t}} = M_{\tilde{\nu}} + M_b$ kinematic limit. These cut regions, labeled a through d, are shown in Fig.11.1 and details are given in the Table 11.1.

The Sliding cut plot for cut group a is shown in Figure 11.2. N-1 cuts for all variables used and all cut groups are shown in Figures 11.3, 11.4, 11.5, 11.6 - that is, plots where all cut variables have been used for a particular stop sneutrino mass point, and then the 95% CL cross section upper limit plotted vs. one variable at a time.

Vertical lines show the cut values used for that particular cut group region and are optimized for the entire cut group. Final cuts in each cut region are a compromise among tuning points.

Variables	Cut groups			
$\Delta M = M_{\tilde{t}} - M_{\tilde{\nu}}$, GeV/$c^2$	$5 < a <$ 47.5	$< b <$ 72.5	$< c <$ 87.5	$< d$
$\not\!\!E_T >$	25 GeV	32 GeV	32 GeV	32 GeV
$d\phi$(dilep-$\not\!\!E_T$)>	60°	60°	60°	60°
$p_{T2} >$	7 GeV/c	7 GeV/c	7 GeV/c	7 GeV/c
H_T min	—	>120 GeV	>130 GeV	>165 GeV
H_T max	<170 GeV	<225 GeV	<290 GeV	—
M_T (lep,$\not\!\!E_T$)>	15 GeV	11 GeV	—	—
p_T (dilep)<	Sliding Cut	—	—	—

Table 11.1
Cuts for different groups.

lep = both leptons, dilep = dilepton system, 2 = second (lower p_T) lepton.

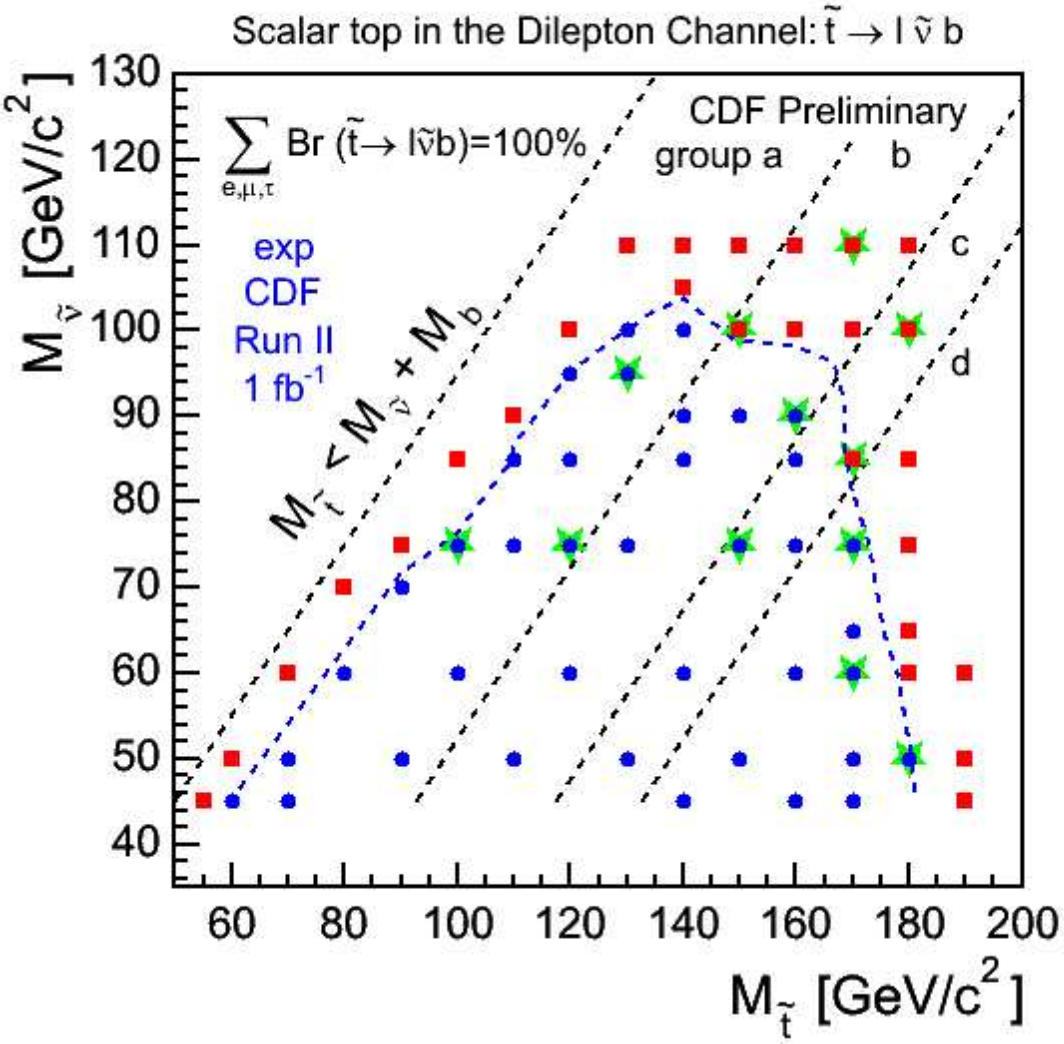

Figure 11.1. Expected exclusion contour.

Cut groups are defined by the Stop-Snu mass difference. Blue dots are excluded, red squares are not excluded, green stars used for tuning cuts.

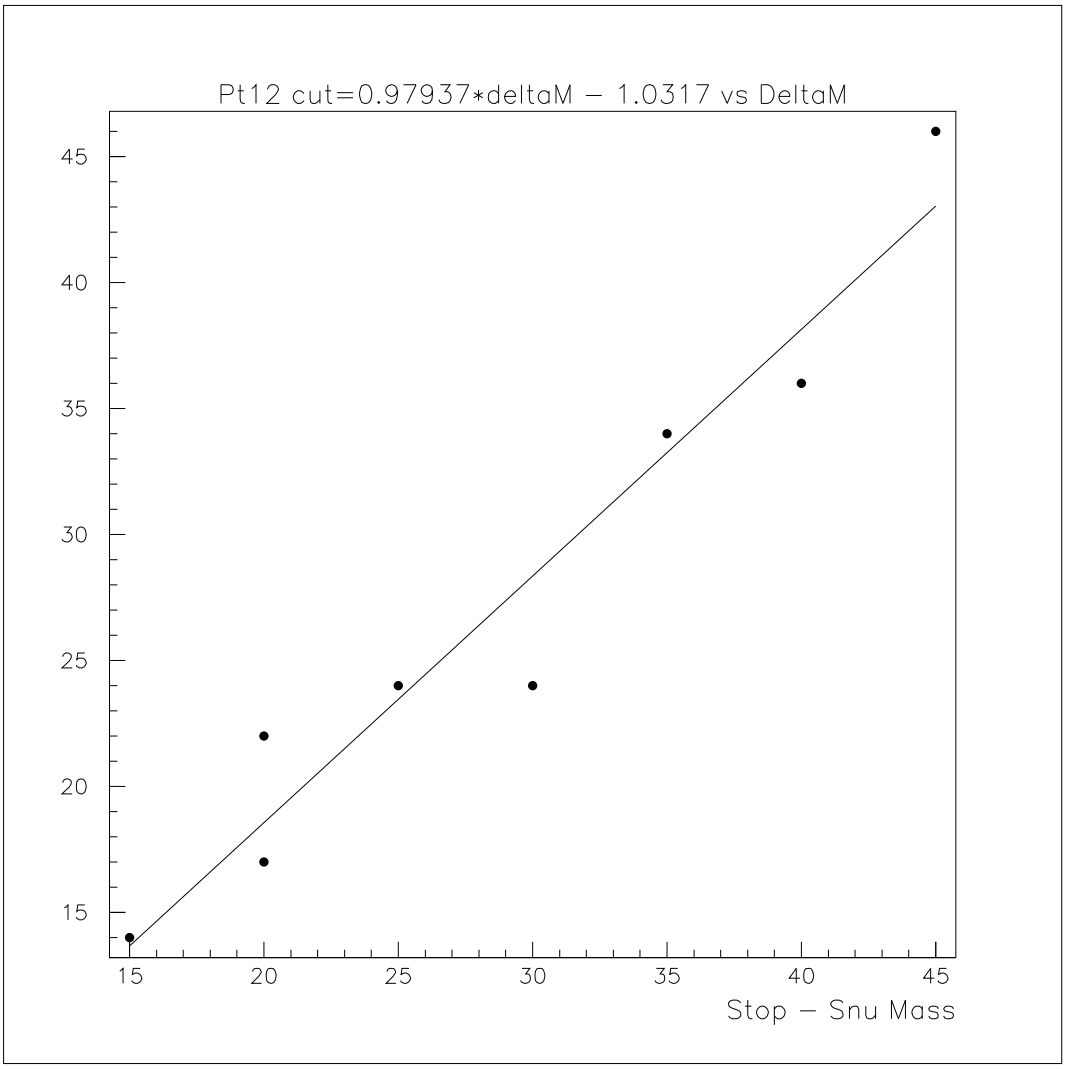

Figure 11.2. Sliding cut for group a.

The sliding cut values used are the straight-line fit to optimized values of this cuts in various sub-regions of region a P_{T12} Cut$= 0.98 * \Delta M - 1.03$.

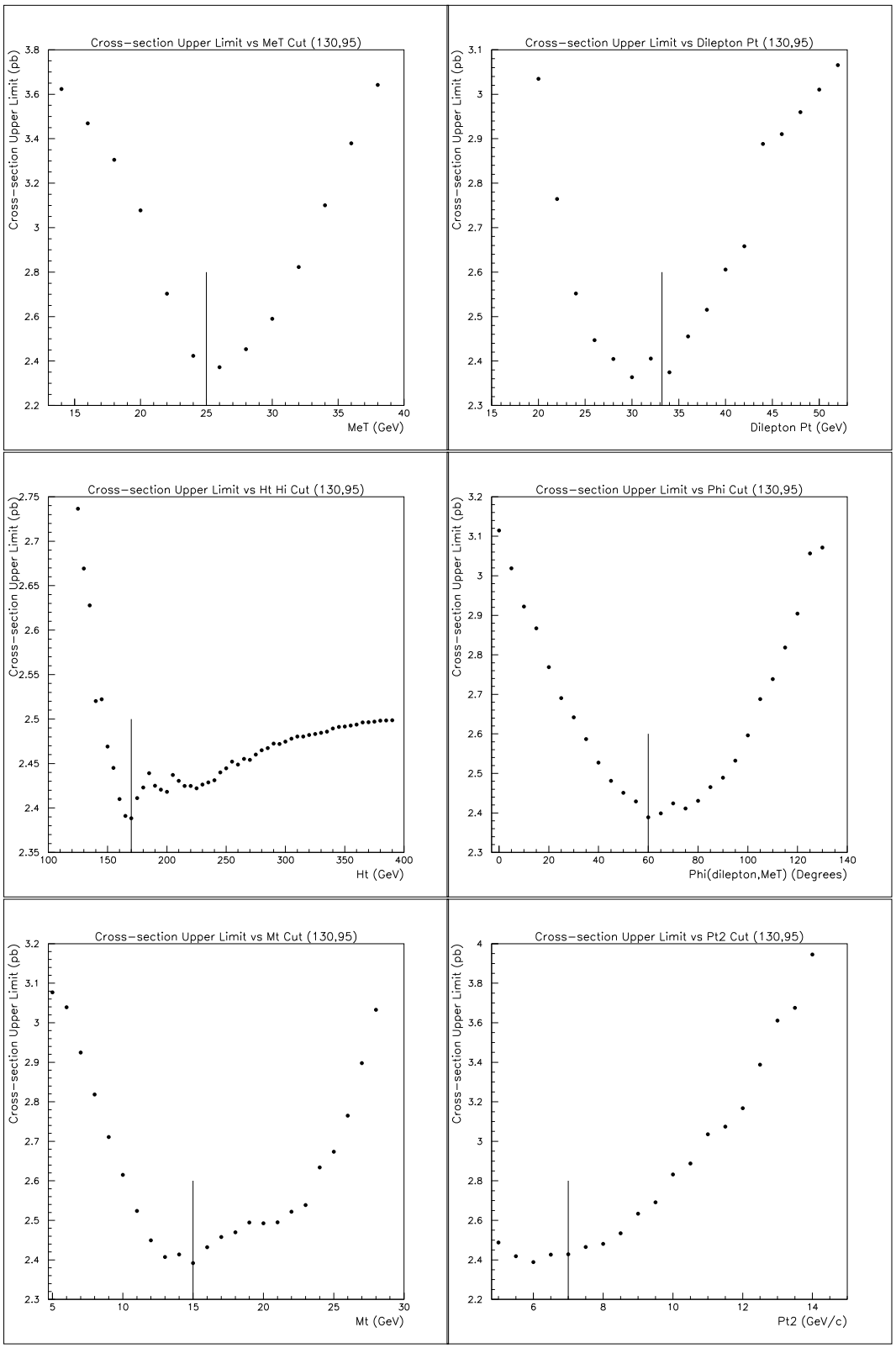

Figure 11.3. N-1 Cuts for group a for stop/sneutrino masses 130/95.

Indicated cuts are a compromise among the region a points used for cut tuning.

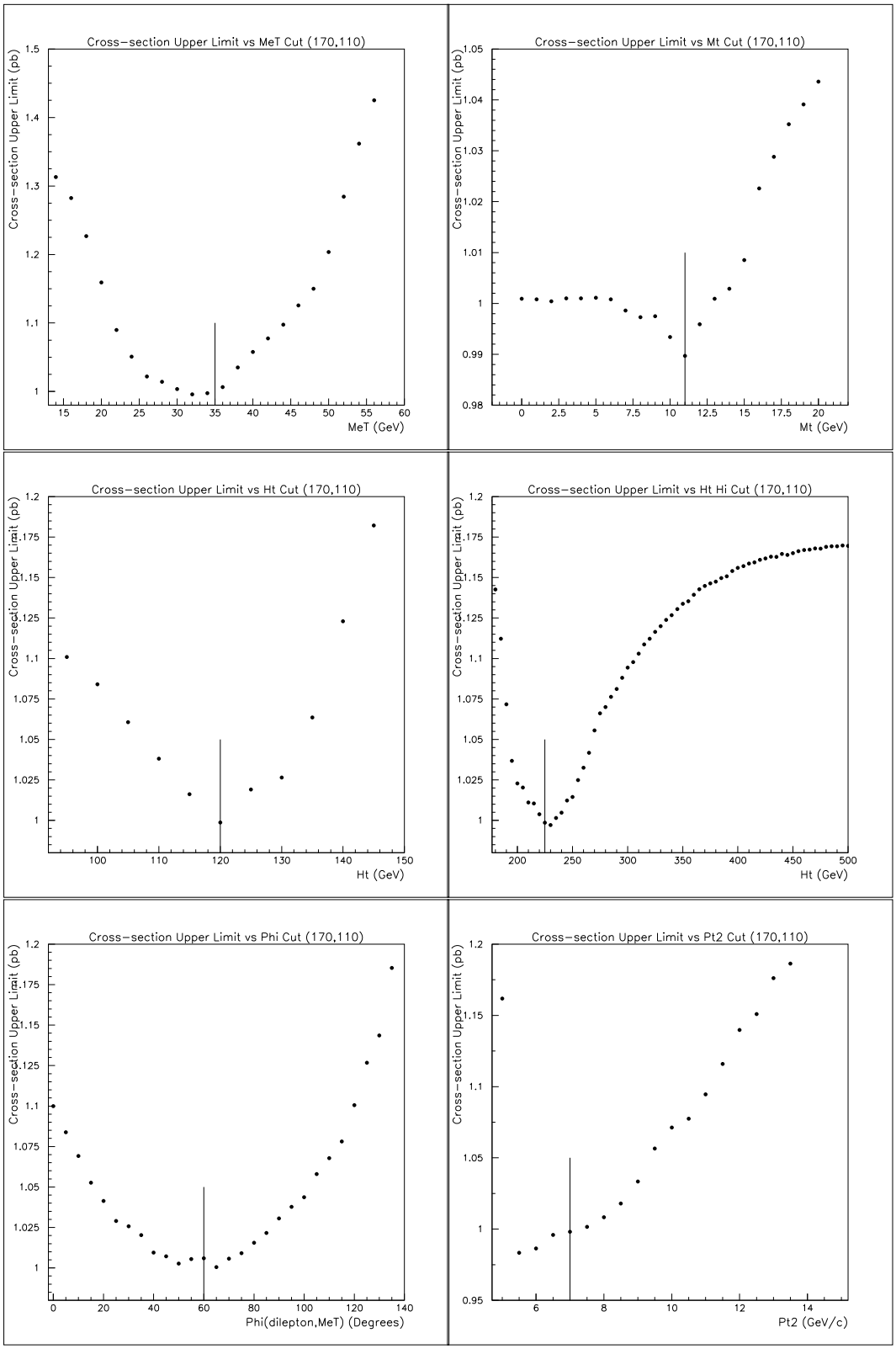

Figure 11.4. N-1 Cuts for group b for stop/sneutrino masses 170/110.

Indicated cuts are a compromise among the region b points used for cut tuning.

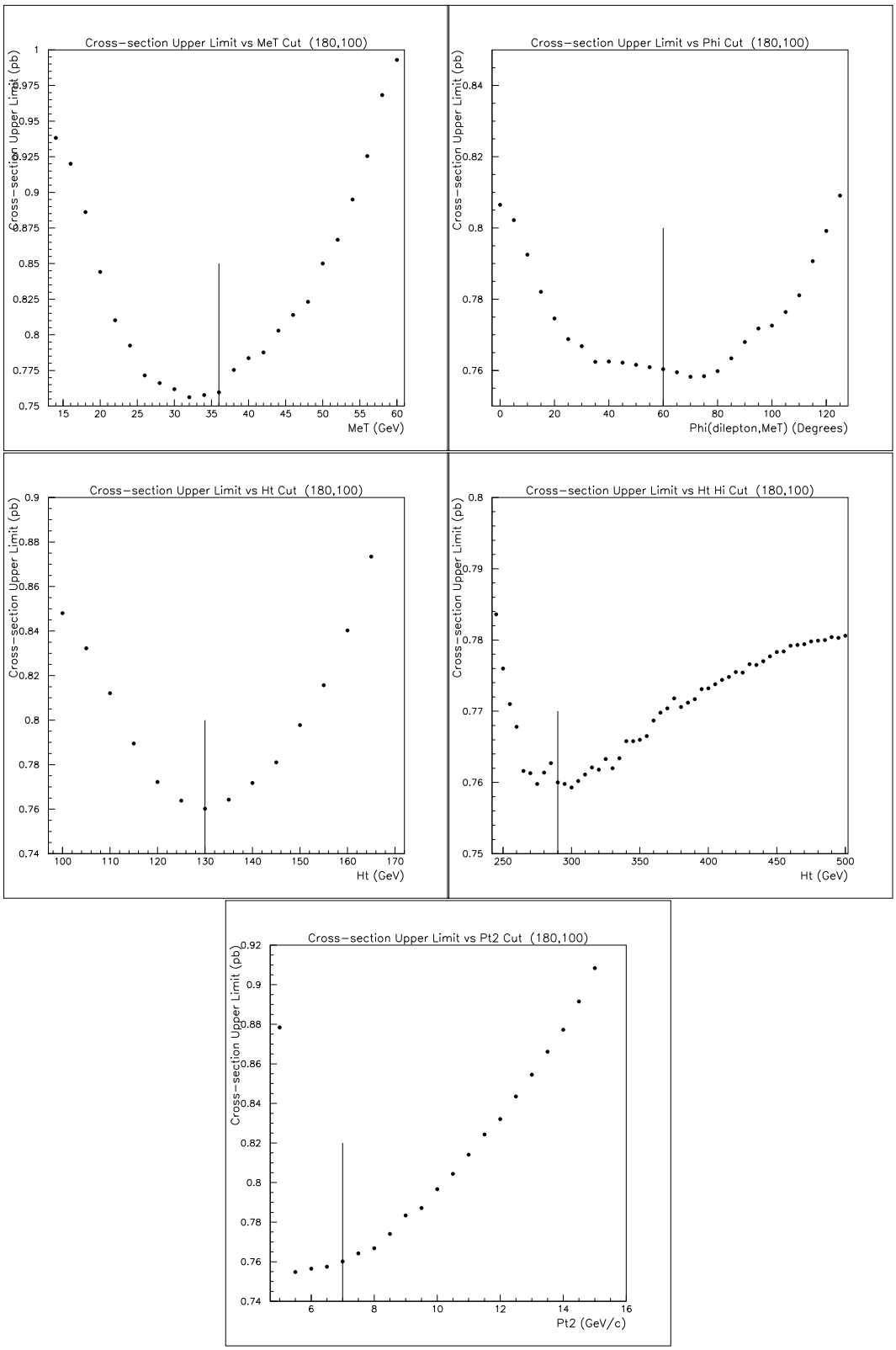

Figure 11.5. N-1 Cuts for group c for stop/sneutrino masses 180/100.

Indicated cuts are a compromise among the region c points used for cut tuning.

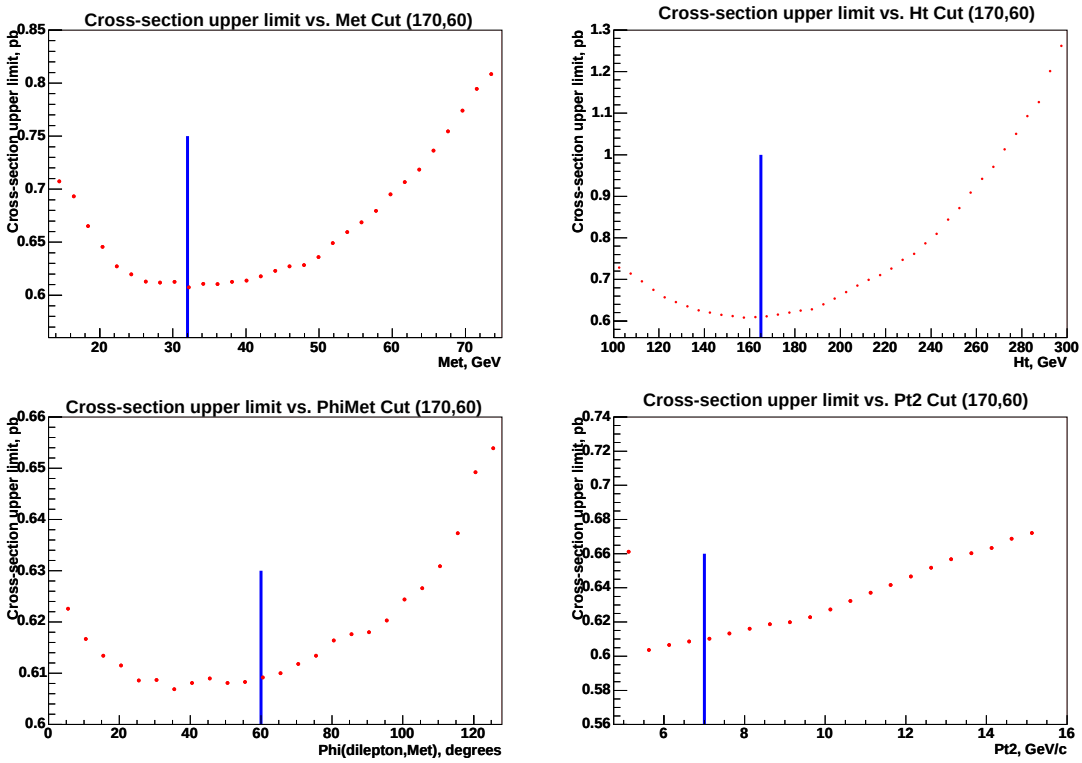

Figure 11.6. N-1 Cuts for group d for stop/sneutrino masses 170/60.

Indicated cuts are a compromise among the region d points used for cut tuning.

12. RESULTS

Now that the "blind" tuning of final cuts has been done, using signal Monte Carlo, we can unblind the data, and look for any significant excess of data compared to the sum of simulated backgrounds. If no significant excess is seen, we can use Corlim to calculate Observed upper limits on the stop cross section, now using observed numbers of events in a give cut region and using the stop efficiencies at a given stop-sneutrino mass point based on the MC-generated stop events at that point.

First, we plot a variety of kinematic distributions for the cleaned-up pre-signal region, then the "N-1" kinematic distributions for cut groups a, b, c, and d where all final cuts are applied except on the kinematic variable being plotted. Representative MC stop distributions are shown unshaded and stacked on the top of the stacked backgrounds. The data are the black points shown with error bars.

The kinematic distributions plotted are for $\not\!\!E_T$ and H_T . Figures 12.1, 12.2 show these distributions for pre-signal events. For cut group a, the N-1 distributions for these same kinematic variables are plotted in Figures 12.5, 12.9. Similar groupings for cut groups b, c, and d are shown in Figures 12.6, 12.10, Figures 12.7, 12.11 and Figures 12.8, 12.12.

The background expectations and data surviving the final cuts for cut groups a, b, c, and d are shown in Tables 12.1 through 12.4, respectively, broken down according to dilepton flavors. No significant excesses are seen for the ee and $e\mu$ events, or for the $\mu\mu$ events of cut group a (the smallest stop-sneutrino mass differences). In the other three cut groups, which happen to have a large overlap with each other in the events selected, there is a noticeable excess of observed $\mu\mu$ events compared to expectation.

Using numbers from Tables 12.2, 12.3, and 12.4, we find the Poisson probability of observing 8 or more events when 2.43 are expected is 0.35%, 9 or more events when 3.92 are expected is 1.9%, and 8 or more events when 4.38 are expected is 7.7%. These

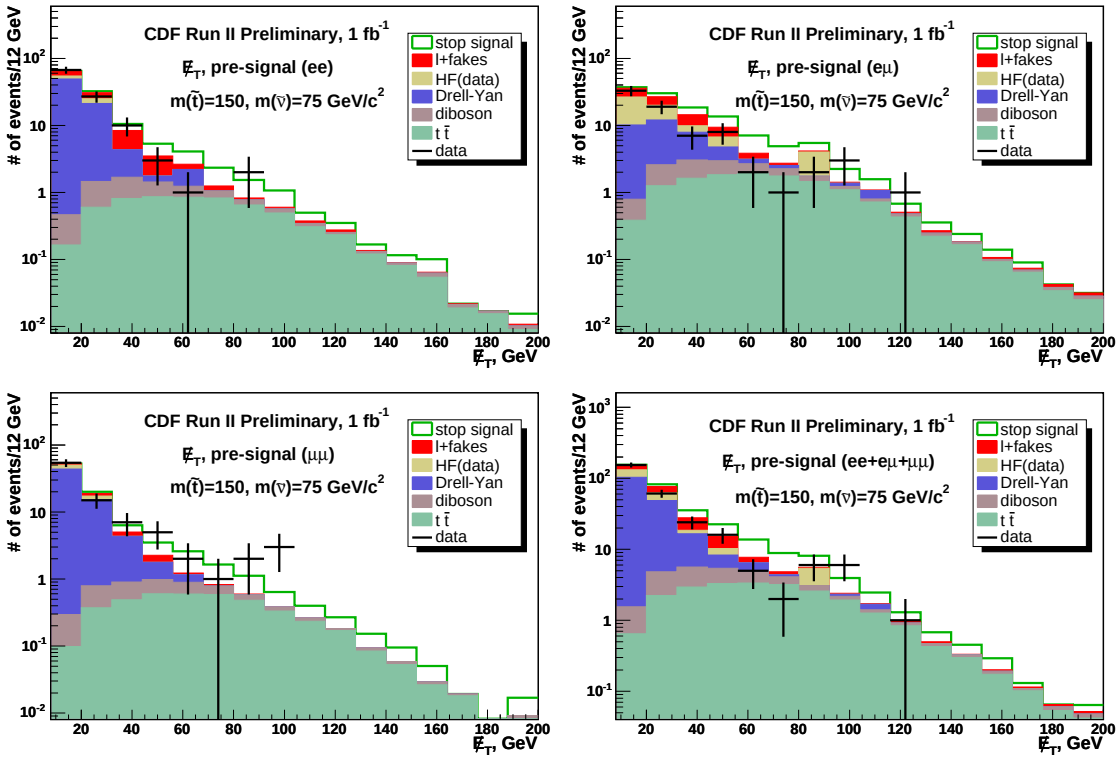

Figure 12.1. $\not\!\!E_T$ plots for pre-signal region.

probabilities are conservatively low because they do not take account of the assigned statistical and systematic uncertainties of the expectations. The most extreme case, cut group b, does not rise to the level of three standard deviations significance.

Whether or not one chooses to regard the di-muon "excess" as a hint, it is incompatible with the ee and $e\mu$ numbers - within the present theoretical model of stop pair production followed by decays with lepton universality and degenerate sneutrino masses.

Lists of the individual events passing at least one of the final cut group cuts are given in Appendix D, with indication of all of the cut groups that each event passes, along with values of a few of the main kinematic variables. The lists are in Tables D.1, D.2, and D.3 for emu, ee, and mumu events, respectively. Two of these events are also selected in a CDF trilepton analysis [21, 25] searching for chargino-neutralino

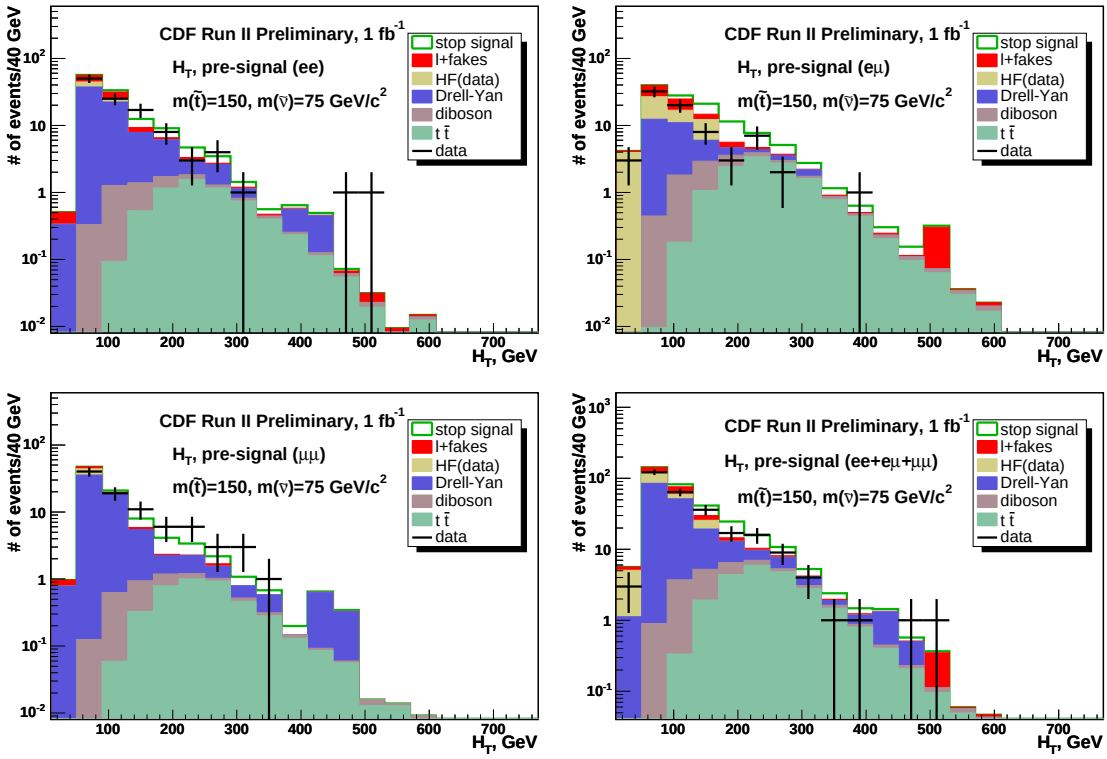

Figure 12.2. H_T plots for pre-signal region.

production. Their dilepton flavors (in our analysis) and Run/Event numbers are: ee (197716, 2528577) and $\mu\mu$ (211396, 9177382).

Appendix D also shows standard two-dimensional event displays for a three of the more striking events. Event displays of all the listed events have been scanned, and no obvious effects have been noticed that might be due to the detector.

We proceed to set 95% confidence level upper limits on the production cross section of stops, at some 70 points in the stop-sneutrino mass plane, using the program Corlim [29] with Bayesian statistics and using the three dilepton flavor channels jointly with full treatment of correlated and uncorrelated errors between them.

One-dimensional curves of the upper limits vs the theoretical cross section are shown in Figure 12.3, for groups of points with particular stop-sneutrino mass differences. It is seen that the cross section upper limits for a given delta-M tend to be rather independent of stop mass.

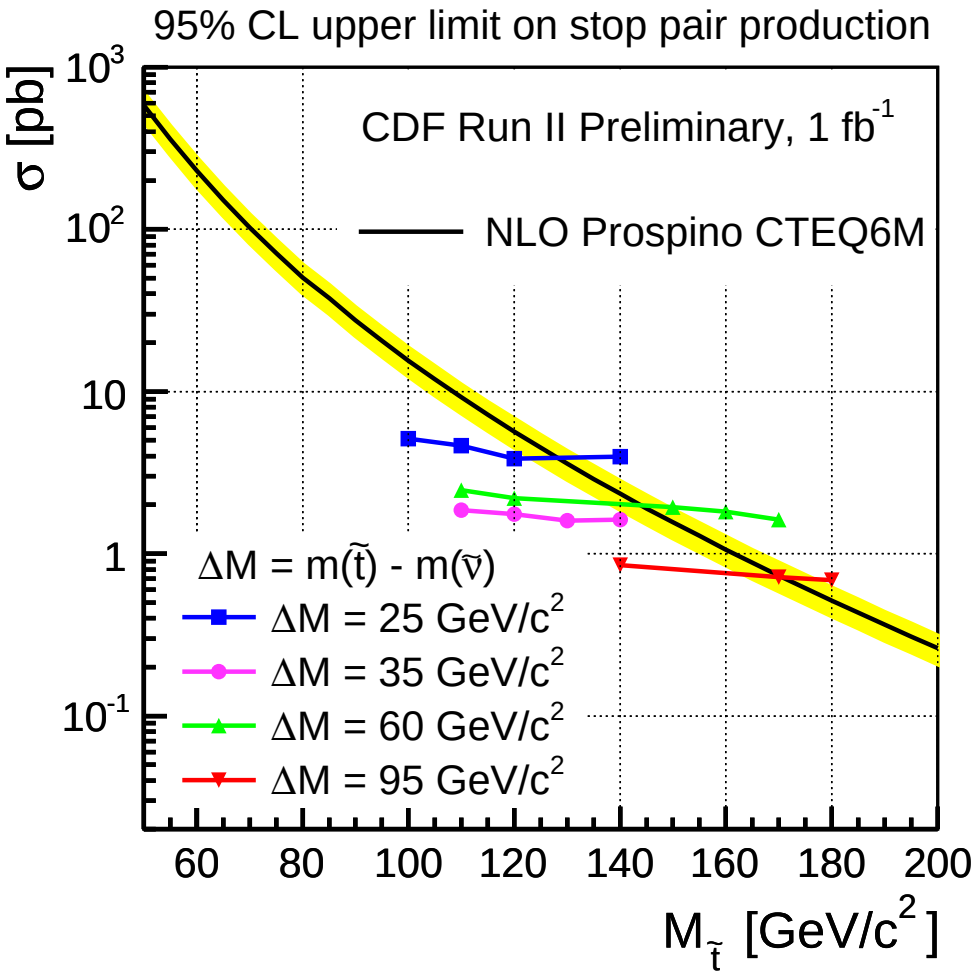

Figure 12.3. Limit plot.

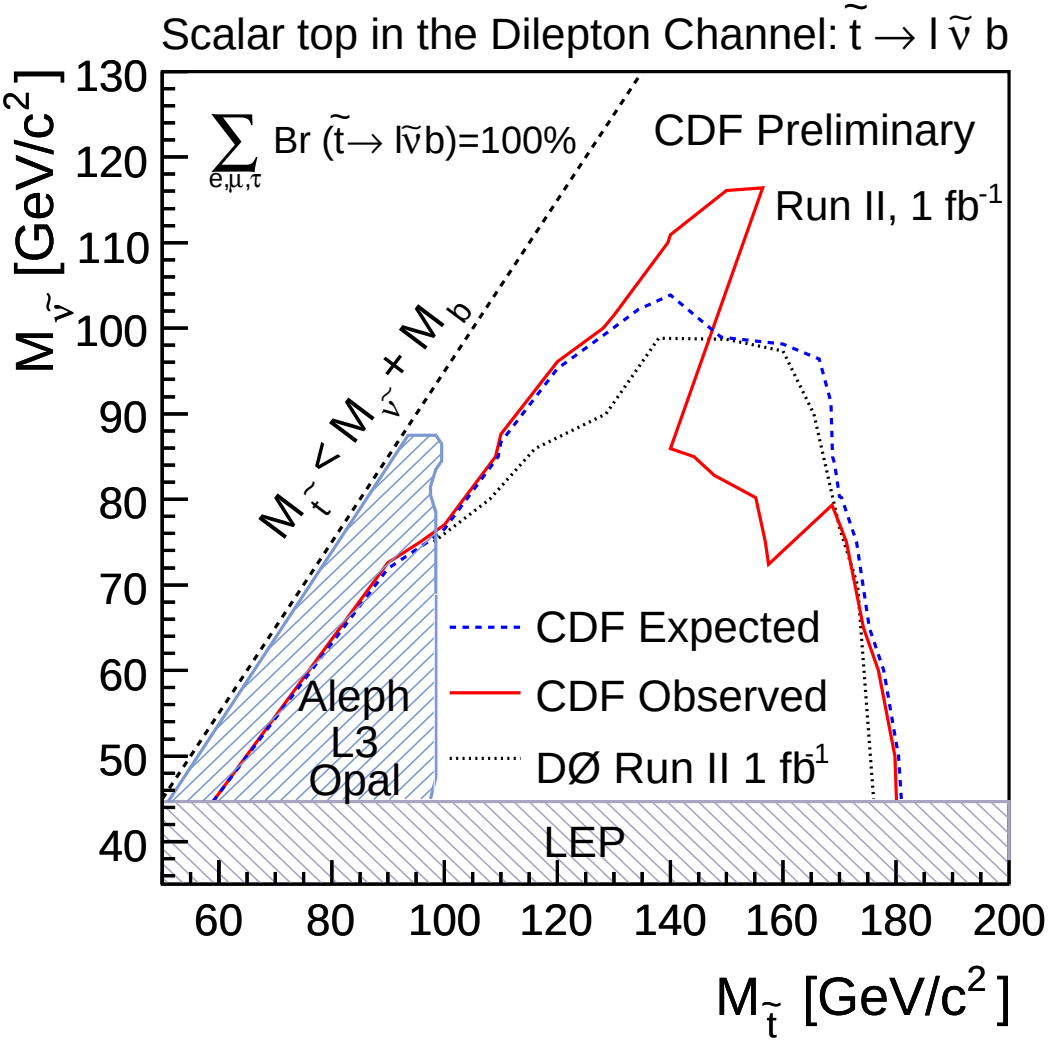

Figure 12.4. Observed/expected limits in a stop-sneutrino plane.

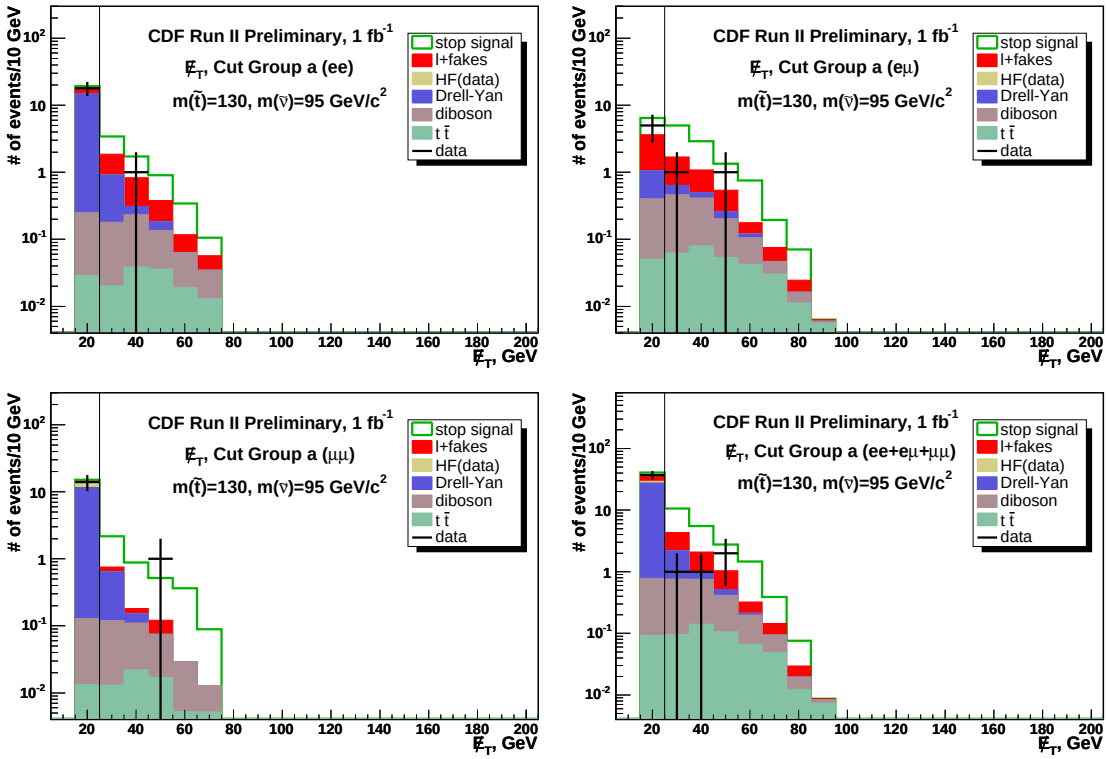

Figure 12.5. (N-1) $\not\!\!E_T$ plots for cut group a.

	ee	$e\mu$	$\mu\mu$	All
DY	0.86±0.19±0.31	0.32±0.10±0.06	0.56±0.15±0.26	1.8±0.3±0.6
$t\bar{t}$	0.13±0.01±0.01	0.28±0.02±0.03	0.06±0.01±0.01	0.5±0.0±0.1
di-boson	0.52±0.02±0.09	0.96±0.03±0.16	0.28±0.01±0.05	1.8±0.0±0.3
l+fake	1.74±0.04±0.87	2.01±0.09±1.00	0.18±0.03±0.09	3.9±0.1±1.7
Exp.Bkg.	3.25±0.20±0.93	3.57±0.14±1.01	1.08±0.15±0.28	7.9±0.3±1.9
$\tilde{t}\bar{\tilde{t}}$ (130/95)	3.25±0.32±0.36	6.64±0.43±0.68	2.92±0.27±0.32	12.8±0.6±1.3
Obs.	1	2	1	4

Table 12.1
Cut group a results for (130/95).

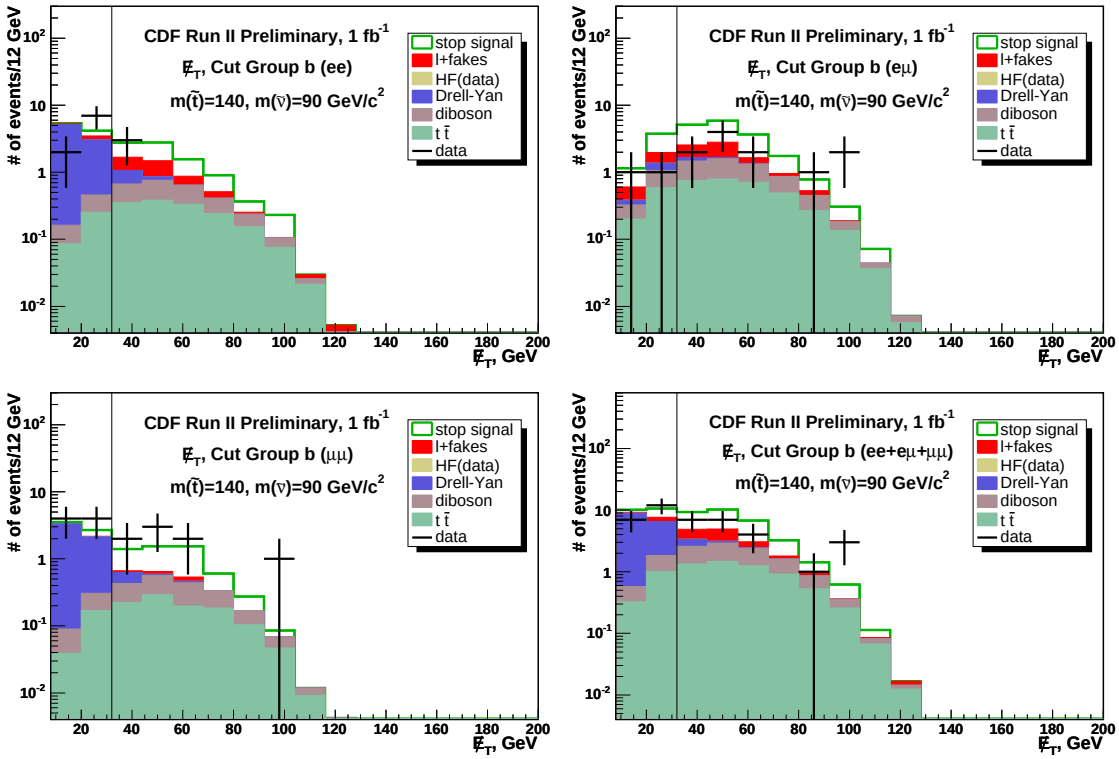

Figure 12.6. (N-1) $\not\!\!E_T$ plots for cut group b.

	ee	$e\mu$	$\mu\mu$	All
DY	0.49±0.15±0.18	0.28±0.09±0.06	0.25±0.10±0.11	1.0±0.2±0.4
$t\bar{t}$	1.57±0.05±0.17	3.20±0.07±0.34	1.06±0.04±0.12	5.8±0.1±0.6
di-boson	1.28±0.02±0.21	2.75±0.03±0.47	0.96±0.01±0.17	5.0±0.0±0.9
l+fake	1.59±0.03±0.80	2.50±0.12±1.25	0.16±0.04±0.08	4.3±0.1±1.8
Exp.Bkg.	4.93±0.15±0.86	8.73±0.17±1.38	2.43±0.12±0.25	16.1±0.3±2.3
$\tilde{t}\bar{\tilde{t}}(140/90)$	3.71±0.29±0.33	8.85±0.42±0.72	3.02±0.23±0.28	15.6±0.6±1.3
Obs.	3	11	8	22

Table 12.2
Cut group b results.

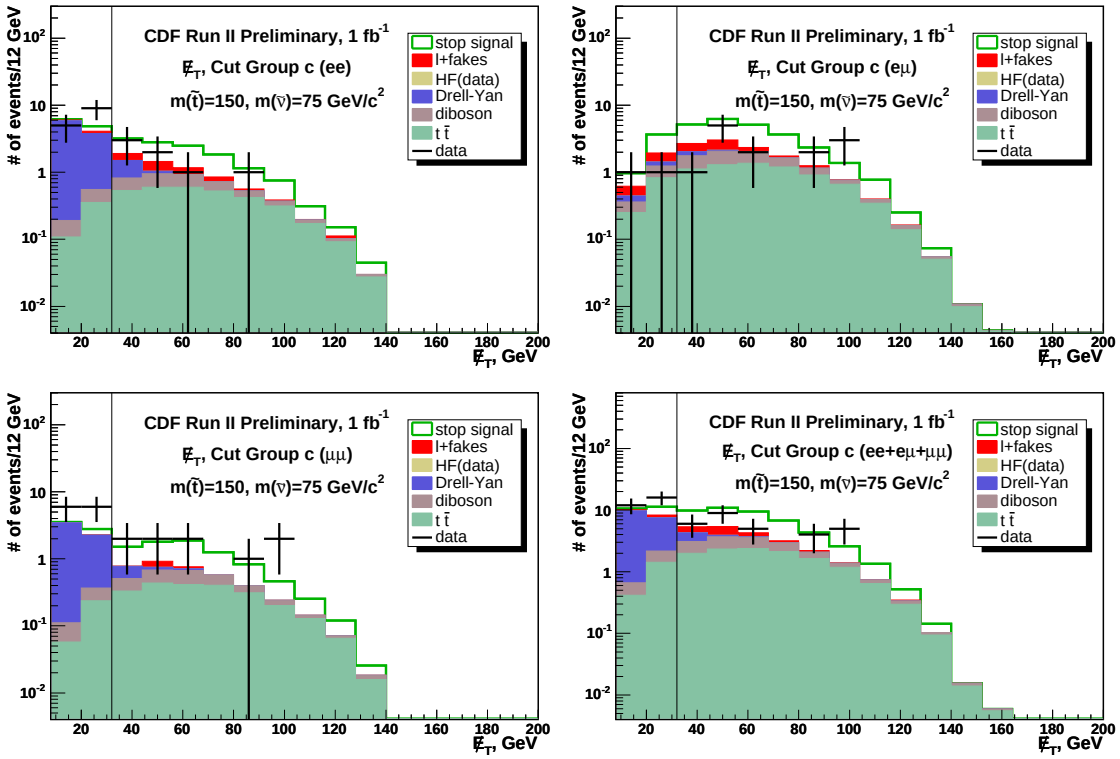

Figure 12.7. (N-1) $\not\!\!E_T$ plots for cut group c.

	ee	$e\mu$	$\mu\mu$	All
DY	0.78±0.18±0.28	0.33±0.09±0.07	0.37±0.11±0.17	1.5±0.2±0.5
$t\bar{t}$	3.28±0.07±0.36	7.11±0.10±0.75	2.31±0.06±0.26	12.7±0.1±1.4
di-boson	1.36±0.02±0.23	2.93±0.03±0.50	1.00±0.01±0.18	5.3±0.0±0.9
l+fake	1.25±0.03±0.62	2.10±0.12±1.05	0.24±0.08±0.12	3.6±0.1±1.5
Exp.Bkg.	6.67±0.20±0.80	12.47±0.18±1.39	3.92±0.15±0.38	23.1±0.3±2.6
$\tilde{t}\bar{\tilde{t}}(150/75)$	6.08±0.24±0.46	12.6±0.3±0.9	4.21±0.18±0.34	22.9±0.4±1.6
Obs.	7	13	9	29

Table 12.3
Cut group c results.

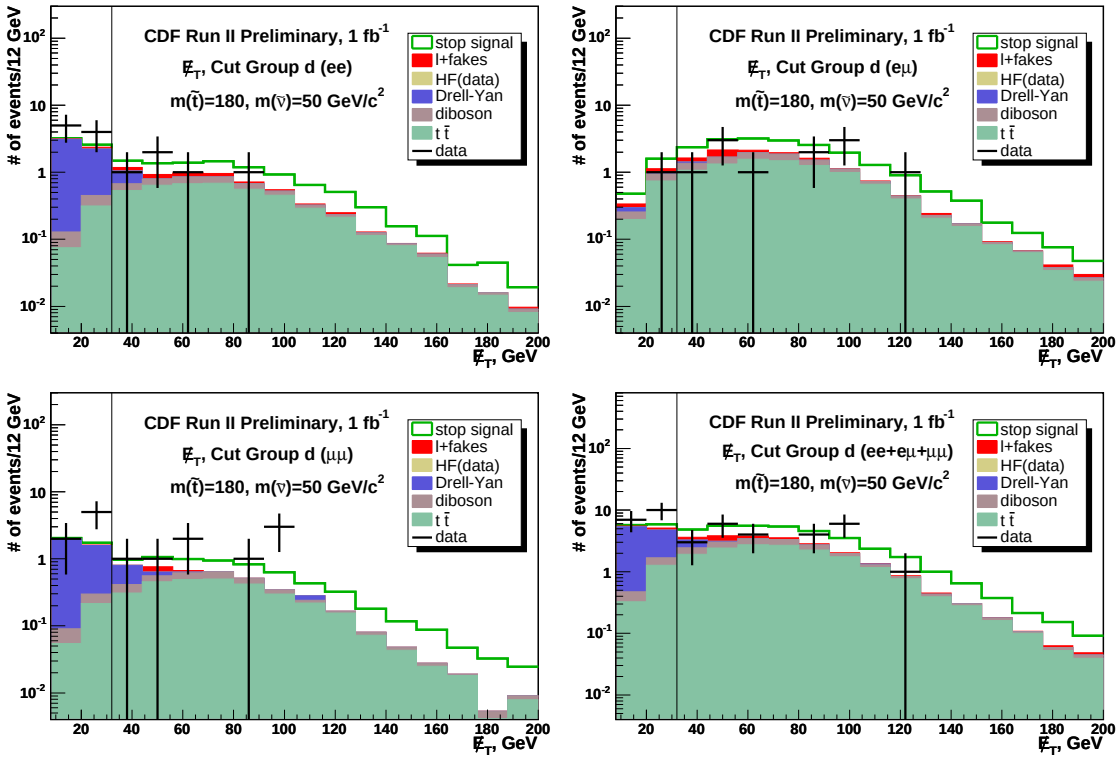

Figure 12.8. (N-1) $\not\!\!E_T$ plots for cut group d.

	ee	$e\mu$	$\mu\mu$	All
DY	0.37±0.13±0.13	0.06±0.04±0.01	0.52±0.14±0.24	1.0±0.2±0.4
$t\bar{t}$	4.37±0.08±0.48	9.37±0.12±0.99	3.04±0.06±0.35	16.8±0.2±1.8
di-boson	0.89±0.01±0.15	1.93±0.02±0.33	0.67±0.01±0.12	3.5±0.0±0.6
l+fake	0.61±0.02±0.30	1.36±0.16±0.68	0.15±0.07±0.08	2.1±0.2±0.9
Exp.Bkg.	6.24±0.15±0.60	12.72±0.20±1.25	4.38±0.17±0.45	23.3±0.3±2.4
$\tilde{t}\bar{\tilde{t}}$ (180/50)	3.45±0.12±0.24	7.26±0.16±0.49	2.34±0.09±0.18	13.0±0.2±0.9
Obs.	5	11	8	24

Table 12.4
Cut group d results.

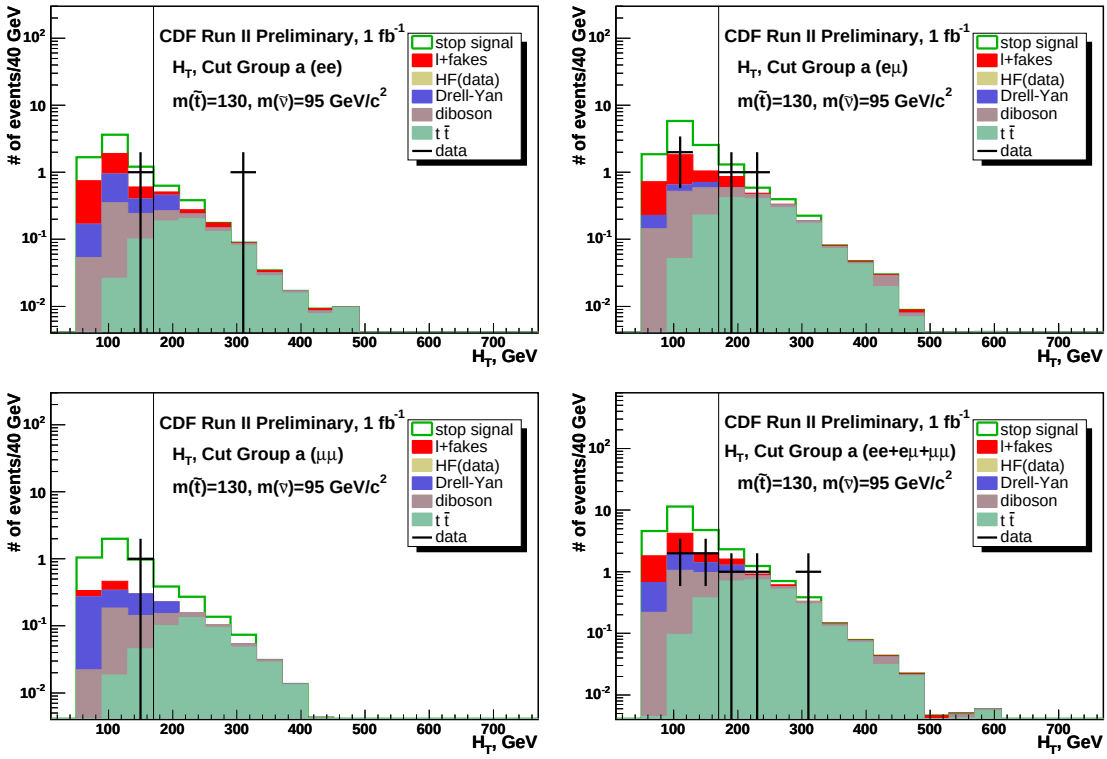

Figure 12.9. (N-1) H_T plots for cut group a.

We then establish the observed exclusion contour shown in Figure 12.4 by comparing the many stop-sneutrino points with the central value of the theoretical NLO Prospino stop cross section. We interpolate linearly between nearby points inside and outside the exclusion boundary, using the difference of the theoretical and observed upper limit cross sections.

The contour extends the world exclusion limits (compared with DØ Collaboration results [30]) to higher sneutrino masses for stop masses in the range 135 to 155 GeV/c2, and to higher stop masses, up to 180 GeV/c2, for low sneutrino masses.

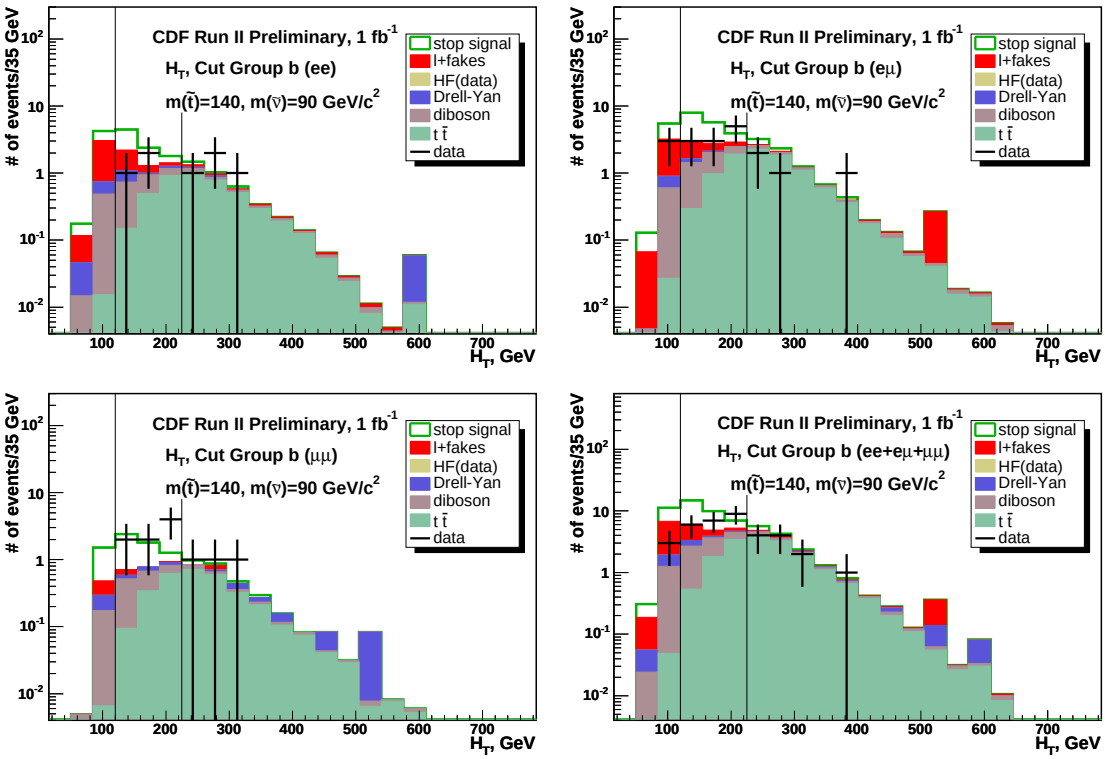

Figure 12.10. (N-1) H_T plots for cut group b.

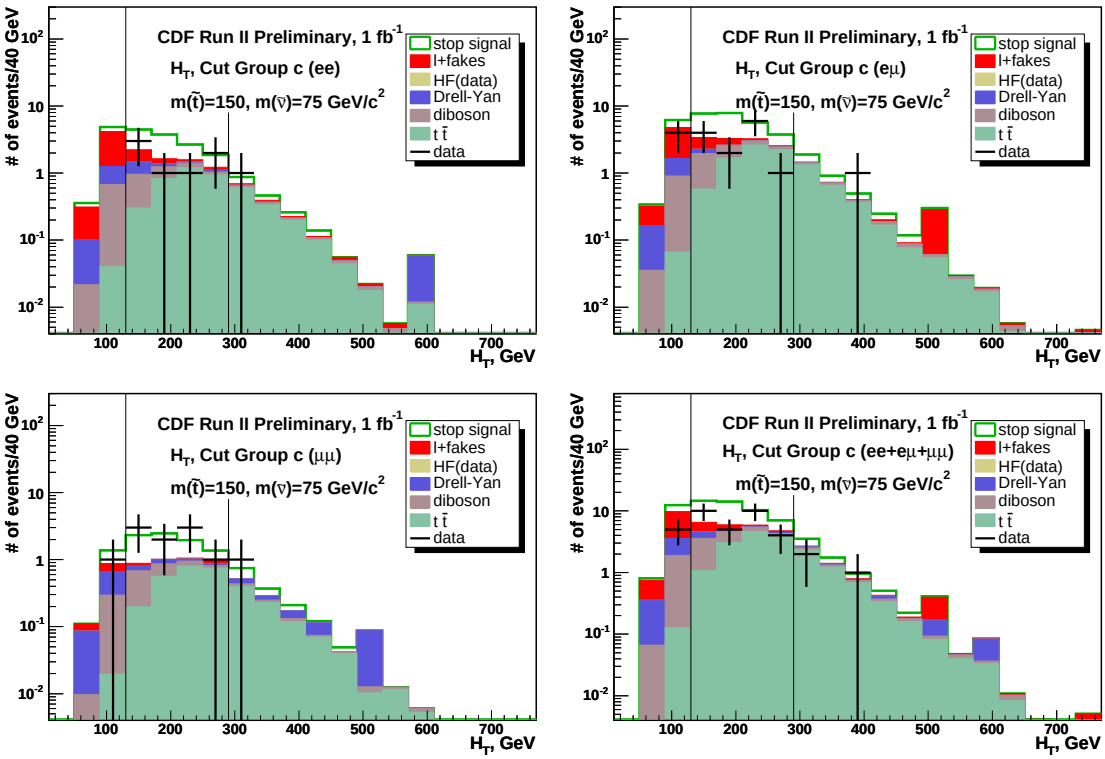

Figure 12.11. (N-1) H_T plots for cut group c.

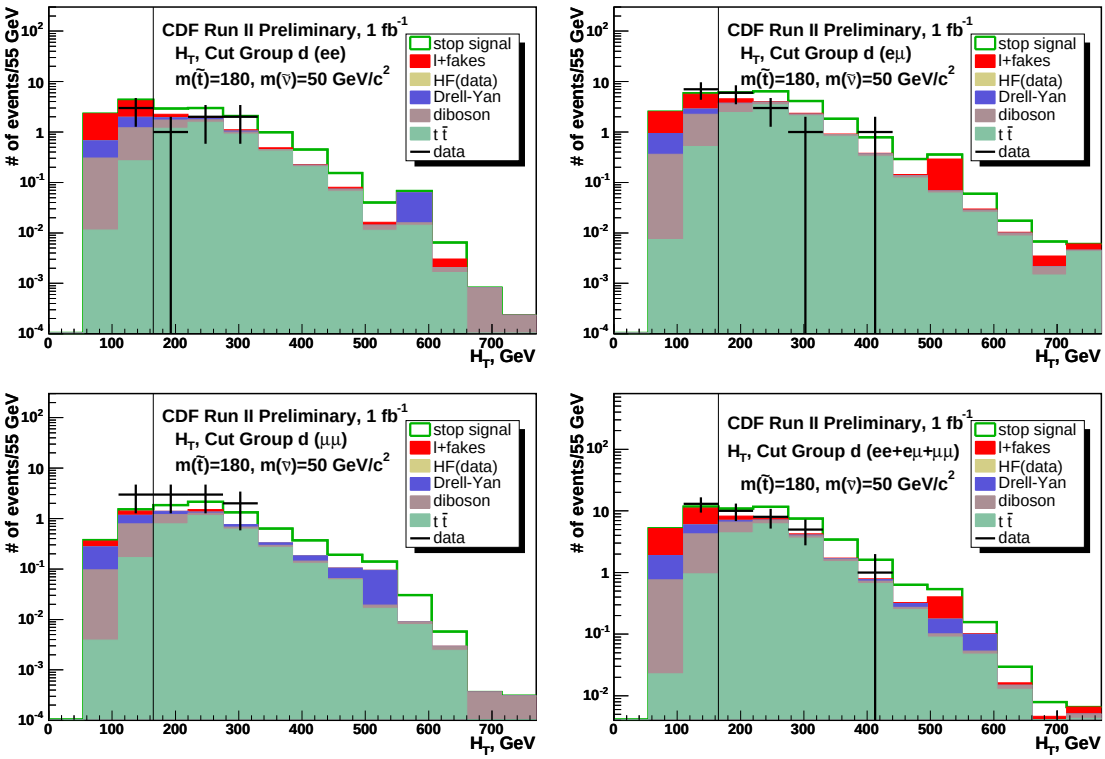

Figure 12.12. (N-1) H_T plots for cut group d.

13. SUMMARY

We present a search for the lightest stop quark using a total of $\mathcal{L} = 1$ fb^{-1} of data collected by the CDF experiment. No statistically significant evidence of the stop signal has been found in a model with degenerate sneutrino ($\tilde{\nu}$) masses. New limits at 95% confidence level in the stop mass versus sneutrino mass plane have been set. Observed exclusion limits extend world limits to higher Sneutrino mass for stop masses in the range 135 to 155 GeV/c^2, and to higher stop masses, up to 180 GeV/c^2, for low sneutrino masses.

APPENDICES

A. Monte Carlo (MC) programs used

The CDF MC samples that were used in this analysis are shown in the table below.

Process	Official name	Source (WG)	X-section Eff.(pb)	N events (w GRL)	Luminosity (fb^{-1})	K-factor (used)	Willis factor
$t\bar{t}$ (m_t=175)	ttop75	Top	6.7±0.5	3686412	550.2	NLO	95.7%
Z→ ee	zexode	EWK	1272±25	4915100	2.760	1.4	93.6%
Z→ $\mu\mu$	zexodm	EWK	1272±25	4983372	2.798	1.4	93.8%
Z→ $\tau\tau$	zexodt	EWK	1272±25	4977932	2.795	1.4	93.3%
WW	wewk5d wewkbd	EWK	1.27±.08	4712655	3711	NLO	95.9%
WZ	wewk6d wewkcd	EWK	0.277±.022	4896600	17677	NLO	96.2%
ZZ	wewk7d wewkdd	EWK	0.348±.035	4702632	13513	NLO	96.1%
W$\gamma \to e\nu\gamma$	rewk06	EWK	21.5±1.5	2623489	91.06	1.34	95.1%
W$\gamma \to \mu\nu\gamma$	rewk07	EWK	21.5±1.5	2532455	87.9	1.34	95.3%

Sources of the Monte Carlo samples are different physics Working Groups (WG). Only events passing our Good Run List (GRL) were used in the table. The effective cross section in the table is the theoretical cross section times filter efficiency; and K-factor is the ratio of Next to Leading Order (NLO) to Leading Order (LO) cross sections. It is used to correct LO theoretical cross section. The "Willis factor" is a Luminosity factor defined in [31] and is needed to take into account the rejection of primary event vertices more than ±60 cm in Z along the beamline from the center of the detector.

Sources :

http://www-cdf.fnal.gov/internal/physics/top/RunIIMC/topmc6/index.shtml

http://www-cdf.fnal.gov/tiki/tiki-index.php?page=EwkDatasets

http://www-cdf.fnal.gov/internal/physics/exotic/susy/mc_samples.html

B. Heavy Flavor estimation from data

Heavy flavor background is estimated from data, and is used for our control region comparisons but note that **no HF(data) events survive our final analysis cuts**.

We define a "scaling region" with Dilepton Invariant Mass (InvM) between **15 < InvM < 35 GeV/c^2** where all MC-generated SM backgrounds are found to be negligible, except for DY, and for lepton+fake lepton events estimated from data. Dilepton data are routinely required to have small impact parameter ("d0") to remove as much bb and cc as possible. These standard impact parameter cuts are: d0 < 0.2 cm using the COT, or d0 < 0.02 cm using SVX tracking if available.

Dilepton data in the above mass interval still show an excess over the sum of DY + "fakes". We attribute this excess to un-removed bb and cc events. We also attribute events failing the standard impact parameter cuts, so-called "inverse d0 cut events", to bb and cc, and for each dilepton flavor combination, we calculate the scale factor R = "excess"/"inverse d0" (listed within each of the HF plots shown in Figure B.1, for the three data periods used in this analysis). We assume that the scale factor for a given flavor combination applies universally to events of that dilepton flavor and run period, and model the un-removed HF background in any kinematic region by scaling the "inverse d0" events in that region.

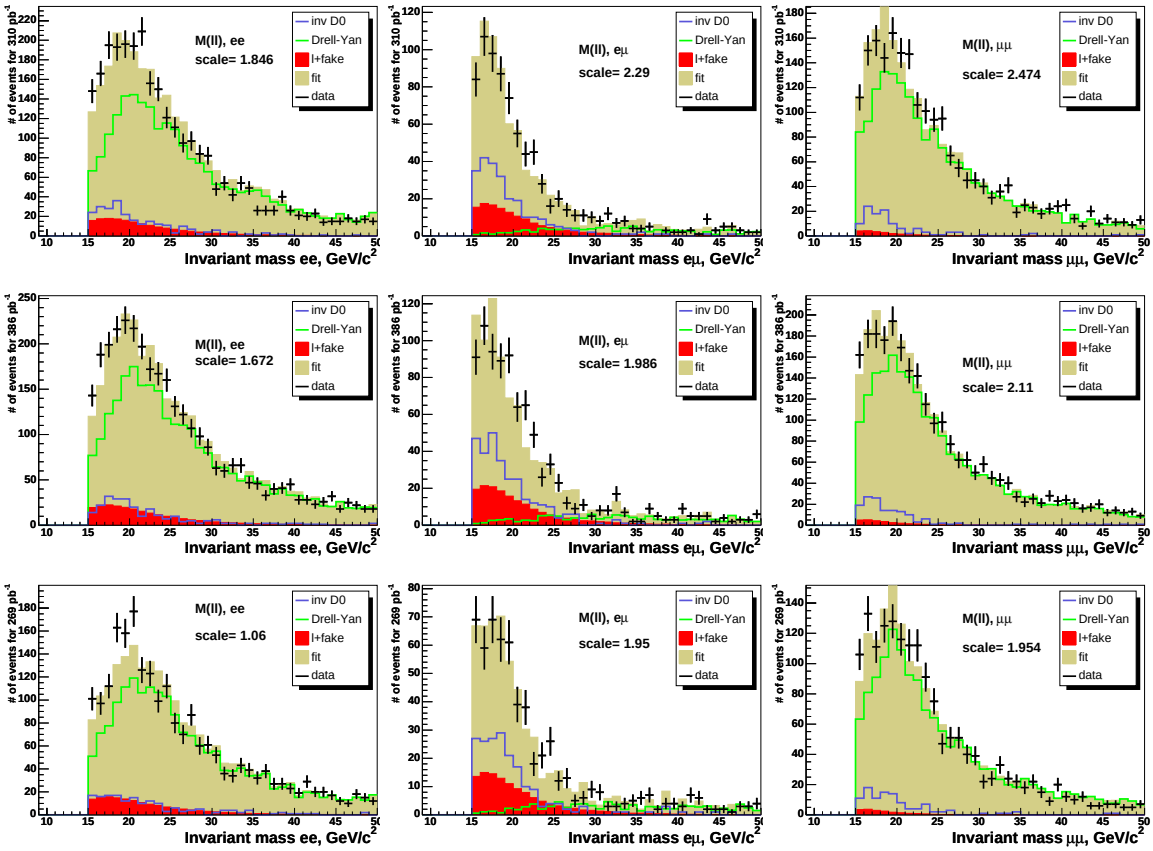

Figure B.1. Invariant mass distributions used to calculate scale factors for HF estimation from data, using inverse d0 data, lepton + fake and DY MC samples for different data periods (d,h,i) and lepton flavors (opposite sign only).

C. Misidentified leptons

"Misidentified leptons" (or "fake" leptons) are either hadrons misidentified as leptons or uninteresting leptons from decays in flight of pions and kaons. These events could play a very important role in understanding the analysis. In the Run I analysis [17,32], such misidentified leptons were comparable in number to the Standard Model backgrounds and required careful tuning of cuts based on special event samples. In this analysis "stubless" muons (CMIO) - tracks, which have minimum ionization in the calorimeter but do not have matching hits in the muon tracking system - are also considered as "Misidentified leptons", because they do not pass our muon ID cuts.

The detailed procedure was described in CDF note 7470 [33] and was successfully used by the trilepton group. We used the trilepton analysis muon "fake probabilities" while electron "fake probabilities" were tuned up by Beate Heinemann specifically for this analysis.

As we know, pure Monte Carlo and Detector Simulation events are not adequate for fake estimations. It is necessary to use real events from CDF data samples which are not a part of the stop search sample – such as events passing a single lepton trigger. In this analysis such samples were the 8 GeV/c electron calibration trigger sample (blpcad) and the 8 GeV/c muon calibration trigger sample (bmclad). For this analysis those samples were filtered by Else Lytken.

To find the "fake" leptons contribution, we apply a "fake rate" to each fakeable object, if any, (tracks in case of muons and jets in case of electrons) in each event of the calibration sample, with condition that we can find such object. We use each event several times if several fakeable objects can be found in the event. In each "event" we treat only one fakeable object, as either a muon or an electron. and apply all analysis cuts.

Since muons are MIPs, in order to correct the $\not\!\!E_T$ we subtract only 2 GeV (the mean ionization loss in the calorimeter for a muon) from the calorimeter (and not the actual deposited energy) and add p_T of the track.

The systematic error on lepton+fakes is taken to be 50% .

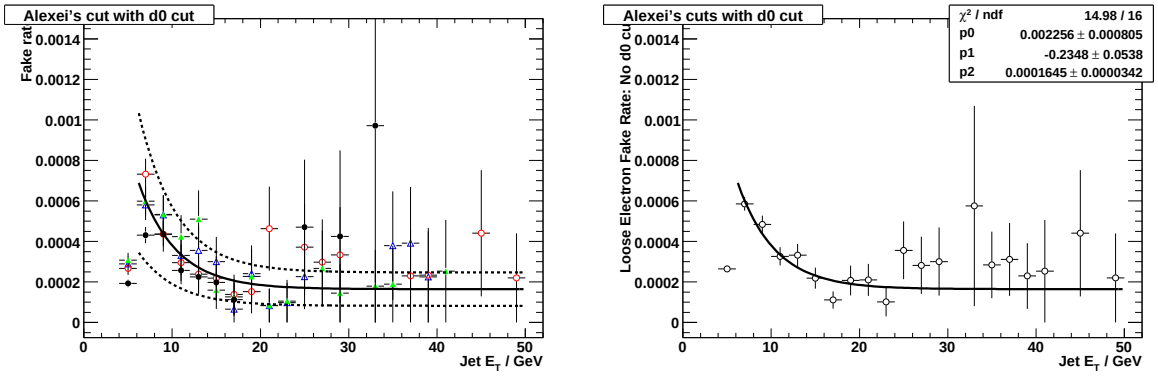

Figure C.1. Plots of misidentified electrons rates for various jet trigger samples (left) and average one (right) with fake rate parametrization.

D. List of data events passed analysis cuts.

run #	event #	Cut	p_{T1}	p_{T2}	p_{T12}	$\not\!\!E_T$	H_T	E_{Tj}
154209	1181321	bcd	54.67	16.27	61.68	92.34	215.23	51.94
155114	478702	bcd	34.40	28.44	5.93	84.65	222.39	74.87
167634	432778	bc	35.82	8.92	44.44	49.08	131.13	37.31
177418	1252581	bcd	41.86	37.98	77.50	50.96	179.92	49.11
184495	1703544	b	53.69	9.79	47.92	35.24	120.24	21.52
192892	7128619	bc	34.10	25.05	46.11	56.80	133.02	17.06
193372	2651085	bcd	22.87	14.27	30.87	65.16	192.80	90.50
193892	345334	d	76.10	50.23	62.44	122.49	393.28	144.46
195261	554777	a	33.66	15.96	30.42	48.94	117.22	18.64
196275	2879207	bc	39.86	24.06	52.74	55.79	159.76	40.06
196473	3624629	bcd	36.76	26.96	63.69	47.66	167.99	56.61
204469	4242498	cd	38.68	15.57	46.37	97.02	232.82	81.54
206326	5463082	bcd	69.58	14.66	84.24	41.84	212.07	85.98
206700	4237419	cd	73.35	46.55	75.29	89.06	227.35	18.39
207156	2387787	bcd	41.77	26.25	67.00	95.90	215.11	51.20
209191	2272489	cd	121.94	81.12	50.58	45.79	276.11	27.27
209986	9485361	a	18.90	14.63	30.78	26.57	91.11	31.01

Table D.1
$e\mu$ events.

run #	event #	Cut	p_{T1}	p_{T2}	p_{T12}	$\not\!\!E_T$	H_T	E_{Tj}
153374	2276742	cd	72.02	56.87	127.70	53.87	271.51	88.75
162396	627907	cd	78.79	14.34	65.01	67.77	188.28	27.38
178759	4142707	abc	20.41	7.53	13.17	39.99	159.74	91.81
186598	4194951	cd	54.50	36.05	89.38	44.92	227.30	91.82
197716	2528577	abc	23.68	17.27	35.18	36.31	138.87	61.61
198695	5284824	d	109.27	81.38	27.90	39.98	308.91	78.20
204679	1899766	cd	104.34	58.20	46.19	80.07	285.90	43.29
206836	1380873	bc	39.06	23.73	35.41	37.31	164.19	64.09

Table D.2
ee events.

run #	event #	Cut	p_{T1}	p_{T2}	p_{T12}	$\not\!\!E_T$	H_T	E_{Tj}
150443	684273	bcd	92.50	21.10	109.54	64.83	224.98	46.54
154654	7344016	bcd	59.70	52.45	87.63	56.21	209.96	41.60
162310	667894	d	120.91	13.84	127.72	102.48	315.79	78.55
165198	1827962	bcd	34.61	23.77	52.56	100.41	224.10	65.31
193991	1042119	cd	45.31	34.51	79.47	84.54	244.36	80.00
198423	3943347	bc	45.05	38.43	62.02	54.58	156.39	18.33
199025	7143282	bcd	104.50	9.45	100.87	33.27	194.28	47.06
203265	4804785	cd	108.26	16.68	91.64	99.05	279.79	55.80
207079	5681255	b	41.03	15.28	55.86	48.37	120.26	15.58
211396	9177382	bc	45.12	21.24	63.25	33.83	144.84	44.66
211441	7455273	abcd	32.26	20.28	18.58	48.31	166.06	65.22

Table D.3
$\mu\mu$ events.

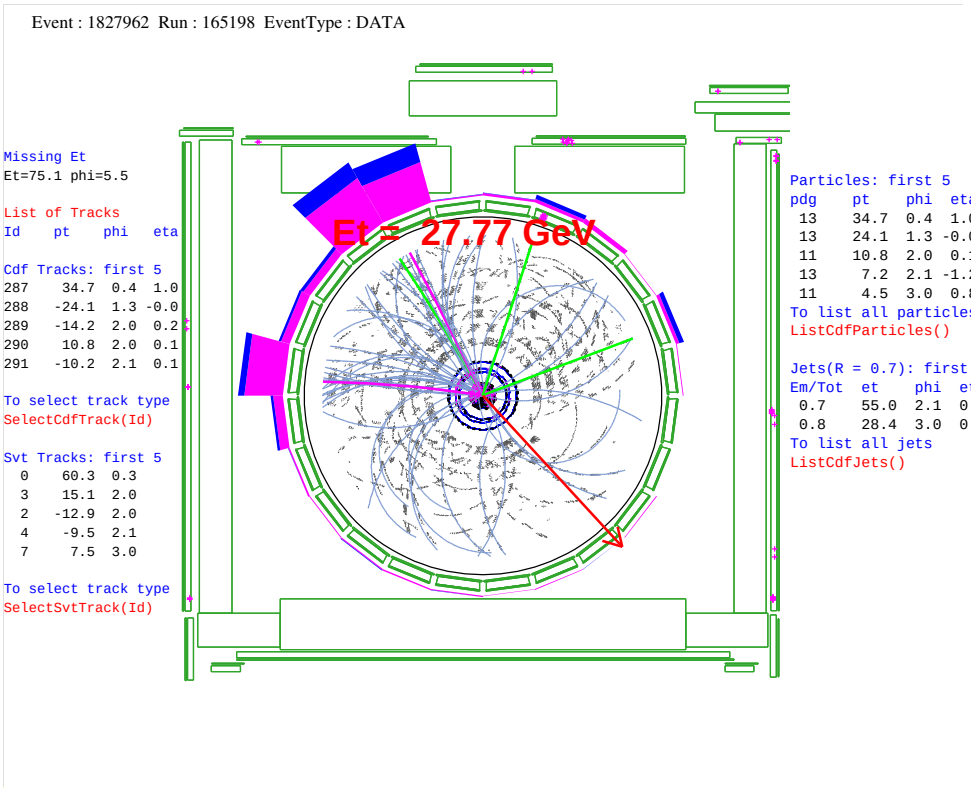

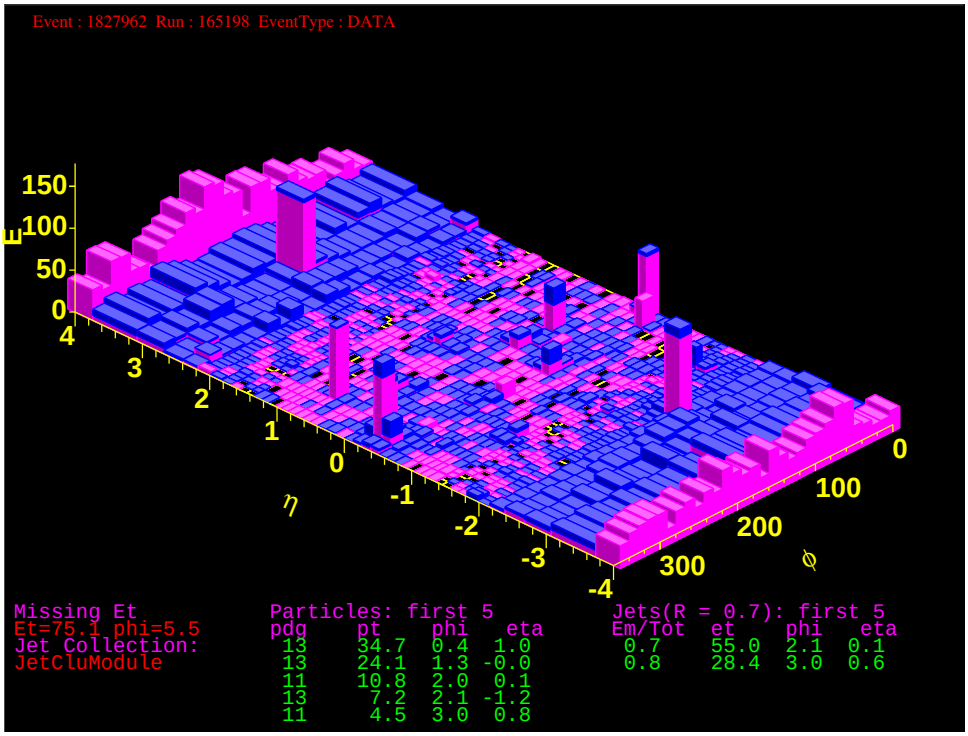

Figure D.1. Event Dispay plots for signal $\mu\mu$ event (run number 165198).

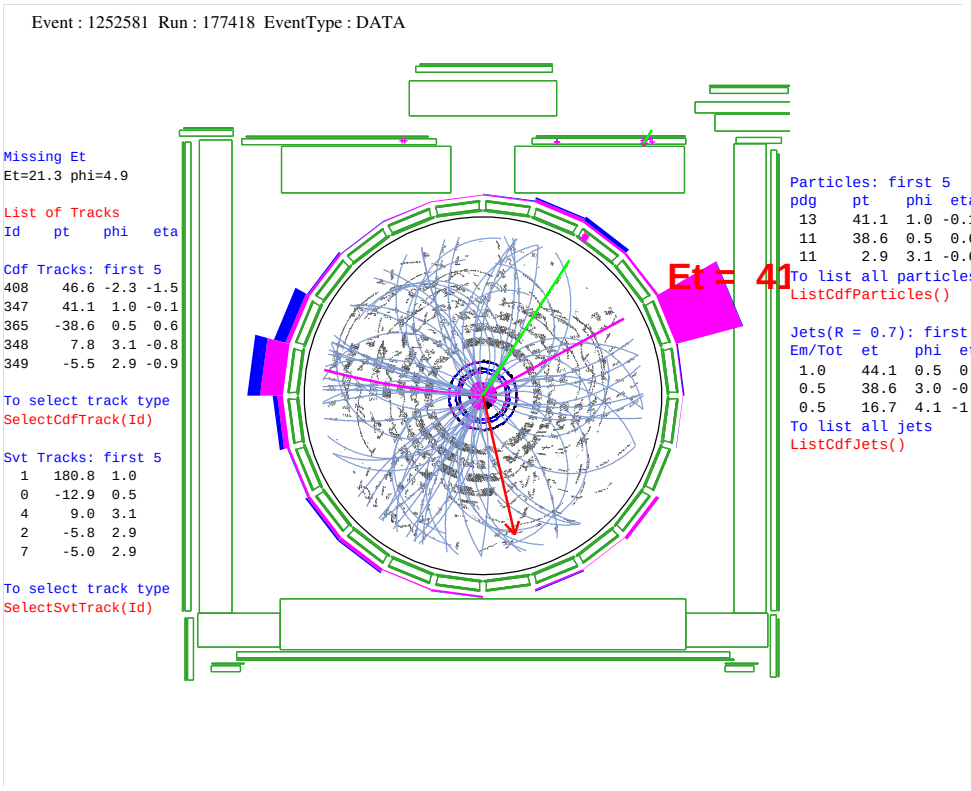

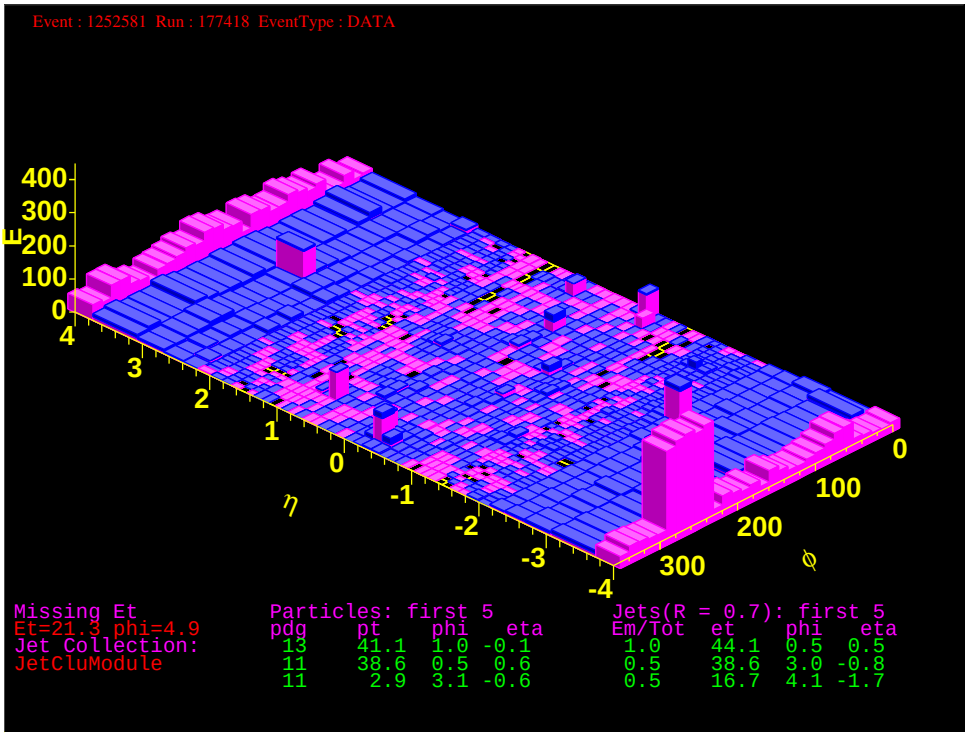

Figure D.2. Event Dispay plots for signal $e\mu$ event (run number 177418).

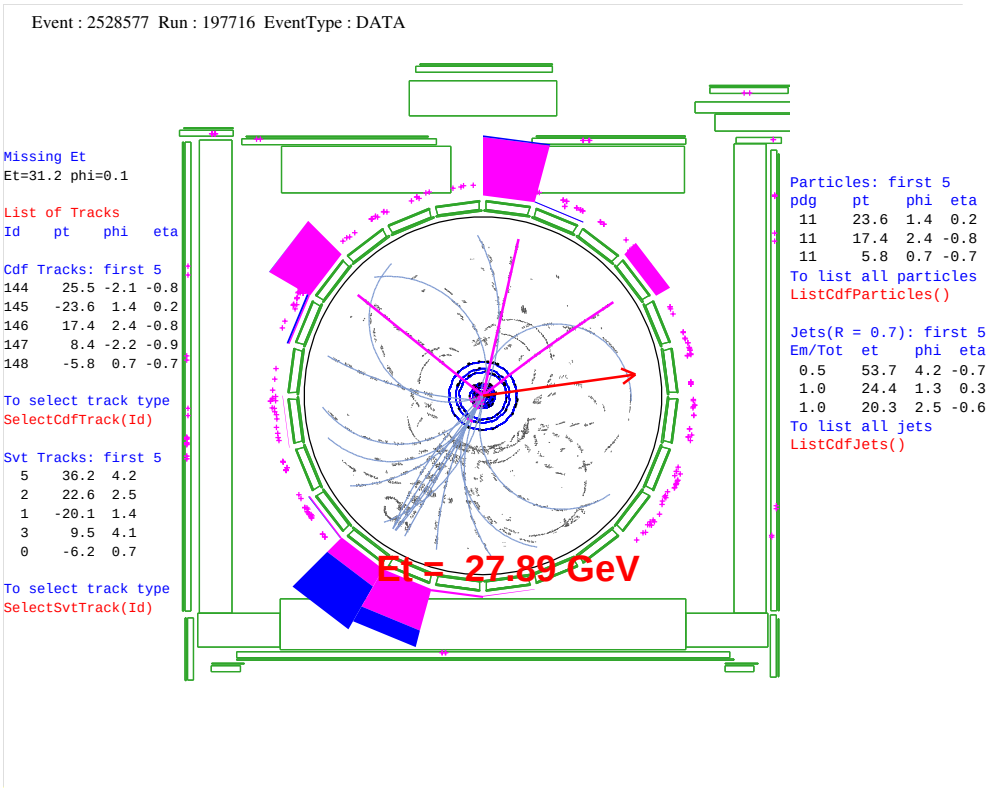

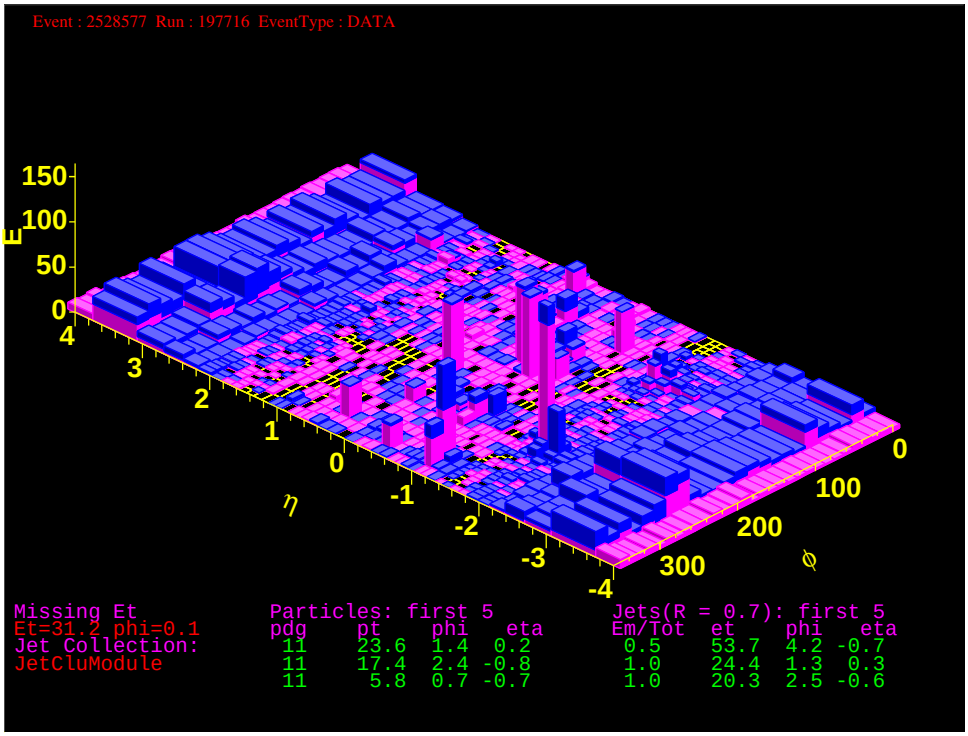

Figure D.3. Event Dispay plots for signal ee (eee) event (run number 197716).

LIST OF REFERENCES

LIST OF REFERENCES

[1] F.Halzen and A.D.Martin, **"Quarks and leptons: An Introductory Course in Modern Particle Physics"**, John Wiley & Sons, (1984).

[2] C.L.Bennett, et.al.,**"First Year Wilkinson Microvawe Anisotropy Probe (WMAP) Observations : Maps and Basic Results"**, astro-ph/0302207.
G.Hishaw, et.al.,**"First Year Wilkinson Microvawe Anisotropy Probe (WMAP) Observations : The Angular Power Spectrum"**, astro-ph/0302217 .

[3] S.L. Glashow, Nucl. Phys. **22** 579 (1961).
S. Weinberg, Phys. Rev. Let. **19** 1264 (1967).

[4] Particle Data Group, H.E.Haber, Phys. Rev.**D66** 895 (2002).

[5] LEPSUSYWG, ALEPH, DELPHI, L3 and OPAL experiments, note LEPSUSY/04-01.1,
http://lepsusy.web.cern.ch/lepsusy/Welcome.html .

[6] LEPSUSYWG, *ibid.*, note LEPSUSY/01-03.1,
LEPSUSYWG, *ibid.*, note LEPSUSY/02-04.1.

[7] W.Beenakker, R.Höpker and M.Spira, **" PROSPINO: A Program for the Production of Supersymmetric Particles in Next-to-leading Order QCD"** , hep-ph/9611232.

[8] G.Zech, Nucl. Instum. Methods A **277** 608 (1989).
T.Huber et al., Phys. Rev.**D41**, 2709 (1990).

[9] CDF Collaboration, Phys. Rev Let. **90** 251801 (2003).

[10] Arnold Pompoš, **Ph.D. Thesis** Accepted by Purdue University, West Lafayette, Indiana on December 6, 2002. CDF Note 6294.

[11] Fermilab Beams Division, **Run II Handbook**.
http://www-bdnew.fnal.gov/pbar/run2b/Documents/RunII_handbook.pdf

[12] Fermilab Beams Division, **Fermilab Linac Upgrade. Conceptual Design**.
http://www-lib.fnal.gov/archive/linac/FERMILAB-LU-ConceptualDesign.pdf

[13] Fermilab Beams Division, **Booster Rookie Book**.
http://www-bd.fnal.gov/proton/booster/rookie/realrookiebook.html

[14] Fermilab Beams Division, **Recycler Design Report**.
http://www-lib.fnal.gov/archive/1997/tm/TM-1991.html

[15] Fermilab Beams Division, **The Antiproton Source Rookie Book**. *http://www-bdnew.fnal.gov/pbar/documents/PBAR_Rookie_Book.pdf*

[16] The CDF II Collaboration, **The CDF II Detector. Technical Design Report**, FERMILAB-Pub-96/390-E, Nov. 1996

[17] Arnold Pompoš, **Ph.D. Thesis** Accepted by Purdue University, West Lafayette, Indiana on December 6, 2002. CDF Note 6294.

[18] H.Baer, F.E.Paige, S.D.Protopopescu, X. Tata, **ISAJET 7.48: A Monte Carlo Event Generator for pp, $\bar{p}p$, and e^+e^- Interactions**, hep-ph/0001086.

[19] S.D. Drell and T.-M. Yan, Phys. Rev. Lett. **25**, 316 (1970).

[20] H. Bachacou, et. al., **"$t\bar{t}$ Event Selection and Detection Efficiency for Winter 2003 Lepton+Jets Analyses"**, CDF note 6084.

[21] Sourabh Dube, John Zhou, Amit Lath, Sunil Somalwar, CDF note 8445

[22] E.Lytken, A.Canepa, D.Bortoletto, CDF note 8336

[23] Ulysses Grundler, Lubomir Lovas, Anyes Taffard, CDF note 8618

[24] Larry Nodulman, CDF note 6971

[25] Michael Gold, Vladimir Rekovic, John Strologas, CDF note 8479

[26] A. Bhatti, at. al., **" Determination of the Jet Energy Scale at the Collider Detector at Fermilab"** , hep-ex/0510047.

[27] Oscar Gonzalez, Web Talks autumn 2005

[28] Doug Benjamin, Al Goshaw, Beate Heinemann, Helen Hayward, Michael Kirby, Naho Tanimoto, CDF note 6619

[29] John Conway, CDF note 6428

[30] The DØ Collaboration, **Search for the lightest scalar top quark in events with two leptons in ppbar collsions at sqrt(s)=1.96 TeV** , Fermilab-PUB-08/508-E, Nov. 2008, http://arxiv.org/abs/0811.0459

[31] Willis Sakumoto, CDF note 8318

[32] Virgil Barnes, Daniela Bortoletto, Stephan Lammel, Arnold Pompos, CDF Note 5912.
Virgil Barnes, Daniela Bortoletto, Stephan Lammel, Arnold Pompos, CDF Note 5913.

[33] Martin Griffiths, Beate Heinemann, Giulia Manca, CDF note 7470

VITA

[redacted]

Alexey Alexandrovich Sedov [redacted] He graduated from middle school #39 in 1989 and attended school for advanced scholars #4 at Nizhny Novgorod Politechnical University from 1989 to 1991. He earned his Master degree in Moscow Institute of Physics and Technology in 1997. During years 1996 - 1998 as a part of small subgroup of ITEP (Institute of Experimental and Theoretical Physics) group he created, tested and installed Forward Tagging System for H1 experiment, DESY. In 1998 he joined Purdue University seaking Ph.D in experimental high energy physics. In year 2000 he began working in the CDF collaboration in Batavia, IL, as a student of prof. Virgil Barnes. For more than 5 years he was the major CDF Plug Sourcing expert stationed in Fermilab. He conducted his thesis research until receiving his Ph.D in Physics in May 2009.